Universidade de São Paulo
Instituto de Física

Sistema de imagem de grande área, sensível à energia, para fluorescência de raios-X baseado em detectores GEM

Geovane Grossi Araújo de Souza



Orientador: Prof. Dr. Marco Bregant
Co-orientador: Dr. Hugo N. da Luz

Tese de doutorado apresentada ao Instituto de Física da Universidade de São Paulo, como requisito parcial para a obtenção do título de Doutor em Ciências.

Banca Examinadora:
Prof. Dr. Marco Bregant - IFUSP
Profa. Dra. Marcia de Almeida Rizzutto - IFUSP
Dr. Bruno Cavalcante de Souza Sanches - EPUSP
Prof. Dr. Edmilson José Tonelli Manganote - UNICAMP
Prof. Dr. João Filipe Calapez de Albuquerque Veloso - Universidade de Aveiro

São Paulo
2023

FICHA CATALOGRÁFICA
Preparada pelo Serviço de Biblioteca e Informação
do Instituto de Física da Universidade de São Paulo

Souza, Geovane Grossi Araújo de

Sistema de imagem de grande área, sensível à energia, para fluorescência de raios-X baseado em detectores GEM. São Paulo, 2023.

Tese (Doutorado) - Universidade de São Paulo. Instituto de Física. Depto. Física Nuclear.

Orientador: Prof. Dr. Marco Bregant

Área de Concentração: Instrumentação em Física Nuclear.

Unitermos: 1. Instrumentação (Física); 2. Detetores radioativos; 3. Fluorescência.

USP/IF/SBI-043/2023

University of São Paulo
Physics Institute

Energy sensitive and large area X-ray fluorescence imaging system based on GEM detectors

Geovane Grossi Araújo de Souza

Supervisor: Prof. Dr. Marco Bregant
Co-supervisor: Dr. Hugo N. da Luz

Thesis submitted to the Physics Institute of the University of São Paulo in partial fulfillment of the requirements for the degree of Doctor of Science.

Prof. Dr. Marco Bregant - Supervisor - IFUSP
Prof. Dr. Marcia de Almeida Rizzutto - IFUSP
Dr. Bruno Cavalcante de Souza Sanches - EPUSP
Prof. Dr. Edmilson José Tonelli Manganote - UNICAMP
Prof. Dr. João Filipe Calapez de Albuquerque Veloso - Universidade de Aveiro

São Paulo
2023

Dedico este trabalho ao meu avô, Itamar.

Agradecimentos

Esse trabalho foi realizado com apoio da Coordenação de Aperfeiçoamento de Pessoal de Nível Superior - Brasil (CAPES) - Código de Financiamento 001. The project developed at the Czech Technical University in Prague was founded by the grant GAČR GA21-21801S (Czech Science Foundation).

My sincere thanks to the people in the GDD lab at CERN, in special Florian Brunbauer for the exchange of ideas. I also want to thank Rudolf Sýkora and Tom Sýkora from the Czech Technical University in Prague.

Meus agradecimentos ao professor Alexandre Suaide por me apresentar ao grupo e pela ajuda nos mais diversos assuntos. Ao Ricardo Romão e Ricardo Menegasso pela disponibilidade, prontidão e colaboração durante o projeto. Aos professores Marcelo Munhoz e Tiago Fiorini, por todas as contribuições, ideias e pela confiança depositada. Ao meu co-orientador Hugo Natal da Luz e sua esposa Lúcia, tenho um carinho e uma gratidão enorme por vocês. Ao meu orientador, Marco Bregant, uma pessoa paciente, bem-humorada, que esteve sempre presente me ensinando e tenho certeza que poderei contar com ele. A toda equipe que participou do projeto do SampaSRS. Um grande abraço ao Cesar, Thiago e André.

Já são quase 10 anos de Instituto de Física e posso dizer que mantenho amizades incríveis com pessoas que conheci logo no primeiro dia. Um abraço especial para o Thiago, Ramsés e Rodrigo. Gostaria de agradecer nominalmente a alguns amigos que tive companhia, mesmo que de maneira virtual, durante a pandemia. As conversas e jogos me ajudaram a passar por esse momento e tenho um apreço enorme por vocês, um abraço ao Elion, Jean, Pedro, Nick, Bahia, Corsini e Léo. Também preciso me lembrar dos amigos que ainda estão ou já passaram pelo HEPIC durante esses anos, em especial ao Leonardo, Renan, Lucas, Fábio, Thais, Mona, Eli e Caio. Um grande abraço também para meus amigos do Karatê.

Ao meu pai, Marco Aurélio e sua companheira, Wallana, obrigado pelo suporte e por todo interesse que demonstram em meu trabalho. À minha mãe, Maria Cabrine, uma pessoa sempre disposta e que sempre me apoiou na minha decisão de seguir essa carreira. Um grande e caloroso abraço ao meu irmão Ramon, companheiro nas mais diversas aventuras. Apesar da distância e de sentir muito sua falta aqui no Brasil conseguimos achar hobbies em comum que nos conectam. Obrigado por me ajudar tanto.

Por fim, à minha companheira Mayumi, sua companhia e carinho me alegram o coração.

"Happiness is only real when shared." —Christopher McCandless

Abstract

This work consists in the assembly, study, and characterization of a large area, position sensitive, and energy dispersive X-ray gaseous detector based on GEMs (*Gas Electron Multiplier*), optimized to operate in the energy range from 1 keV to 30 keV. The advantage of using such large detectors is to reconstruct images without the need to scan the sample. These detectors are cost effective when compared to solid state devices, they can reach high gains using multiple multiplication structures and, with a suitable readout electronics, it is possible to work at high counting rates. Moreover, handling these detectors is relatively simple since they can work without flammable or toxic gases and, by making small changes in their assembly, it is possible to detect different types of radiation.

The construction of a detector that operates in this energy range is interesting to the scientific community because it may assist research from different areas with position sensitive X-ray fluorescence imaging. Exploiting this technique it is possible to detect the presence of different chemical elements and to obtain their spatial distribution in a sample. Cultural heritage studies can be performed using this technology and also this equipment can be implemented in different fields such as industry, crystallography and nuclear safety and security.

In this work, the SAMPA chip was integrated in CERN's Scalable Readout System to collect the signals produced by the detector. Software tools for acquisition control, data acquisition, and the reconstruction of images and spectra were also developed. To test this new system a thin-gap detector for 1-D X-ray imaging and fluorescence, and also on a small Time Projection Chamber for cosmic ray detection were build. Along with the experimental results, a set of simulations were made in order to adapt and optimize this type of detectors, initially developed for high energy physics, to low energy applications such as X-ray imaging and fluorescence.

Keywords: Radiation detectors, micropattern gaseous detectors, gas electron multiplier, X-ray fluorescence imaging, readout electronics.

Resumo

Este trabalho consiste na construção, estudo e caracterização de um detector gasoso de grande área, sensível à posição e à energia baseado em GEMs (*Gas Electron Multiplier*), optimizado para operar na faixa de energias entre 1 keV e 30 keV. Estes detectores de microestruturas apresentam resultados satisfatórios para amostras grandes pois permitem a reconstrução de imagens sem a necessidade de fazer uma varredura no objeto estudado. Além disso, podem alcançar altas taxas de contagens, apresentam baixo custo quando comparados com os detectores de estado sólido e ganhos elevados pois podem ser utilizados em estruturas múltiplas para multiplicação. Ademais, o manuseio e manutenção desses detectores é relativamente simples quando não são utilizados gases inflamáveis ou tóxicos, e acabam sendo versáteis em relação à montagem, podendo detectar diferentes tipos de radiação.

A construção de um detector que opera nessa faixa de energia é de interesse da comunidade científica pois pode auxiliar no trabalho de pesquisadores das mais diversas áreas do conhecimento através da técnica de fluorescência de raios-X. Explorando esse fenômeno físico é possível inferir a presença de diversos elementos químicos e obter informações em relação às suas distribuições espaciais. Com isso, estudos aprofundados ligados ao patrimônio histórico e cultural podem ser feitos, além da utilização desse equipamento para aplicações na indústria, cristalografia e para segurança e proteção nuclear.

Para leitura dos sinais e obtenção de dados com o detector o chip SAMPA foi integrado no Scalable Readout System e um conjunto de ferramentas para o controle da aquisição, recebimento de dados na rede, monitoramento e reconstrução das imagens e espectros em energia foram desenvolvidos durante o período. Para testar as ferramentas desenvolvidas um detector triplo-GEM foi desenvolvido e utilizado para obtenção de dados em 1-D de imagem e fluorescência de raios-X, assim como uma pequena Câmara de Projeção Temporal capaz de detectar a passagem de raios cósmicos. Junto com os resultados experimentais, um conjunto de simulações computacionais foram feitas de forma a ajudar no projeto, estudo e construção do detector, adequando a sua montagem da melhor maneira à aplicação de imagem de raios-X de baixa energia.

Palavras-chave: Detectores de radiação, detectores gasosos baseados em micro-estruturas, detectores do tipo GEM, imagem de fluorescência de raios-x, eletrônica de leitura.

Contents

1 Introduction **17**

2 Interaction of radiation with matter **21**

2.1 Electromagnetic radiation 21

2.1.1 Attenuation of photons by matter 21

2.1.2 Photoelectric effect 23

2.1.3 Compton scattering 24

2.1.4 Pair production 24

2.1.5 Characteristic X-ray emission 25

2.2 Charged particles 26

2.2.1 Protons, alpha particles and atomic ions 26

2.2.2 Electrons and Positrons 27

2.3 Neutrons 28

3 Gaseous detectors **31**

3.1 The single and multi wire proportional detectors 33

3.2 Microstrip Gas Chamber 33

3.3 Micromesh Gaseous Structure 35

3.4 Gas Electron Multiplier 36

3.5 The time projection chamber 37

4 Detector characterization **39**

4.1 Detection or conversion efficiency 39

4.2 Collection and extraction efficiencies 39

4.3 Charge multiplication factor and gain 41

4.4 Ion back-flow 41

4.5 Experimental measurements of efficiencies, ion back-flow and gain 41

4.6 Energy resolution 43

4.7 Spatial resolution 43

4.7.1 Point and line spread function 43

4.7.2 Contrast 44

4.7.3 Modulation transfer function 45

5 Simulations **47**
5.1 Garfield++ and HEED . . . 47
5.2 Detection efficiency and energy resolution . . . 48
5.3 Photon escape probability . . . 51
5.4 Spatial resolution . . . 53
5.5 Simulation of the readout system and reconstruction algorithms . . . 59
5.5.1 Flat-field correction algorithm for strip readouts . . . 63
5.6 Copper contamination of the energy spectra. . . . 64

6 Ion back-flow simulations **71**
6.1 Using a mesh to reduce the IBF . . . 71

7 Experimental setup **77**
7.1 The detector . . . 77
7.2 The geometry for XRF imaging . . . 78
7.2.1 Geometric response . . . 79
7.3 The scalable readout system . . . 83
7.4 The SAMPA chip . . . 84
7.4.1 The SAMPA hybrid . . . 84
7.4.2 The SampaSRS software . . . 85
7.4.3 Clustering algorithm for event reconstruction . . . 90
7.4.4 Data production and zero suppression . . . 90

8 Experimental results **93**
8.1 Detector characterization . . . 93
8.1.1 The SRS with APV25 . . . 93
8.1.2 The SRS and the SAMPA chip . . . 98
8.2 Application of the SAMPA in a TPC . . . 102

9 Discussion and conclusions **109**

Chapter 1

Introduction

The discovery of X-rays changed the world and was an important breakthrough in science, industry and medicine. Since the first detection of such radiation, using platinocyanide plates by Wilhelm Conrad Röntgen [1], new detection techniques and technologies are being developed to improve the quality and capability of doing X-ray images.

Over the years the techniques that make use of X-rays have evolved and spread and after the development of energy-dispersive detectors we were able to use different approaches such as X-ray fluorescence (XRF) [2] and particle-induced X-ray emission (PIXE) [3] to make spectral analyses, obtaining important results and developments in fields such as geology, cultural heritage studies and new materials development.

Gaseous detectors are a class of detectors that are sensitive to ionizing radiation and can either be or not energy sensitive, that is, capable of distinguishing X-rays with different energy, and thus, create an energy spectrum of a sample. These detectors are dated from the first decades of the 20th century and their use has not changed since, consisting in the collection of the free charge carriers generated by the passage of ionizing radiation inside a gaseous volume [4].

Since the creation of the Multi-Wire Proportional Chamber (MWPC) by Charpak [5], a detector capable of determining the radiation interaction point with position resolution of a few millimeters, and years later the development of the Time Projection Chamber (TPC) by Nygren [6], these detectors are being widely used in high energy physics experiments to identify charged particles produced after collisions, but also can be used in nuclear reactions related experiments. With the new photo-lithography methods developed in the last few decades to create printed circuits, there was a breakthrough in the construction of gaseous detectors, allowing exploring new electrode geometries, as in micropattern gaseous detectors (MPGD). The MPGD family is composed by different detectors such as, for example, the *Microstrip Gas Chamber* (MSGC) [7], the *Gas Electron Multiplier* (GEM) [8], the *Micro-Mesh Gaseous Structure* (MICROMEGAS) [9], the *Thick-Gas Electron Multiplier* (Thick-GEM) [10], the *Micro-Hole and Strip Plate* (MHSP) [11], the ThickCOBRA [12] or the WELL [13].

MPGDs are structures used to amplify the primary charge generated after the radiation interaction with the medium. These detectors are constructed using high precision photolithography followed by chemical or physical etching, a process similar to the one used on

printed circuit production. By applying a suitable potential to the MPGD structure it is possible to create zones with an electric field high enough to initiate Townsend avalanches [14], generating a multiplication region that amplifies the signal. In the MPGDs that are semi-transparent to electrons, it is possible to stack multiple structures, achieving high gains and a good signal-to-noise ratio at lower voltages, which improves operation stability. Following all these planar amplifying structures it is possible to place a set of segmented electric conductive electrodes and, using a multichannel reading electronic, calculate the position of interaction inside the detector. Using this assembly one can cover a large sensitive area for a much lower price when compared to Solid State Detectors. This new generation of proportional gaseous detectors has shown good performance in high energy physics experiments in terms of spatial resolution, counting rate, radiation hardness, operational stability, as well as to be suitable to cover large regions (up to $32\,\mathrm{m}^2$ in the ALICE TPC, for example [15]).

The objective of this project is to use the knowledge and technology that was developed in the high energy physics environment to develop an optimized imaging system based on GEMs for X-ray fluorescence. The studies developed before this work [16, 17] showed its capabilities for X-ray imaging in transmission and fluorescence modes (figures 1.1 and 1.2 respectively). These works also presented a limitation of the detector and the acquisition system, the extra peak in the energy spectrum generated by the copper fluorescence that happens inside the detector due to its material composition. In this work, this effect was studied and ways to mitigate it are presented. The SAMPA chip [18] was implemented into the Scalable Readout System (SRS) [19], and tools and algorithms to retrieve the data and reconstruct spectra and images were created. With this new readout system, the counting rates achieved improved by at least one order of magnitude (from 1.2 kHz with the SRS using the APV25 [83] to values above 20 kHz with the SRS using the SAMPA chip).

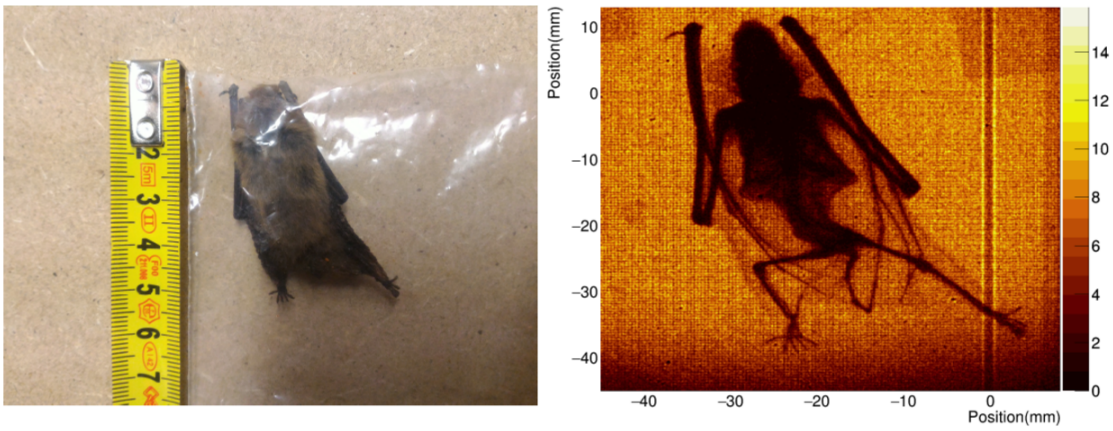


Figure 1.1: X-ray transmission image using GEM detectors and the SRS with the APV25 ASIC. This image was obtained after approximately 3 hours of acquisition. Figure from [16].

This work is divided as follows: In chapter 2, it is possible to find a description of the most

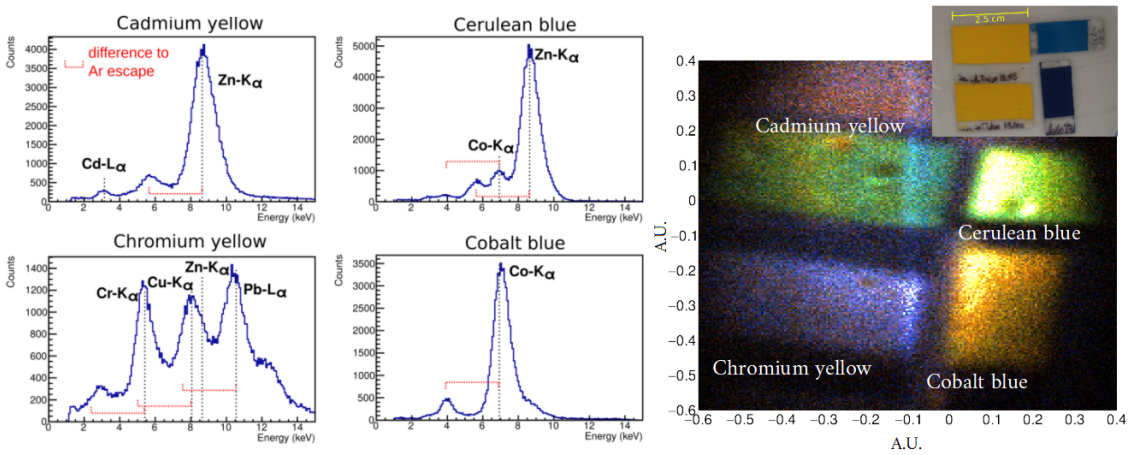


Figure 1.2: X-ray fluorescence spectrum and imaging of a set of color pigments. Figure adapted from [17].

important concepts regarding the electromagnetic radiation interaction with matter. MPGDs are versatile detectors and can detect different types of radiation, such as neutrons or charged particles, however, here we will focus on the effects related to electromagnetic radiation. Chapter 3 gives an overview of the gaseous detectors family, their differences and applications in different fields. Chapter 4 will introduce to the reader the definitions that describe the performance of these detectors and ways to characterize it. Chapter 5 is focused in ways to optimize the X-ray detection on GEM-based gaseous detectors in the energy range we are interested in ($1 \sim 30\,\text{keV}$) by using computational tools, such as Garfield++ [20]. Chapter 6 is a contribution to the ion back-flow study, a subject of interest when working with TPCs or detectors that are operated at high counting rates. Ideas to suppress it are shown in this section. Chapter 7 describes the detectors that were built during this work and we address the integration of the SAMPA with the RD51 [21] SRS. In chapter 8 we show the experimental results with the system described in the previous chapter and the last part of the work is the conclusion, with an overview of the results, future work and ideas that can be tested.

Chapter 2

Interaction of radiation with matter

The principle of operation of any ionizing radiation detector is the collection and processing of the free electrons generated by the passage of the radiation through its medium. The mechanism of interaction and the energy loss and consequently the number of free electrons created are different for X-ray photons, electrons, ions or neutrons. This section will provide a brief review of the main processes of the interaction for X-ray photons and other particles.

2.1 Electromagnetic radiation

X-rays are produced by electronic transitions and the acceleration of charged particles. If these photons have a wavelength between about 10 to 0.01 nm (energies between 124 eV to 124 keV) they are conventionally named X-rays and due to this broad energy range, different effects may occur when photons interact with matter. There is no partially absorbed photon when it interacts with the medium, and so, a photon beam traveling through a material will be attenuated in intensity but will not suffer from energy degradation, and this will be a difference when comparing interaction with matter of photons and of charged particles or neutrons, for example. The three main interaction effects for higher energy photons are the photoelectric effect, Compton effect and pair production.

2.1.1 Attenuation of photons by matter

When traveling through a material, a beam composed by a spectrum of photons with different energies will get hardened (filtered) as a result of the selective attenuation of lower energy photons. The Lambert–Beer law describes how the absorption and attenuation of electromagnetic radiation by a material takes place, and it has a great importance in nuclear physics studies and radiology protection. A mono-energetic beam traveling through a material with thickness dx has its intensity decreasing with the following rate:

$$dI = -I\lambda dx$$

integrating this equation we obtain the expression of the attenuation of a beam of photons.

$$I = I_0 e^{-\lambda x} = I_0 e^{-\mu \rho x}, \tag{2.1}$$

where, I is the beam intensity after passing through length x in the material, I_0 is the original intensity, λ is the linear attenuation coefficient, which is the attenuation per unit of length. It is often more convenient to express the attenuation coefficient in terms of density (ρ), therefore, the mass attenuation coefficient μ, defined as $\frac{\lambda}{\rho}$ (expressed in cm^2/g), results in the right term of equation 2.1.

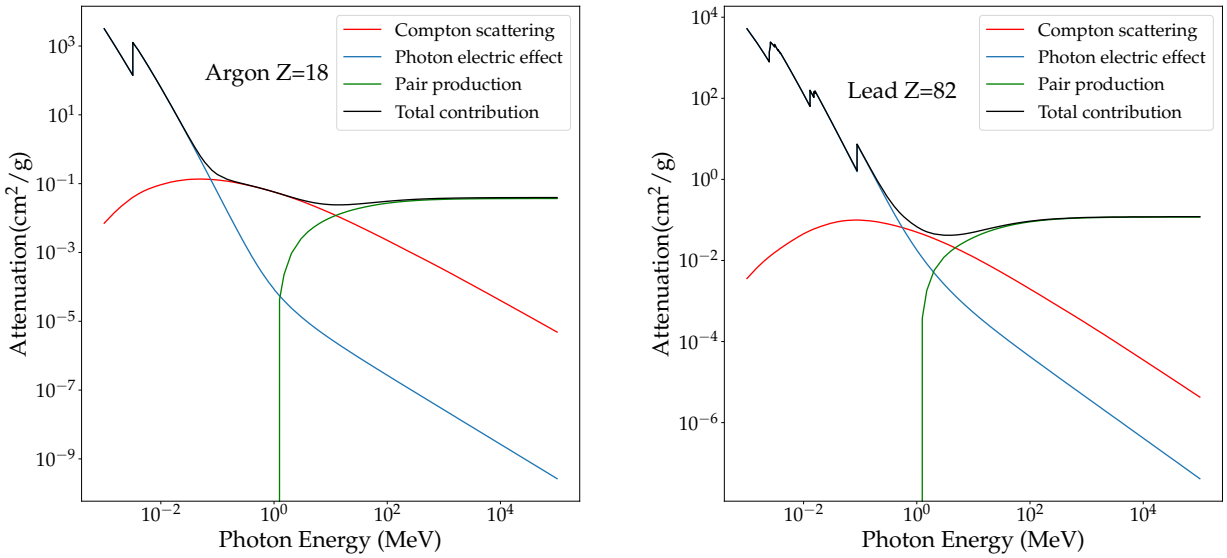


Figure 2.1: Mass attenuation coefficient for argon and lead as a function of the energy. Values obtained from the XCOM database [22].

The linear attenuation coefficient λ can be written in terms of the contributions of each of the three possible interactions of photons with matter, which change according to the photon energy and the target's atomic number as it can be seen in figure 2.1.

$$\lambda = \tau + \sigma + \kappa, \tag{2.2}$$

where τ, σ and κ are the contributions related to the photo-electric effect, the Compton effect and pair production, respectively. Figure 2.2 shows the region of predominance for each of the effects as a function of the atomic number of the medium and energy of the photon.

From figures 2.1 and 2.2 it is possible to see that in the energy range of X-rays, the contribution to the total absorption cross section is dominated by photo-electric effect, and so, the other effects can be neglected and will be referred in this discussion for their importance in Physics.

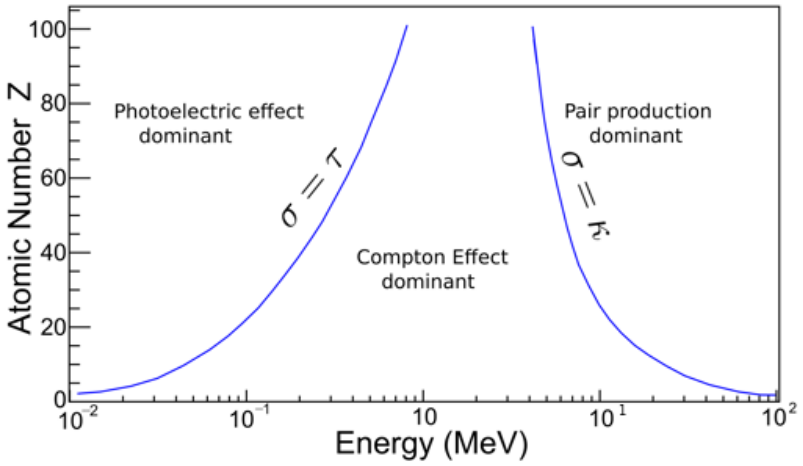


Figure 2.2: Photon interaction predominant effect as a function of energy and atomic number. Adapted from [23].

2.1.2 Photoelectric effect

In 1887 Hertz observed that the probability to create an electrical discharge between electrodes was higher when the cathode was irradiated by ultra-violet (UV) electromagnetic radiation [24]. The mechanism was named photoelectric effect and it was only fully understood when Einstein proposed his theory to explain this phenomenon. The energy of each photon is equal to the product of Planck's constant h with the radiation frequency ν. When the photon energy value is higher than the bidding energy of the electron in the material, it can be ejected, passing from a bound state to a free state.

The kinetic energy of an electron ejected from the atom is given by:

$$K = \mathrm{h}\nu - W, \tag{2.3}$$

where W is the binding energy between the electron and the atom, also known as the work function. This effect is only possible if the photon has an energy that is equal to or greater than W. The cross-section for photoelectric effect (only in the K-shell) can be calculated using the Born approximation which, disregarding relativistic effects ($\mathrm{h}\nu \ll \mathrm{m_e c^2}$), consists on the equation 2.4 [4]:

$$\sigma_p = \frac{8\pi Z^5 \alpha^4 4\sqrt{2}}{3} \left(\frac{\mathrm{e}^2}{\mathrm{m_e c^2}}\right)^2 \left(\frac{\mathrm{m_e c^2}}{\mathrm{h}\nu}\right)^{7/2}, \text{for } \mathrm{h}\nu > E_K \tag{2.4}$$

where $\mathrm{m_e}$ is the invariant mass of the electron, α is the fine structure constant, which is equal to $\frac{1}{137}$ and Z is the atomic number of the target. The cross-section (proportional to the interaction probability) between the photon and the K-shell electron scales with Z^5, but decreases abruptly as the photon energy increases ($\mathrm{h}\nu^{-3.5}$). In the energy range of this work this effect is the major

mechanism of energy deposition by radiation in matter (as figures 2.1 and 2.2 show) and the most important, since it is the effect that will lead to the generation of a characteristic X-ray emission, the aim of this work.

2.1.3 Compton scattering

The Compton scattering or Compton effect is the inelastic scattering between a photon and a free electron [25]. Due to this interaction the direction of a photon will be shifted and also its wavelength, transferring part of its energy to the electron and thereby, depositing energy in the medium.

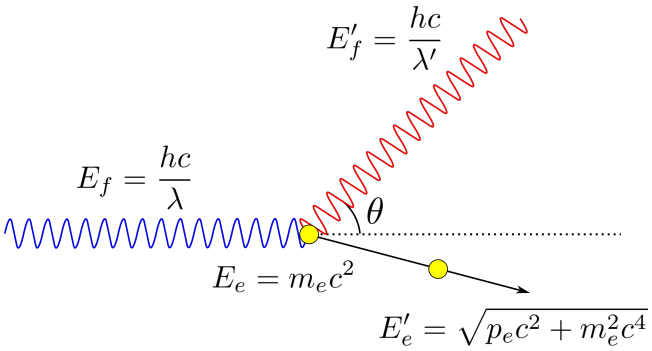


Figure 2.3: Compton effect diagram. Figure from [16].

The initial and final wavelength relations can be derived from the momentum and energy conservation and the geometry of the problem, reaching equation 2.5.

$$E'_{\mathrm{p}} = \frac{E_{\mathrm{p}}}{1 + \frac{E_{\mathrm{p}}}{\mathrm{m_e c^2}}(1 - \cos\theta)} \tag{2.5}$$

or, depending on the wavelengths [25]:

$$\lambda' - \lambda = \frac{1}{\mathrm{m_e c}}(1 - \cos\theta) \tag{2.6}$$

As figure 2.3 shows, after the interaction, part of the photon energy will be transferred to the electron, resulting in a partial energy deposition and a radiation wavelength shift.

2.1.4 Pair production

Pair production becomes possible when the photon's energy is greater than twice the rest mass of an electron, 1.022 MeV. The pair production is the creation of pairs of electrons and positrons by heavy nuclei decays, high energetic photons like the ones generated in colliders, astronomical events such as gamma-ray bursts and high energy particle colliders.

The photon needs to interact with the Coulomb field of nuclei (which is a requirement for momentum conservation [4]), and then it is converted into a pair, as illustrated in figure 2.4. Due to the high mass of the nucleus, its recoil energy can be neglected.

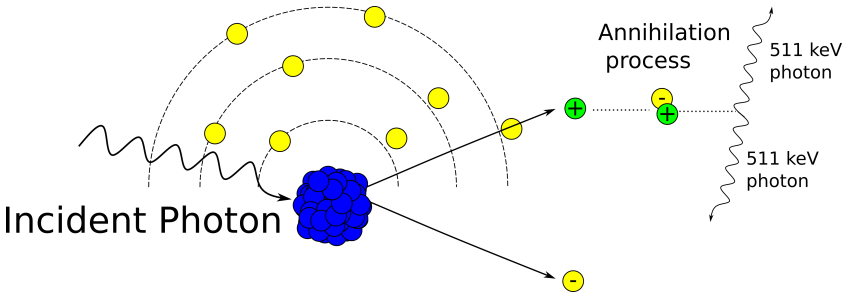


Figure 2.4: Pair production diagram. Figure from [16].

After losing energy to the medium through Coulomb interaction, the positron may encounter an electron and they are annihilated in a process that emits a pair of photons. These photons are emitted back-to-back and this well-known characteristic is exploited in many different techniques that have application not only in physics but also in medicine such as the positron emission tomography (PET) [26].

2.1.5 Characteristic X-ray emission

Electrons can be ejected from inner atomic shells when an atom is hit by a high energy photon or a charged particle. The atom that has an unfilled shell is in an excited state. When the vacancy in the inner shell of the excited atom is filled with an electron from an outer shell, a characteristic X-ray with energy equal to the energy difference between the final and initial states is emitted, as illustrated in figure 2.5.

For heavier atoms, equivalent shells will have larger energy differences, and the characteristic X-rays will be more energetic. The transitions are named according to the electronic shell that became filled and they get a subscript index which is related to the shell where the transition electron came from. If the electron filling the K-shell was originally in the L or M shell, the corresponding X-ray line will be named as K_α or K_β respectively. Since the energy difference grows for outer shells, β transitions are more energetic than α ones. The maximum energy that a K-series photon shows would be produced by filling the vacancy with an unbound electron, and the energy corresponding to this transition is given by the K shell binding energy [14].

This process of characteristic X-ray emission is called X-ray fluorescence. The difference of energy levels is a characteristic of each element, meaning that by precise measurement of the energy of the X-rays, the elements in a sample can be identified. This is the principle of elemental analysis by X-ray fluorescence spectrometry. The technique consists of the analysis of the spectra of photons generated after irradiating a sample with ionizing radiation (particles

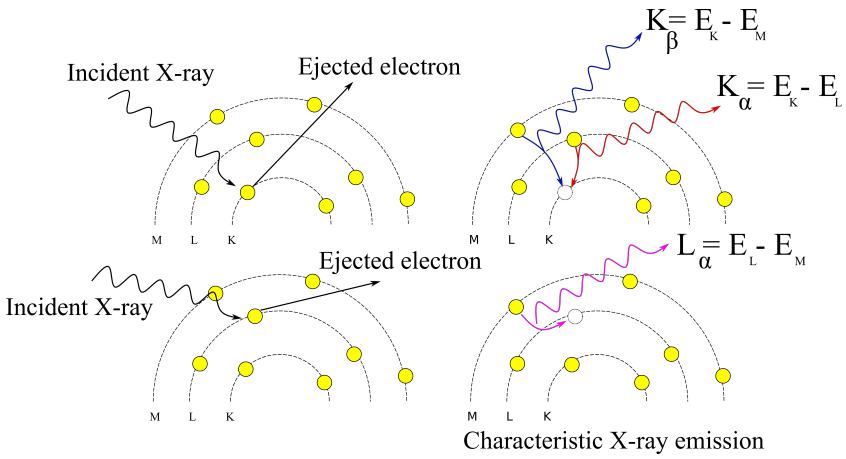


Figure 2.5: The excitation of an atom by an X-ray and consequent emission of a characteristic X-ray. Figure from [16].

or photons). This is a non-invasive and non-destructive technique, since there is no need to remove part of the sample material, making it suitable to identify different elements in rare and valuable samples such as art work.

2.2 Charged particles

Charged particles interact by coulomb force with electrons from the atomic orbitals. These interactions may create excitation or ionization in the atoms of the medium along the traveled path. Due to the difference in the processes related to the energy loss, which depend mainly on the mass of the charged particle, electrons and positrons are treated separately from heavier charged particles.

2.2.1 Protons, alpha particles and atomic ions

Heavy charged particles interacting in a medium will deposit energy (and create a path of excited or ionized atoms) at a certain rate, called the stopping power. The relativistic expression that describes the rate of energy loss $-dE/dx$ is given by the Bethe-Bloch equation [14]:

$$-\frac{dE}{dx} = \frac{4\pi e^4 z^2 NZ}{m_e v^2}\left[\ln\left(\frac{2m_e v^2}{I}\right) - ln\left(1-\frac{v^2}{c^2}\right) - \frac{v^2}{c^2}\right] \tag{2.7}$$

where I, N and Z represent respectively the mean energy for creating ionization and excitation, the number density and atomic number of the crossed medium. v is the velocity of the charged particle and z is its charge, and $\mathrm{m_e}$ is the electron invariant mass.

The rate of energy loss along the path becomes higher towards the end of the ion's traveled path, as it can be seen in figure 2.6.

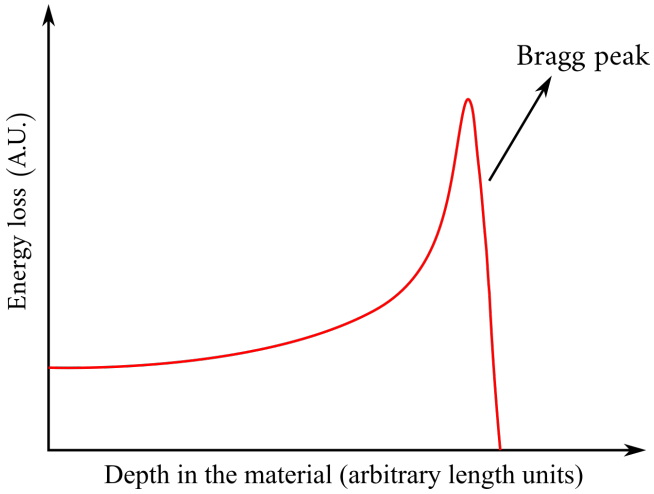


Figure 2.6: Example of an ion energy loss curve in a material.

This is known as the Bragg peak and it happens because, at lower velocities is when the energy loss to the medium becomes maximum. At the very end of the trajectory, the ion is neutralized by capturing electrons from the medium, dropping sharply $-dE/dx$ [4].

2.2.2 Electrons and Positrons

Each interaction between fast electrons and orbital electrons will result in a large amount of momentum transfer due to the equal masses that they have, therefore, a larger amount of energy is lost in a single collision, resulting in abrupt changes of trajectory and energy deposition. Thus, when compared with ions, the path traveled by these fast electrons is much more chaotic [14].

Electrons and positrons will deposit energy in the medium by two different processes, the collisional and the radiative (Bremsstrahlung). The first process is similar as for other heavy charged particles and Hans Bethe developed a theory for the energy loss regarding this component in 1930 [27]. The second depends both on the atomic number of the medium and the initial electron energy. The ratio between the energy loss due to collisional (dE/dx_{col}) and radiative process (dE/dx_r) for an electron can be written as:

$$\frac{(dE/dx_r)}{(dE/dx_{col})} \approxeq \frac{EZ}{700} \tag{2.8}$$

where E is the electron energy in units of MeV and Z is the atomic number of the medium. It can be seen that the contribution of the energy loss due to radiative processes for the electrons in the energy range of 1-30 keV, the one we are interest in this work, is small and can be neglected when using gaseous detectors filled with argon or krypton.

Bremsstrahlung production

The "braking radiation" or Bremsstrahlung from German is the radiation emitted by charged particles after undergoing an acceleration. The change in the velocity can be the result of the interaction between the moving particle and other charged particles or a force field. The conversion of kinetic energy into radiation is larger for higher kinetic energy of the moving particle or the target's atomic number [14]. This process is extremely important in the production of X-rays and happens in large Synchrotron accelerators and in commercial X-ray sources.

In commercial X-ray sources this type of radiation is generated by the decelerating electrons when they are pushed against the target. If their kinetic energy is high enough, along with the continuous background Bremsstrahlung spectrum, characteristics X-rays from the elements composing the target are generated, as figure 2.7 shows, which can be copper, silver or molybdenum, among others.

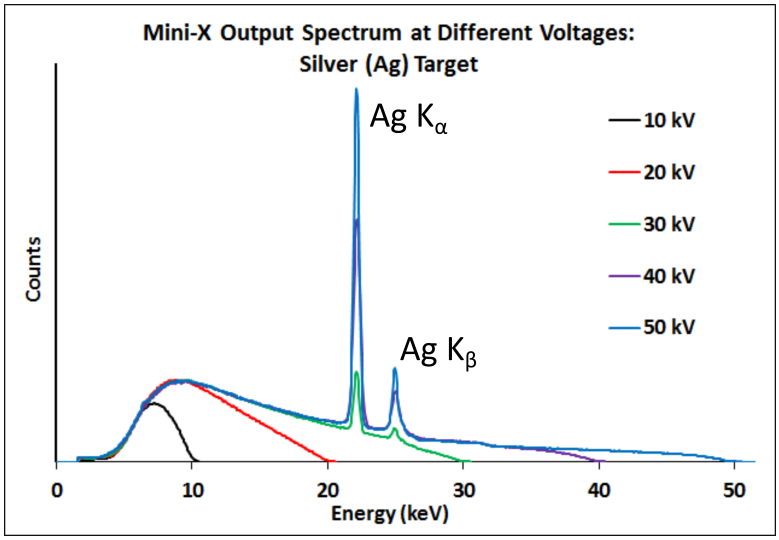


Figure 2.7: The emission of a commercial X-ray tube with Ag target for different accelerating potentials. Figure adapted from [28] for didactic purposes.

2.3 Neutrons

Neutrons do not interact via Coulomb force, therefore, a conversion element that is able to capture them via nuclear reactions must be used. As a result, charged particles or highly energetic photons will be produced and these can be detected according to the mechanisms that were shown before.

For many years ^{3}He was one of the most used gases to convert neutrons into charged particles, however, in the last two decades, due to the high demand and low production, many facilities are running out of it [29]. To overcome this problem, other elements which have

the capability to convert neutrons are being tested. Figure 2.8 shows the neutron interaction cross-section for different elements.

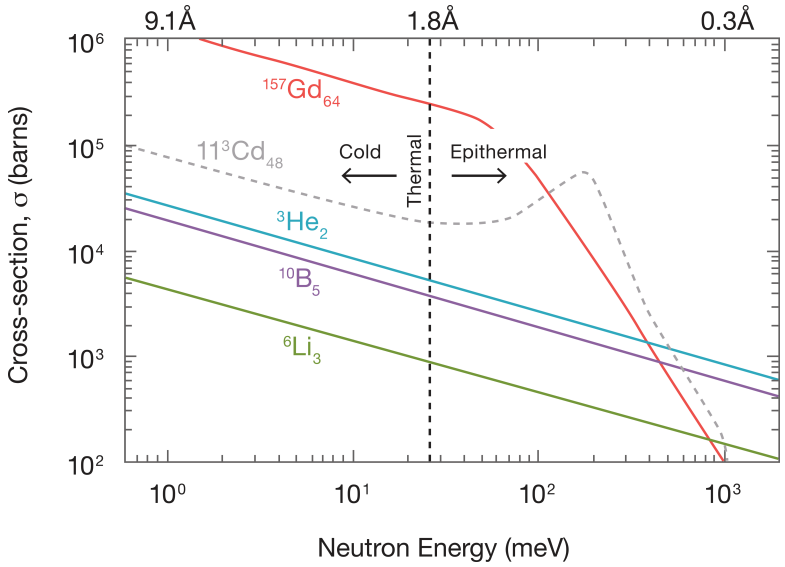


Figure 2.8: Neutron interaction cross-section for different conversion elements. Figure from [30].

Two promising elements to replace ^{3}He are the ^{157}Gd and ^{10}B. The conversion mechanism for these elements can be seen below:

$$^3\mathrm{He} + \mathrm{n} \longrightarrow ^3\mathrm{H} + ^1\mathrm{H} + 0.764\mathrm{MeV}$$

$$^{10}\mathrm{B} + \mathrm{n} \longrightarrow \begin{cases} ^7\mathrm{Li} + ^4\alpha + 2.31\mathrm{MeV} + 0.48\mathrm{MeV}(\gamma) \\ ^7\mathrm{Li} + ^4\alpha + 2.79\mathrm{MeV} \end{cases}$$

$$^{157}\mathrm{Gd} + \mathrm{n} \longrightarrow ^{158}\mathrm{Gd}^* \longrightarrow ^{158}\mathrm{Gd} + \gamma's + \text{conversion electrons}$$

It is possible to adapt the cathode or even the GEM foils with thin ^{10}B layers to be used as conversion materials [31] for neutrons, expanding the possibility of using position sensitive gas detectors.

Chapter 3

Gaseous detectors

The first radiation detectors, for example the photographic plates, exploit a chemical reaction induced by the passage of a charged particle or a photon. Once exposed, the light-sensitive chemicals become more or less opaque depending on the exposure [32]. In gaseous detectors, the absorbing gas is ionized and the electrons and ions are then separated and eventually amplified by electric fields as figure 3.1 illustrates. The ionizing particle (represented as the green sphere) creates electron-ion pairs inside the medium represented by the blue (ions) and the red (electrons) and, by applying a potential to the electrodes, it is possible to separate the positive and negative charges, collect the electrons in the anode and by processing it with a specific electronic system, transform this pulse charge into a signal that can be read and analyzed. According to different characteristics of the signal it is sometimes possible to determine parameters related to the original event, such as the energy deposited in the medium or the type of charged particle.

Figure 3.2 shows the different regimes of operations of gaseous detectors. In the first region, the electric field is not high enough to avoid charge recombination and therefore signals are lost and a detector does not operate in this condition. Increasing the electric field we reach the first regime of operation for gaseous detectors, which is the ion saturation. Here, all the charge carriers generated by the ionizing radiation reach the readout electrodes without any type of amplification. The electric field applied in the system is high enough only to prevent

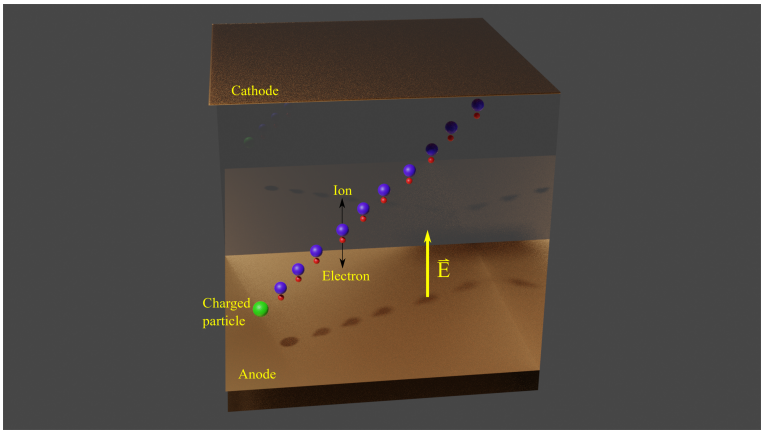


Figure 3.1: Basic principle of operation of a radiation detector that directly collects the charges produced by ionization.

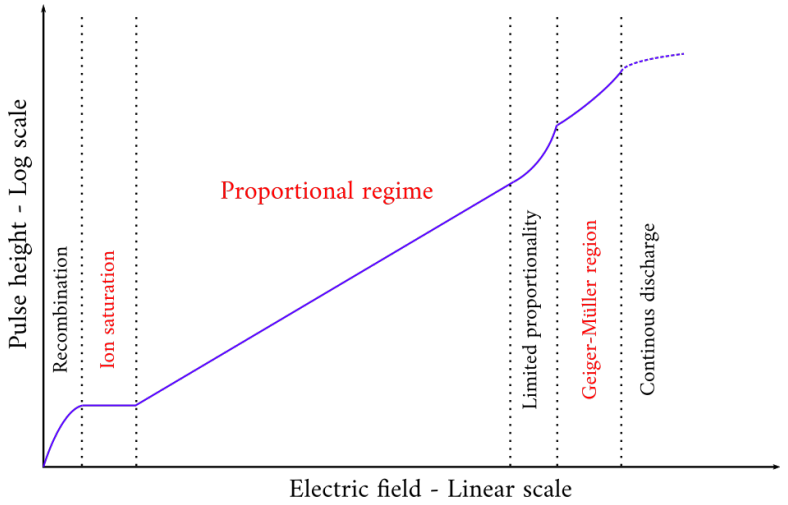


Figure 3.2: Regions of operation of gaseous detectors. Adapted from [14].

pair recombination and to avoid non-linear effects in the signal that is read. A small increase of the electric field in this region does not change the pulse height, since the multiplication threshold is not reached. The most famous type of detector operating in this regime is the ionization chamber, which consists of a recipient filled with gas with two electrodes (anode and cathode) that measures directly the current induced by the products of the ionization.

The primary electrons generated, which are very few, a charge of the order of atto-coulomb (10^{-18}), are generated in a region that operates in the ion saturation regime. They drift to region that operate in the proportional regime and there they are multiplied. To reach the multiplication threshold, an electric field of the order of 10^4 V/m for typical gases at atmospheric pressure is required [14], accelerating the electrons and giving them enough kinetic energy to create new electron-ion pairs and sustain the so called Townsend avalanche process(fig. 3.3). This is the region of operation of the Micropattern Gaseous Detectors (MPGD), which will be described in detail in the following sections. In the proportional regime, the output signal has a height that is proportional to the energy deposited in the detector.

If the electric field is further increased a region where the proportional regime is not valid is reached and non-linear effects become dominant. This is the Geiger-Müller region. Working at this level of field intensity an electrical discharge is generated in the whole volume of the detector, independently of the deposited energy. In this discharge, the energy information is completely lost since all signals have the same amplitude. Detectors such as the Geiger-Müller counter are widely used to measure the activity of radioactive sources. By further increasing the electric field the dielectric breakdown potential can be reached leading to a continuous discharge inside the detector impairing the operation of the device.

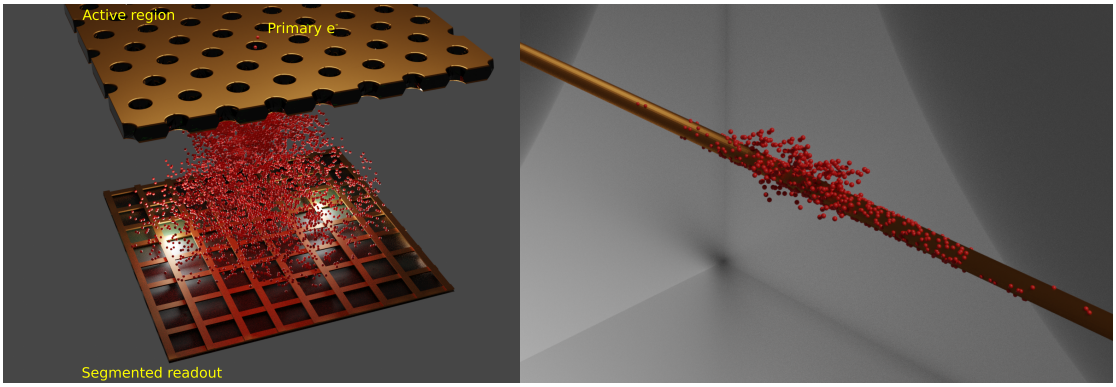


Figure 3.3: Artistic representation of the charge multiplication processes through Townsend mechanism inside a gaseous detector. Left: The primary electrons (very few produced in the active region represented as red dots) drift towards the GEM holes gaining enough kinetic energy to generate new ionization. The final charge is collected by a readout system. Right: Single wire proportional detector. The high electric field in the vicinity of the wire generates a multiplication region for the electrons. Drawings are not to scale

3.1 The single and multi wire proportional detectors

The single wire detector consists of a cylindrical vessel filled with gas, where a single conductive wire is stretched along the axis. A positive high voltage applied to the wire that serves as the anode, creates a multiplication region in its vicinity. The charge that drifts towards this anode is multiplied. Figure 3.3 shows an artistic view of the multiplication of electrons in the vicinity of the wire. The electric field caused by the wire can be calculated using Gauss's law. It is inversely proportional to the distance.

The Multi Wire Proportional Chamber (MWPC) [5], created by Georges Charpak (1992 Nobel laureate in Physics due to this invention), is an extension of the single wire detector. In this detector, several wires are placed in parallel to each other spanning a wide area. Two cathode planes are placed above and below the plane defined by the wires as figure 3.4 shows. The cathode planes can be structured in strips (or also wires) givin position sensitivity to the detector. Due to the possibility to detect position and energy simultaneously, the MWPC played an important role in particle and nuclear physics experiments, being the readout plane of detectors like the Time Projection Chambers (TPC) (e.g. [33]) and Tracking Chambers (e.g. [34]).

3.2 Microstrip Gas Chamber

The MWPC was implemented in most of the large High Energy Physics experiments in the world. However, its manufacture process was tedious and the development of the experiments started to expose some limitations in the performance of these detectors, namely in terms of

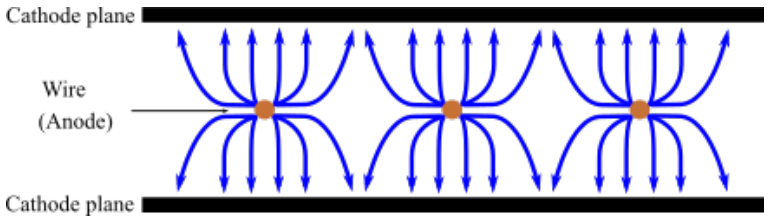


Figure 3.4: Representation of the MWPC principle. A set of wires creates several multiplication regions and the collection of charge in each one of them can be used to determine the interaction position inside the gaseous volume. The blue arrows represent the electric field lines.

counting rate and position resolution. The MPGDs were invented to overcome some of these problems. The first MPGD developed was the Microstrip Gas Chamber (MSGC), created by Anton Oed in 1988 [7]. In the MSGC, alternated thin strips of anodes and thicker cathodes are etched on a dielectric substrate. By applying a potential difference between these electrodes it is possible to create a multiplication region in the vicinity of the anode strips.

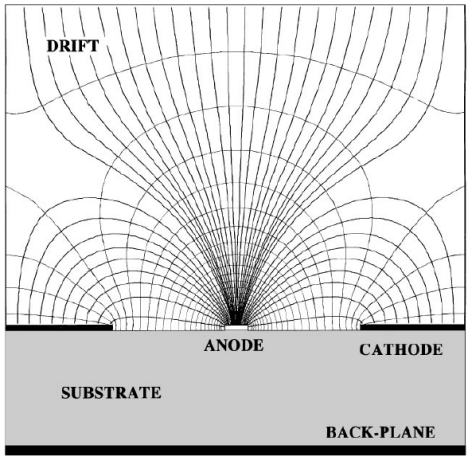


Figure 3.5: The MSGC, with the electric field and equipotential lines represented. A drift field is defined and electrons are pulled towards the anodes where they are multiplied. Image from [35].

The pitch between anode strips is of the order of 200 µm. The cathode strip, placed in between two different anodes, is wider than the anode as it can be seen in figure 3.5. The production of these devices follow high resolution photo-lithography processes. The MSGC has the advantage to neutralize ions short after they are created by the multiplication, differently from the MWPC, where the ions flow back towards the drift region and are neutralized after a long drift time, by a conductive grid or the cathode plane. This makes the detector faster, supporting higher counting rates. Due to the very dense pattern and small width of the anode strips, these detectors are very sensitive to sparks that are very common in gaseous detectors. Therefore, the gains that were possible to achieve with them were limited. The damage created by a spark can be seen in fig 3.6.

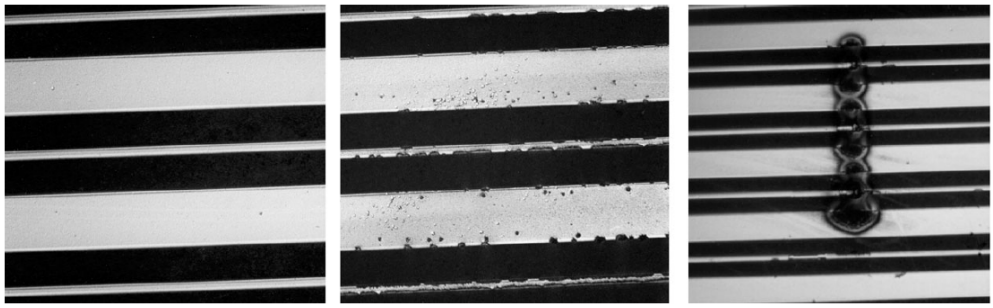


Figure 3.6: Aging issue on the MSGC. The first image shows a plate before its use, followed by a plate after a certain amount of micro discharges and the last image shows the damage after a major spark on the electrodes. Pictures by F. Sauli from [36].

3.3 Micromesh Gaseous Structure

The MICRO MEsh GAseous Structure (MICROMEGAS) was developed by Yannis Giomataris in 1996 [9]. This structure consists of an mesh electrode placed typically around 100 µm above the readout anode, defining a multiplication region. To sustain this structure, insulator pillars are used as spacers. Figure 3.7 shows the working principle of this detector. The radiation deposits energy in the drift region and the free electrons drift towards the multiplication region, defined between the micromesh and the readout electrode. The strip readout provides the position sensitivity.

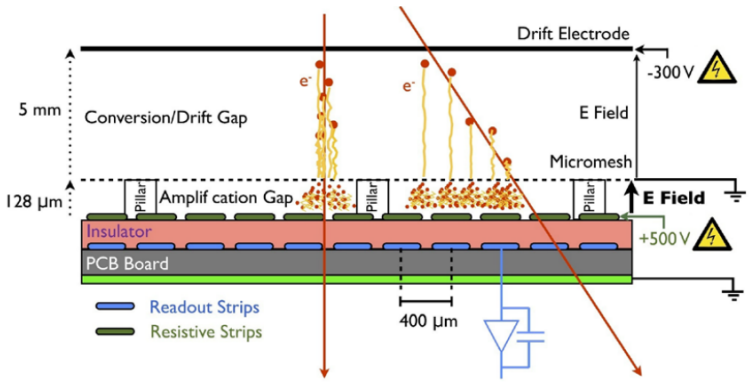


Figure 3.7: MICROMEGAS design for the ATLAS NSW. Image from [37].

An actual use of the MICROMEGAS can be found at the New Small Wheels (NSW) of the Muon Spectrometer of the ATLAS experiment [38]. The detector is composed of 8 MICROMEGAS layers for tracking in combination with 8 sTGCs (Small Strip Thin Gap Chambers) for triggering. Each wheel is composed of a set of two MICROMEGAS sandwiched by two sTGCs . One of the main advantages of this structure is the small dead time, about 100 ns, since the multiplication region is very narrow. Nowadays, MICROMEGAS are covered with an additional resistive layer on the top of a thin insulator, with that it is possible to decouple

the readout plane from the high voltage and to protect the system from sparks [37], achieving higher gains.

3.4 Gas Electron Multiplier

The Gas Electron Multipler was created by Fabio Sauli in 1997 [8] and it was originally conceived to be a first multiplication stage for the MSGC, increasing the gain and protecting the strips from discharges caused mainly due to the high potentials applied. It was observed however, that the GEM itself was able to operate at a very high gain, without the need of the MSGC, allowing it to decouple the charge multiplication from the collection electrode, protecting the readout electronics.

The detector consists of a layer of dielectric material, normally polyimide/kapton, a dielectric polymer resistant to heat and with the expansion coefficient matching the one of copper. This polymer, originally developed for the manufacture of flexible printed circuits, is covered on both sides by a thin conductive layer. By photo-lithography processes and chemical etching, holes are perforated in a hexagonal matrix [35]. The standard GEMs produced at CERN (and used in this work) are made using a 50 µm kapton foil, covered on both sides by a 5 µm copper layer. The holes are etched in a bi-conical shape, with 70 microm diameter at the conductor layer and 50 µm in the center of the dielectric. A typical value for the pitch between holes is 140 µm. Dealing with MPGDs requires a clean environment, in order to avoid the deposition of suspended particles on the electrodes, specially in the holes which may lead to leakage currents and increased discharge probability.

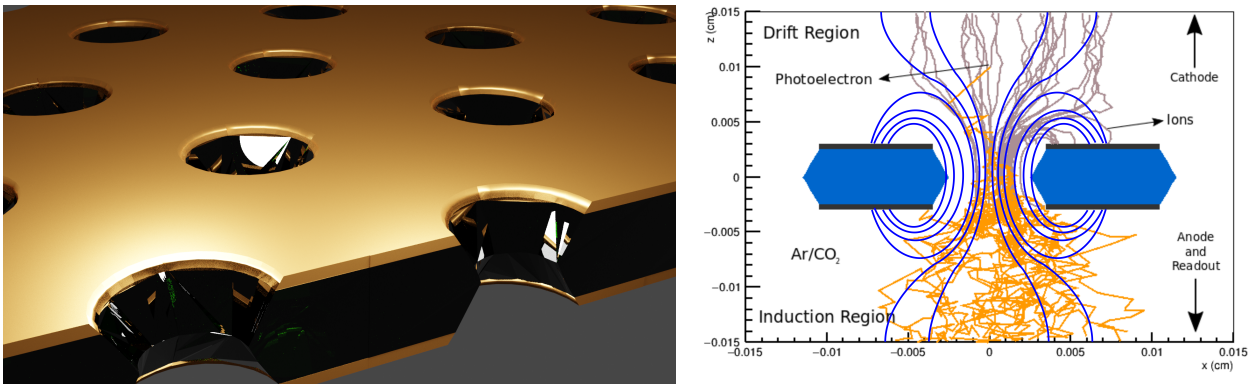


Figure 3.8: Left: 3D model of a GEM foil. Right: Simulation of a Townsend avalanche inside the GEM hole. The orange and gray lines are the electrons and ions drift lines respectively. The blue lines are a representation of the electric field. Figure from [16].

By applying a potential difference between the copper electrodes, it is possible to create electric field of the order of 10^4 V/cm inside the GEM holes, focusing the primary electrons and creating a charge multiplication region. One advantage of using GEMs is the possibility

of stacking several foils, creating multiple multiplication stages with less increase of the high voltages applied, achieving gains of the order of 10^3 for a single multiplication stage and above 10^5 with a triple GEM stack in different noble gases mixtures [39].

One of the problems when dealing with high counting rates is the flow of ions to the drift region (the sensitive volume of the detector), the so called ion back-flow, which may spoil parameters such as the velocity of electrons and ions in the drift region and the position and energy resolutions. The GEM however, provides an intrinsic suppression of ion back-flow. GEM-based detectors allowed operation at higher event rate and substituted the MWPC in different major experiments such as ALICE's TPC [40], the muon detectors of both CMS [41] and LHCb [42], and the COMPASS [43] tracking chambers. The versatility of the GEM detector is an interesting feature since they can be adapted with different coatings of its surface, making it capable of detecting other types of radiation, such as neutron (using ^{157}Gd [44] or ^{10}B [31,45–47] coatings) and UV photons (using, for example, a CsI photo-cathode [48]).

3.5 The time projection chamber

Although the focus of this work is in X-ray fluorescence imaging, both the GEM detector and the SAMPA chip were developed in the environment of high energy physics experiments, mainly for application with Time Projection Chambers (TPC). Therefore, we dedicate this section to present the concept, which will also be explored within this work. The TPC was introduced by David Nygren in the late 1970s [6], when he proposed a chamber that was capable of reconstructing the 3D trajectory of charged particles and, by doing so, to identify the products after a collision. Figure 3.9 illustrates the basic principle of operation of a TPC. A highly energetic charged particle deposits part of its energy in the gas, thus creating a track of electron-ion pairs. Applying a uniform electric field across the TPC volume, the electrons are directed towards a specific direction, where they are collected by a readout plane that multiplies the charge with MWPC or, more recently, multiplied by a MPGD and collected by a segmented readout.

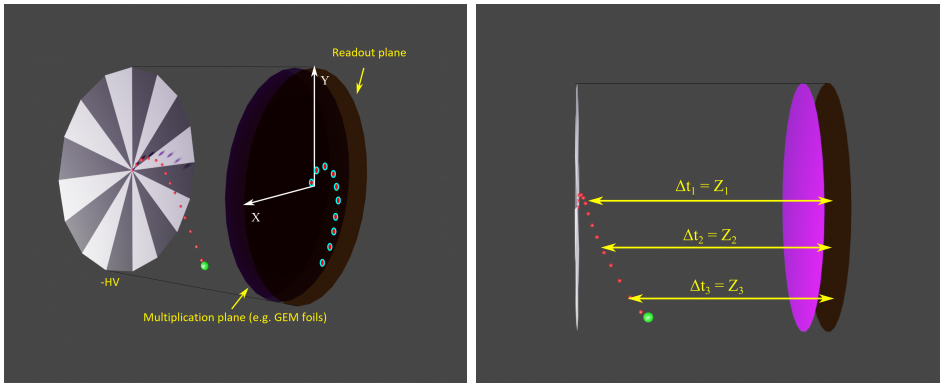


Figure 3.9: Time projection chamber principle. Left: Trajectory projection on the X-Y plane. Charged particles affected by a magnetic field generate a curved track. Right: The Z component is obtained using the charge drift time. Drawing not to scale.

The Z component of the track is determined from the drifting time of the electrons, using the known values of the drift velocity for the gas conditions and uniform electric field. By applying a uniform magnetic field parallel to the electric field, the Lorenz force bends the incoming charged particle and its charge and momentum can be calculated from the bending radius. The energy loss in the TPC can be used for particle identification.

Chapter 4

Detector characterization

To be able to compare capabilities of different detectors a set of measurements can be done in the laboratory or even simulated using different software. The study of these characteristics gives a complete vision regarding the quality of the equipment designed and how it should be located when compared with other equipment. In this chapter the reader will find the definition of some of the parameters relevant to this work, and that can be used to characterize not only gaseous detectors, but also imaging systems.

4.1 Detection or conversion efficiency

The detection or conversion efficiency gives the probability of the system absorb part of the energy and convert the radiation into a signal that can be collected by the readout electronics. In the case of gaseous detectors we also have to deal with the drift of the charge along a path until it is collected and the loss of information during this process must be avoided. To take into account this signal and to extract the best information regarding an event, the detector is tuned in terms of electrodes arrangement, potentials applied and the type of gas that can be used, along with its physicals properties.

As already referred in chapter 2, using the attenuation length coefficient λ and the Lambert-Beer we can calculate the attenuation of a beam with intensity I_0 passing through matter and leaving the material with intensity I. The ratio I/I_0 can be interpreted as the escape probability for a single photon.

$$P(x) = e^{-\frac{x}{\lambda}} \tag{4.1}$$

where x is the length traveled by the photon inside the medium. One can calculate the interaction probability or the conversion probability from the complementary, $1 - P(x)$. After the absorption of the photon, the electrons generated must reach the readout system.

4.2 Collection and extraction efficiencies

The collection and extraction efficiencies are characteristic parameters of GEM detector and are largely dependent on geometric aspects of the foil, such as the distance between foils,

alignments of the holes, pitch and electric field configuration. The charge generated after the radiation deposits some energy in the material drifts through the absorption region of the detector according to the electric field configuration and there is a probability that this electron hits a surface of the GEM foil, instead of being multiplied inside a hole and thus be lost.

To compare and study different experimental setups one can calculate different transport efficiencies for GEMs. One of the main goals of these studies is to achieve the maximum values for each of these quantities in order to get a large amount of information regarding the event and the best possible signal-to-noise ratio. The collection efficiency of a GEM is the capability to direct the charge towards the multiplication region as figure 4.1 shows.

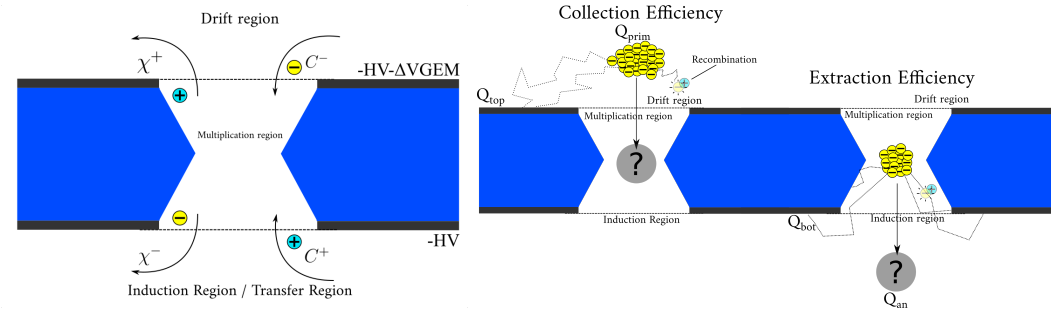


Figure 4.1: Representation of the collection(C) and extraction efficiencies(χ) for electrons and ions. The arrows indicate the direction of movement of the charges.

Considering only the electron charge, the collection efficiency for a GEM foil can be calculated using the following relation:

$$C^{-} = 1 - \frac{Q_{\text{top}}}{Q_{\text{prim}}} \tag{4.2}$$

where Q_{top} and Q_{prim} are the charge deposited at the top copper electrode and the primary charge respectively. The extraction efficiency gives the capability to remove the charge from the multiplication region and direct it towards another GEM or to the readout electrode. It can be calculated as shown below:

$$\chi^{-} = \frac{Q_{\text{an}}}{Q_{\text{an}} + Q_{\text{bot}}} \tag{4.3}$$

where Q_{bot} and Q_{an} are the electron charge deposited in the bottom electrode of the GEM and the readout respectively. In simulations it is possible to distinguish the charge collected that came from ions and from electrons. In the case of ions, the definitions are analogous but the electrodes that are chosen to count the charge are going to be inverted due to the different direction of movement for the positive charge, as figure 4.1 shows.

4.3 Charge multiplication factor and gain

When measuring the charge gain of a detector, one usually compares the primary charge with the charge that reaches the anode, as shown in equation 4.4. This value is a convolution of the charge multiplication in the holes of the GEM foils and the collection and extraction efficiencies. The term 'gain' is widely used to define the effective gain. The multiplication factor of a GEM foil is the average number of electrons that are generated by the electric field in its holes after the collection of one electron. The multiplication factor can also be called absolute gain. It is related to the effective gain by the equation 4.5.

$$G_{\text{eff}} = \frac{Q_{\text{an}}}{Q_{\text{prim}}} \tag{4.4}$$

$$G_{\text{eff}} = G_{\text{abs}} C^{-} \chi^{-} \tag{4.5}$$

4.4 Ion back-flow

Ion back-flow is an effect that can limit gaseous detector performance when operating at high counting rate, especially for TPCs. It can be described as the migration of a very large amount of ions in the absorption region, deforming the electric field, which will not be uniform anymore. This can have consequences such as loss of primary charge due to recombination of the electrons, leading to a loss in energy resolution or, important in TPCs, to the distortion of particle tracks, that has an impact in the physics under study. The definition for ion back-flow given by the number of ions hitting the cathode divided by the number of electrons hitting the anode and can be measure directly from the currents in the anode (I_{an}) and the cathode (I_{cat}):

$$\text{IBF} = -\frac{I_{\text{cat}}}{I_{\text{an}}} \tag{4.6}$$

4.5 Experimental measurements of efficiencies, ion back-flow and gain

The primary current in the detector is determined from the following relationship:

$$I_{\text{p}} = \text{e} N_{\text{p}} n \tag{4.7}$$

where e is the electron charge, N_{p} is the number of primary electrons, that can be calculated using the photon mean energy and the gas work function and n is the event rate. This type

of calculation has a high deviation for non mono-energetic photons, since the mean energy will have a higher uncertainty. The primary current can also be directly measured with an ammeter from either the cathode or the top electrode of the first GEM foil, with the drift region biased and without any voltage across the GEM foils.

IBF and absolute gain can be measured in a single GEM detector, as shown in fig. 4.2 using 4 different ammeters.

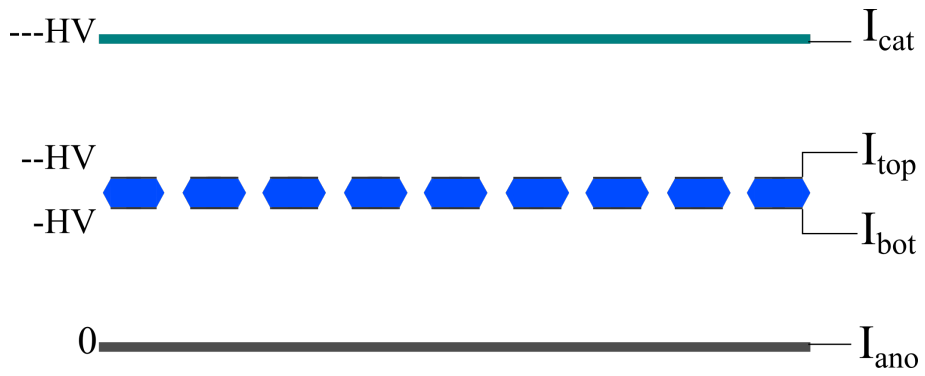


Figure 4.2: Currents used to experimentally characterize the detector.

The cathode current is composed by the primary ions plus the ones that compose the IBF, which are equal to the absolute gain times the extraction efficiency for ions(χ^+).

$$\mathrm{I}_{cat} = \mathrm{I}_p + \mathrm{I}_p C^- \mathrm{G}_{abs} \chi^+ \tag{4.8}$$

The top electrode current is composed by the primary electrons that do not reach the multiplication region and the ions that are not extracted.

$$\mathrm{I}_{top} = -\mathrm{I}_p(1 - C^-) + \mathrm{I}_p C^- \mathrm{G}_{abs}(1 - \chi^+) \tag{4.9}$$

The bottom current is composed by all the electrons that are multiplied but are unable to leave the multiplication region.

$$\mathrm{I}_{bot} = -\mathrm{I}_p \mathrm{G}_{abs} C^-(1 - \chi^-) \tag{4.10}$$

The anode current is the primary current times the effective gain of the detector.

$$\mathrm{I}_{an} = -\mathrm{I}_p \mathrm{G}_{abs} C^- \chi^- = -I_p G_{eff} \tag{4.11}$$

Using the ion back-flow definition from equation 4.6, and equations 4.8 and 4.11, we derive equation 4.12:

$$\mathrm{IBF} = -\left(\frac{1}{G_{\mathrm{eff}}} + \frac{\chi^+}{\chi^-}\right) \tag{4.12}$$

One can see that the ion back-flow is dependent on the gain until at a certain point. For very high gains, the first term goes to zero and only the efficiencies (which are related with field configuration and geometry) will affect the IBF.

4.6 Energy resolution

It is well know that due to statistical fluctuations in the pair creation inside the detector, the number of electrons created after each event will fluctuate (following the Poisson statistics), generating not a well defined line, but a broad distribution around a mean value (more details will be discussed at chapter 5) [14]. The energy resolution of the detector for a certain energy is defined as the full width at half maximum (FWHM) of the distribution divided by the mean energy value (E_{m}).

$$R_{\mathrm{E}} = \frac{\mathrm{FWHM}}{E_{\mathrm{m}}} \tag{4.13}$$

The FWHM of the peak is proportional to the square root of the energy deposited inside the detector (from the Poisson distribution the standard deviation is given by the square root of the mean), therefore it is possible to right the following relation:

$$R_{\mathrm{E}} = K\frac{\sqrt{E_{\mathrm{m}}}}{E_{\mathrm{m}}} = \frac{K}{\sqrt{E_{\mathrm{m}}}} \tag{4.14}$$

where K is a constant of proportionality. This relation shows that for higher energies it is possible to achieve a better energy resolution only due to the decreased relative dispersion with the mean.

4.7 Spatial resolution

The spatial resolution of an imaging system is its ability to distinguish different objects and details. It can be measured by different techniques. Details regarding some of them are going to be discussed in this section. This discussion has been detailed already in a previous work with a similar detector [16].

4.7.1 Point and line spread function

The point spread function (PSF) is a response function of an infinitely small object imaged by the detector. The blurring effect caused by such a response can give a measurement of the quality of an imaging system. This blurring effect all over the image will turn objects indistinguishable as they approach from each other. A quantity related to the PSF and more

used within this work is the line spread function (LSF). The LSF gives the spatial resolution of an imaging system by making an image of a thin slit and projecting the perpendicular profile of this slit on a plane [49]. Ideally, the profile would consist of a delta function where the projection of the slit would be infinitely narrow. However, in a real detector, this projection will spread within a width that corresponds to the detector's LSF. The width of this LSF is the smallest distance at which two different objects can be distinguished. Figure 4.3 illustrates how the image of a thin slit can be recorded by the detector as a distribution with a finite width.

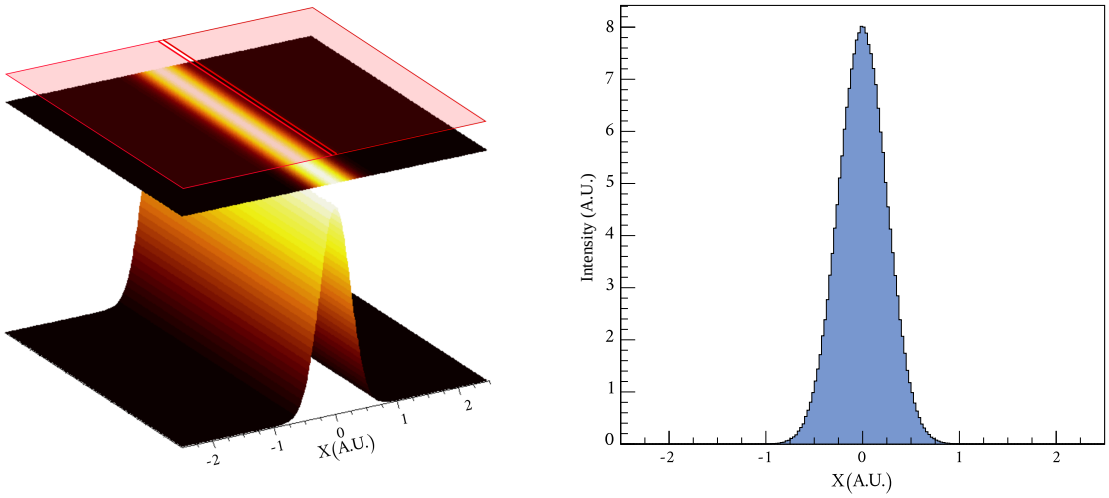


Figure 4.3: Left: Line spread function of an infinitesimal slit. Right: Projection on the X-axis.

Since in the real world it is impossible to create a mask with an ideal slit, normally slits with a width comparable to the position resolution are used. To obtain a quantitative value for the spatial resolution, a Gaussian distribution can be fitted to the slit profile and the standard deviation/FWHM measured. The profile obtained is a convolution between two different distributions, the square profile of a slit plus the LSF (which has a Gaussian distribution) of the detector. Ref. [31] has a detailed description of an empirical method to deconvolute the width of the Gaussian distribution from the square profile of the slit.

4.7.2 Contrast

The contrast is the ability to distinguish between light and dark regions in the image. The contrast radiography image depends on different factors such as the material thickness, the atomic number of what is irradiated, its density and the X-ray beam characteristics [50].

Even with all the parameters related with the detector and the radiation source established at fixed values, the contrast of an image still largely depends on its spatial frequencies. This means that some regions will have a higher contrast than others due to the differences in the size

of the features of the object. The contrast value can be directly measured using the Michelson definition [51], as seen in equation 4.15.

$$C = \frac{I_{max} - I_{min}}{I_{max} + I_{min}} \tag{4.15}$$

where I_{max} and I_{min} represent a bright and a dark spot (in terms of intensity) respectively. The contrast is calculated using the peaks and valleys intensities on the profile image as figure 4.4 shows.

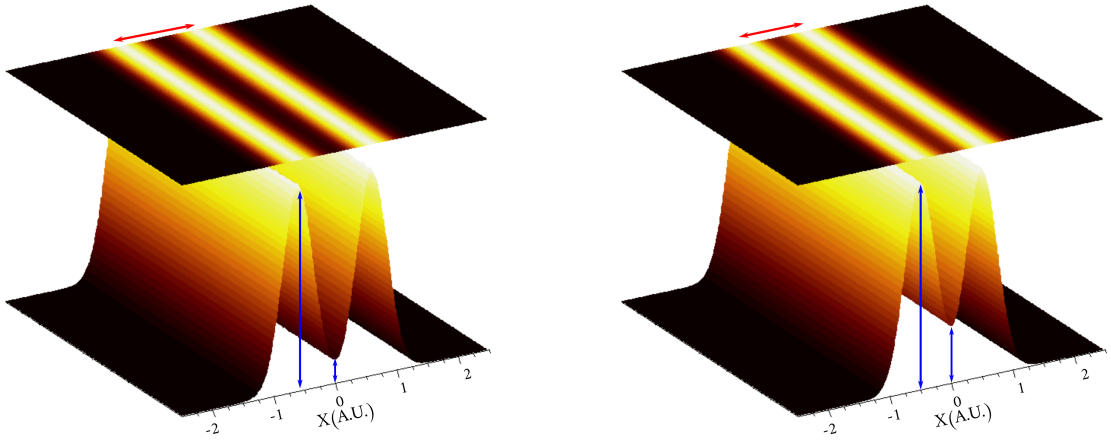


Figure 4.4: Set of slits at different distances. One can see that the closer the slits lower is the contrast.

As it can be seen in figure 4.4 the absolute contrast measured will decrease for closer objects, at a certain point that they will be seen as one single structure. This shows that neither the contrast, nor the width of a slit are enough to define the quality of an image. The variation of the contrast with the spatial frequency (the size of the features) is defined as the Modulation Transfer Function.

4.7.3 Modulation transfer function

The Modulation Transfer Function (MTF) is the response of an imaging system measured in the frequency space. It describes the contrast of a system as a function of the spatial frequencies (or a set of spaced objects at the same distance).

There are two different ways to obtain the MTF of an imaging system. The first way is a direct measure of the response of the system in the frequency space, measured in line pairs (LP) per unit of distance (for example, LP/mm), using an specific resolution mask that has a set of slits separated by a distance that is also their width (see figure 4.5). By measuring the contrast for each set of slits it is possible to calculate the spatial resolution. The absolute value

of contrast will decrease for higher spatial frequencies (smaller and closer objects) and the final resolving power of the detector is assumed to be the MTF at 10 % of contrast [50].

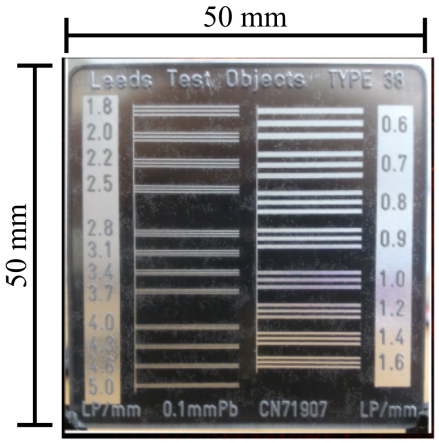


Figure 4.5: Lead mask used for spatial resolution measurements in X-ray transmission imaging. Each set of slits correspond to a spatial frequency in line pairs per millimeter (LP/mm).

The second way is measuring the Line Spread Function and getting the profile perpendicular of a slit. Once you have the distribution, it is possible to apply the Fourier transform on this data. The result (which is going to be a Gaussian distribution on the frequency space) is the MTF [52].

Chapter 5

Simulations

In this chapter we present the results obtained from simulations. The aim is to better understand the behavior of the detector regarding its capability to detect radiation, to find optimal ranges of applications and to understand effects that take place in low energy applications such as X-ray detection. The first studies aimed are the overall detection efficiency of the detector and the energy resolution limits for photons in the range from 1 keV to 30 keV. We have also modeled the contamination of the energy spectrum with X-rays induced from the copper surfaces inside the detector, which is an intrinsic problem when using copper cladding GEM detectors to detect X-rays. We applied a flat-field correction to reduce image artifacts and we model how a peak of energy changes its intensity due to the non-uniform spatial response of the imaging system. Some simulations were conducted using Garfield++ [20], a specific software for charge transport in gaseous detectors and C++ and Python Monte Carlo (MC) code written by the author of this work.

5.1 Garfield++ and HEED

Garfield++ [20] is a framework for simulation of signals in detectors (mainly gaseous detectors but also semiconductors). It was developed at CERN and is based on the Fortran shared libraries from Garfield [53], created by Rob Veenhof in 1984. To make the transport and multiplication of electrons in gas mixtures Garfield++ is integrated with Magboltz [54]. Developed in 1995 by Stephen Biagi, Magboltz solves the Boltzman transport equation, using a Monte Carlo method, for electrons under the presence of electric and magnetic fields in different gas mixtures.

To simulate a full MPGD in Garfield++ two major factors are required, the 3D model of the detector using a mesh for later finite element calculations (that can be build in a software such as GMSH [55]) and the electric field configuration, that can be solved using a specific sofware such as Elmer [56]. The simulations regarding photon absorption were performed using HEED (High Energy Electro-Dynamics), a software written by I. Smirnov that calculates the interaction of charged particles and photons in a gaseous medium [57]. Details regarding the operation of these software can be found on their respective user manual or in the previous work developed by the author [16].

5.2 Detection efficiency and energy resolution

One of the first detectors mounted for X-ray fluorescence imaging in our laboratory consists of a triple-GEM detector, with 1 cm active region depth, that is illuminated through a pin-hole [17]. The first characteristic we want to determine is this instrument's capability to detect an event, in our case, to convert photons into electrons. If we take into account the distance between the radiation source (the sample under analysis) and the detector (in our case 20 cm of air) and that we are using a 50 µm kapton window, almost no radiation below 3 keV is going to be detected. The drift region is the detector active part, the gaseous volume where photons are going to be converted to electrons, multiplied and we performed our MC simulation for two different thicknesses: one with 1 cm and another 3 cm.

The efficiency curves for three different gas mixtures, Ar/CO_2 (70/30), Ne/CO_2 (90/10) and Kr/CO_2 (90/10), can be found in figure 5.1. This efficiency already takes into account the distance between the sample and the detector and the kapton window transmission. The curves were obtained using the transmission and absorption data tables from [58] and the photons were generated perpendicularly to the detector window.

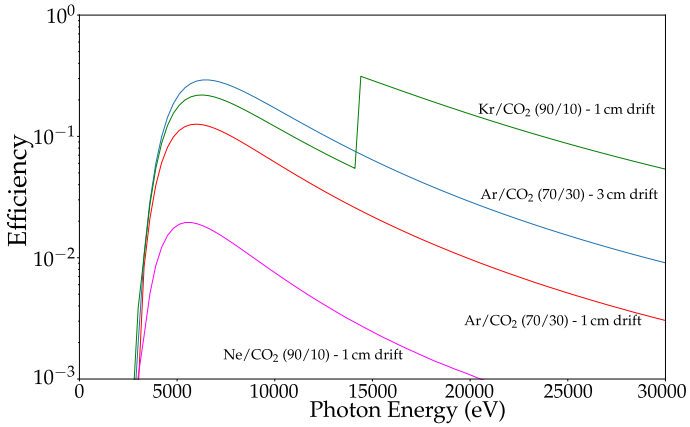


Figure 5.1: Conversion efficiency for three different noble gaseous mixtures for the detector configurations described in the text.

The first thing to be noticed is the low efficiency of neon, being approximately one order of magnitude smaller than the other gases, explained partly by its lower atomic number. Despite the low efficiency, neon may be an interesting gas because it has the advantage of producing an escape peak convoluted with the main characteristic radiation peak (neon fluorescence K_α = 0.848 keV [59]), and so, it will not produce additional peaks in the energy spectrum impairing the identification of elements (a discussion regarding the production of escape peaks will be presented in section 5.3). With a pinhole geometry, the count rate in a detector with neon will be very low, therefore, its use is recommended only if the flux of photons is high. One

can see that for the same thickness of the drift region, krypton shows a higher efficiency when compared to argon and due to the absorption K-edge, above 14 keV krypton shows by far a larger efficiency.

Since we are building gaseous detectors to measure the energy spectrum, one of the most important parameters is the energy resolution. Due to statistical fluctuations higher energies, which are going to produce a larger amount of charge, have better energy resolution. Using Garfield++ [20], more specifically the HEED library [60], we were able to simulate the detection of mono energetic photons, interacting inside a gaseous volume filled with either Argon or Krypton mixtures. We did not simulate neon since this gas is not available in our laboratory and, even if we managed to have it, the relatively low photon flux we usually work with would result in an impractically long acquisition time.

The distribution of the number of primary electrons generated by the 6 keV photons can be found in figure 5.2. These photons were perpendicularly hitting the detector plane, inside the gaseous volume of Ar/CO_2 (70/30) or Kr/CO_2 (90/10), at atmospheric pressure, with dimensions of 10 cm height, × 10 cm width × 1 cm depth. The number of primary electrons is directly proportional to the energy deposited in the drift region, hence the energy of the incident X-ray photons. The secondary peak in the plot on the left is the argon escape peak. Below 14 keV, krypton does not produce a prominent escape peak due to the energy of its fluorescence emission. This effect, which can be an advantage, will be discussed further ahead in this chapter.

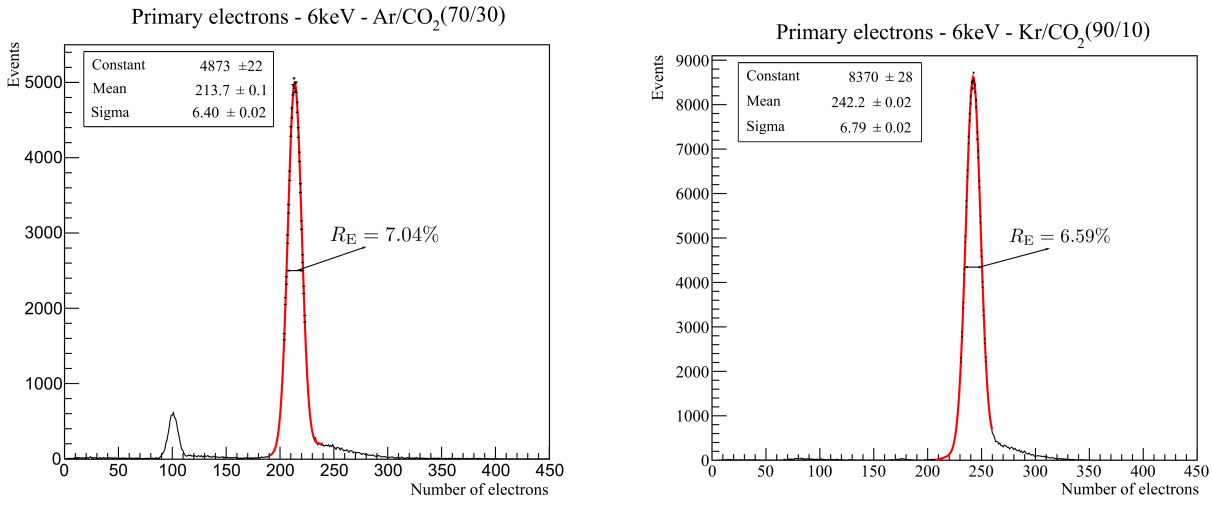


Figure 5.2: Number of electrons generated per event at the drift region by mono energetic photons with 6 keV.

The fluctuation in the number of primary electrons is caused by statistical Poisson processes and since the event that creates charge carriers is not completely independent, a correction to deal with the deviation of the distribution can be applied. The correction is the Fano's factor [4].

The energy resolution limit of a detector can be estimated using the following equation:

$$\mathrm{R_{min}} = 2.35\sqrt{\frac{Fw}{E_x}} \tag{5.1}$$

where F is the Fano's factor for the medium and is 0.23(1) for pure krypton [61] and 0.20(2) for pure argon [62], w is the work function and E_x the energy of the incident radiation. However, this is not the only effect which degrades the energy resolution. Due to the Townsend multiplication mechanism which is in charge of signal amplification in a gaseous detector, the energy distribution becomes wider. The drift field (E_d) was set to 400 V/cm while the induction field (E_i) was kept at 4000 V/cm. Figure 5.3 shows a simulation of the effective gain distribution obtained for different voltages across a single GEM stage.

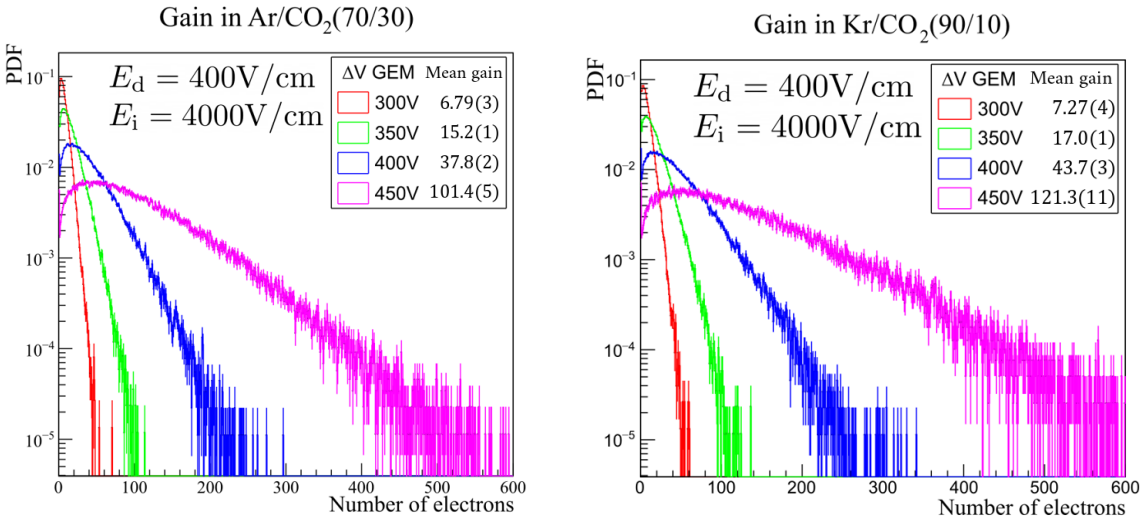


Figure 5.3: Gain distribution as a function of the voltage applied on the GEM electrodes. One can see that the dispersion is wider for higher voltages.

Using this probability density function (PDF) we can use the histogram of primary electrons of figure 5.2 and, by applying a MC method to draw values, obtain a spectrum after multiplication, which can be seen in figure 5.4.

It is possible to notice the energy resolution degradation after multiplication in the GEM foil. We have done the same procedure for two and three GEM foils, however, no considerable difference in the energy resolution was found and this happens mainly because the energy resolution is linked with the processes related to the first GEM as it deals directly with the primary charge. The width obtained in the energy peak is important since it shows the best energy resolution that can be achieved, neglecting other effects such as electronic noise. Using Ar/CO_2, operating at atmospheric pressure, the minimum value that can be achieved is 15%, which can make the identification of neighboring elements in the periodic table more difficult.

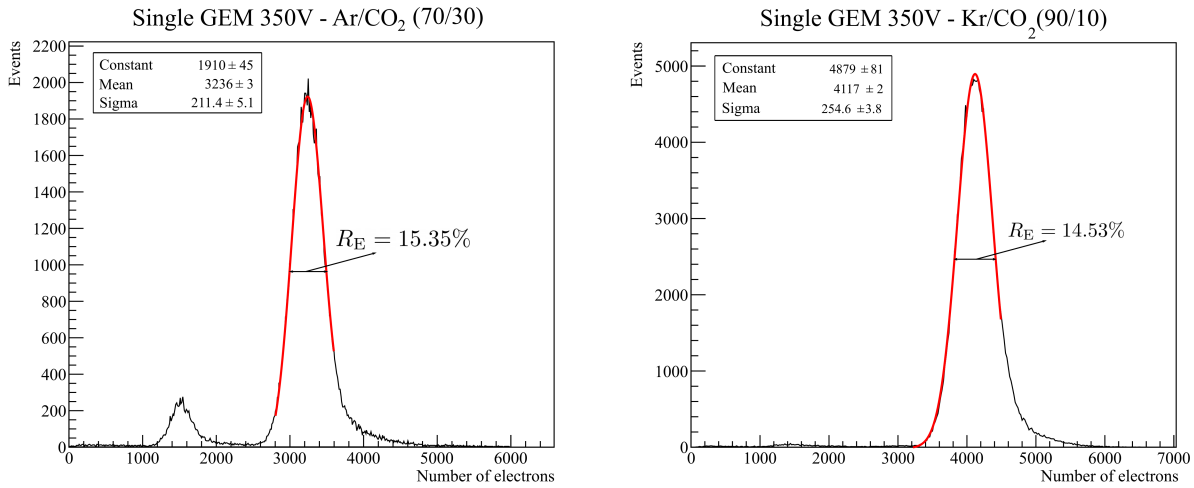


Figure 5.4: Number of electrons generated per event at the drift region by mono energetic photons with 6 keV after multiplication done by one GEM.

5.3 Photon escape probability

In both figures 5.2 and 5.4 we can notice the escape peak, with lower intensity on the left side of the main peak. It is generated when the total energy of an event is not completely deposited inside the detector. The secondary photon, emitted by the atom de-excitation, may not interact inside the gaseous volume and this energy is lost. Therefore, for each fluorescence line detected, an escape peak is expected, generated with a very well defined energy.

One problem faced when we try to identify elements by spectral analysis is the superposition of fluorescence lines detected and escape peaks. To study such effects, one can simulate the probability of a photon escaping as a function of the depth of the drift region and the type of gas used inside the detector. Two different detector models were simulated, one with 1 cm drift depth and the other with 3 cm, both operating with $Ar/CO_2(70/30)$. To calculate the escape probability, points were chosen at regular intervals inside the drift volume (Z-axis scanned in steps of 0.1 cm and the X-Y plane in steps of 0.25 cm) and for each point 10^4 photons were generated isotropically and with energies of 3 keV for argon and 1.59 keV for krypton. The total length traveled inside the gaseous medium was calculated analytically and, using this length, we obtained the escaping probability for this photon, calculated using the Lambert-Beer equation2.1.

Figure 5.5 shows the mean escaping probability for argon (fluorescence energy of 3 keV [59]). One can notice that the escape probability drops by increasing the size of the drift region. Also, by increasing the argon concentration in the mixture we can decrease the escaping probability for the whole detector as figure 5.6 shows. The main factor that contributes to this result is that the interaction cross-section for photons of 3 keV is higher in argon than in carbon

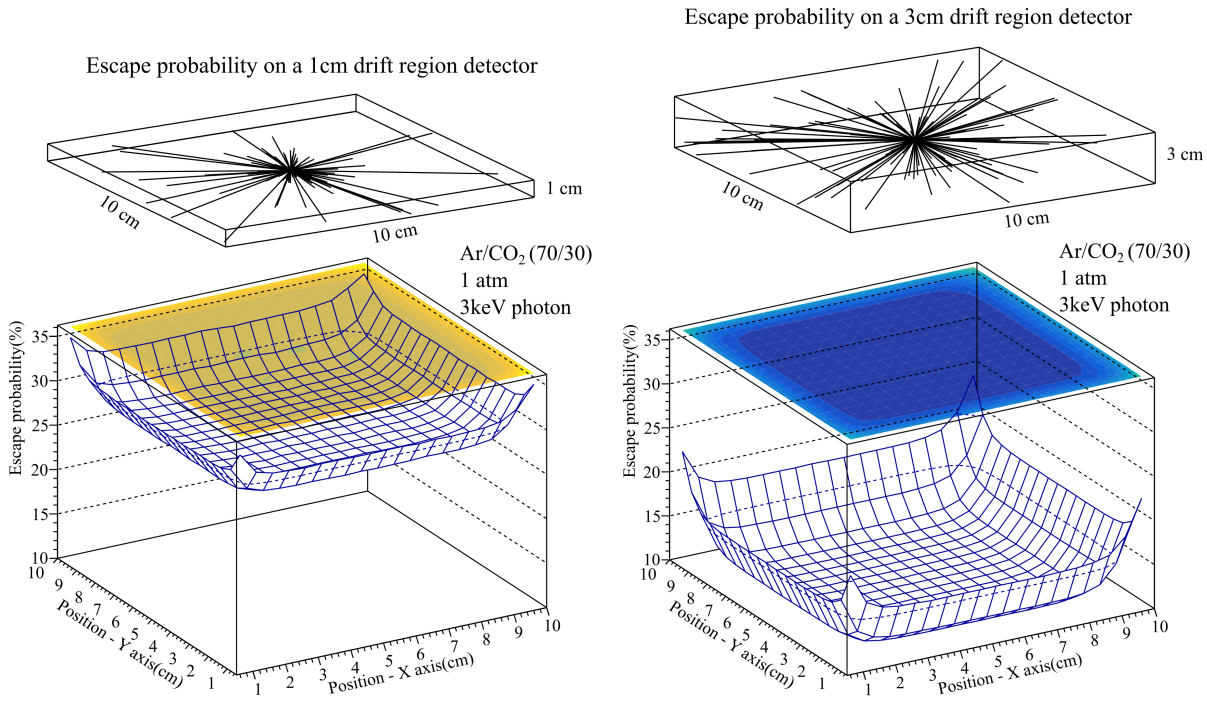


Figure 5.5: Escape probability calculated for two different detector geometries operating with Ar/CO_2 at atmospheric pressure. The escape probability for the drift region of 3 cm is substantially lower, as expected.

dioxide [22]. However, increasing the concentration of argon may affect other parameters such as gain and operation stability in undesirable ways.

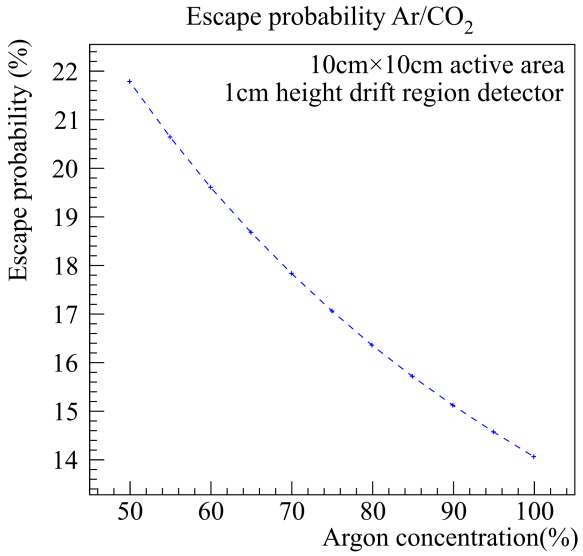


Figure 5.6: Escape probability as a function of the concentration of argon in the gaseous mixture with carbon dioxide.

Finally, if there is the necessity to work with shorter drift lengths, one alternative is to change

the noble gas of the mixture. Krypton only emits the K_α line if it is ionized by radiation with energy higher than 14 keV. For lower energies, the L_α transition emits a photon with 1.59 keV [59]. Since this energy is lower, the probability of reabsorption of these photons is higher, and the full energy of the X-rays are absorbed in the gas as shown by low escape probability depicted in figure 5.7.

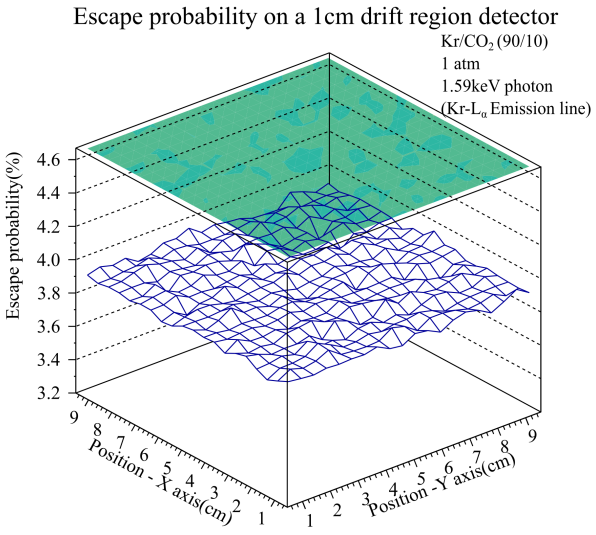


Figure 5.7: Escape probability for a 1 cm drift gap filled with Kr/CO_2. The escape probability is one order of magnitude lower than for the same concentration of argon.

The use of krypton may be interesting for X-ray fluorescence gaseous detectors since it reduces the contribution of secondary escape peaks to the energy spectrum, however other factors need to be considered such as spatial resolution, energy resolution and detection efficiency.

5.4 Spatial resolution

In the case of gaseous detectors, one factor to be studied is the role of the primary electron cloud diffusion and how it will affect the behavior of the device and the reconstruction of the interaction point. Previous studies [63] have calculated the resolution limits by getting the center-of-gravity of all the electrons thermalized positions after interaction but not taking into account secondary effects such as diffusion through a specific geometry. To estimate these effects we simulated a detector similar to the one built for this work (same size and electric field configuration) for the energy range of 1 – 20 keV to understand how the charge multiplication and diffusion affect the position resolution.

The simulation was divided into two parts, the first one used HEED [60] to simulate the photon interaction inside the gas and the distribution of primary electrons in space. The second part was to use previous calculated diffusion coefficients [16] obtained using Garfield++ [20]

(see figure 5.8) to create a fast Monte Carlo transport simulation (with a fixed gas gain of 10^4 for each primary electron). The center of the detector was chosen as the origin of the coordinate system and initial position of the photons. The photons were generated with an incidence angle of 90 degrees with the readout plane and could interact anywhere inside the drift gap.

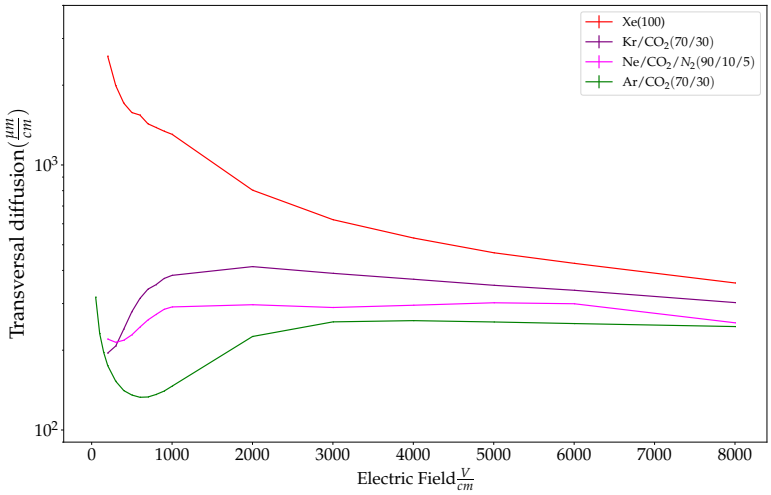


Figure 5.8: Simulation of the transverse diffusion of electrons as a function of the electric field simulated using Garfield++. Adapted from [16].

Figure 5.9 shows the photo-electron tracks obtained for approximately 240 initial photons. The tracks farther from the origin of the coordinate system, pointed by blue arrows, on figure 5.9 (left) are the argon deexcitation photons that interact millimeters away from the initial position.

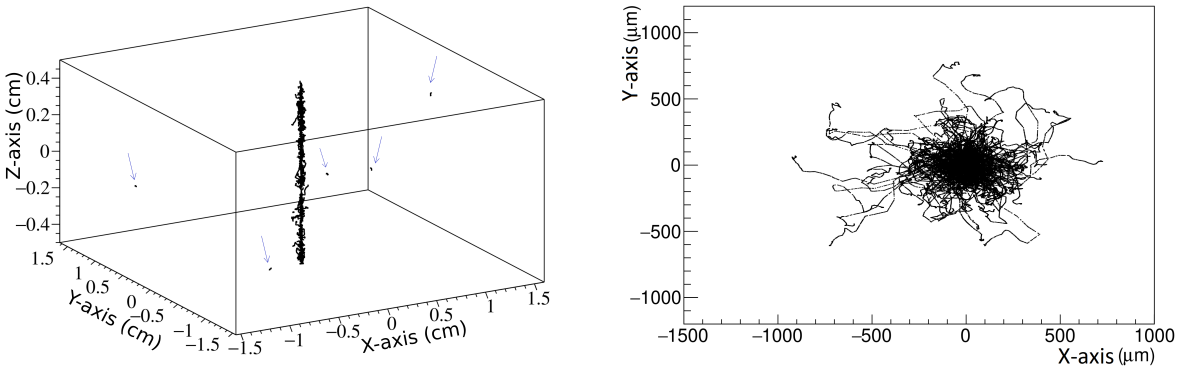


Figure 5.9: Left: Primary electron tracks after first ionization. The scattered tracks farther from the origin are electron clouds generated by the fluorescence of argon. Right: Zoom in close to the origin showing tracks in detail.

Since we want to study the effect of diffusion we have to conduct the complete transport simulation for each electron. Figure 5.10 shows an example of energy deposition for a sin-

gle 8 keV photon. There are two different tracks in this image, the longer one represents the photoelectron that leaves the atom with kinetic energy of 5 keV (initial photon energy minus ionization energy). The second track appears after atomic deexcitation and the argon characteristic X-ray emission. Since charge is quantized, a smoothed heat map (made with a Gaussian kernel available in *SciPy* [64]) has been applied to better visualize the charge distribution in the X-Y plane.

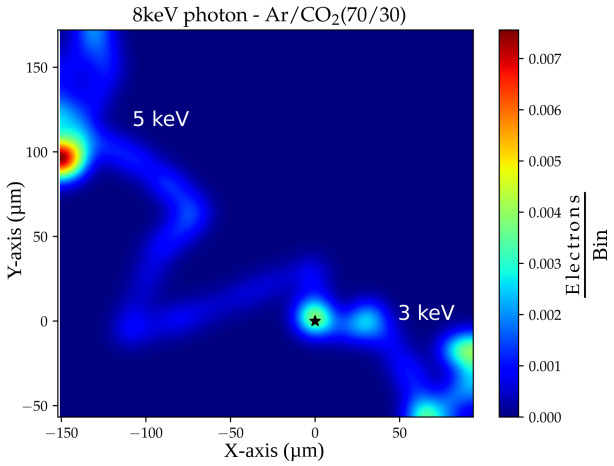


Figure 5.10: Heat map of charge density left by primary and secondary ionization inside the detector. Projection in the X-Y plane. The star marks the first interaction point.

The simulations happen as following: an X and Y coordinates are sorted for each primary electron (these coordinates follow a Gaussian distribution with standard deviation related to the diffusion coefficient parameter for a fixed travel length and electric field) at the end of a drift region with 1 cm thickness and an electric field of 400 V/cm. At the end point of the trajectory of each primary electron, 10^4 new electrons are created - simulating a single GEM detector multiplication with fixed gain and neglecting geometric parameters such as foil thickness or hole position. After that, additional X-Y coordinates, now at the readout plane, are calculated for each electron in the simulation. A new diffusion parameter is used in this case since the induction region thickness and electric field are different (0.55 cm thickness and an electric field of 3000 V/cm).

Figure 5.11 shows the charge distribution at the end of the drift and induction region.

The final position of electrons on the readout plane after multiplication can be seen in figure 5.12. The charge is not distributed centered at the point where the first interaction happened (marked with a star) because the center of mass is biased towards the direction of the 5 keV electrons track. Using a standard center of mass algorithm it is possible to reconstruct the position of the interaction and to evaluate the error between the reconstructed point and the photon interaction point. The center of mass is given by:

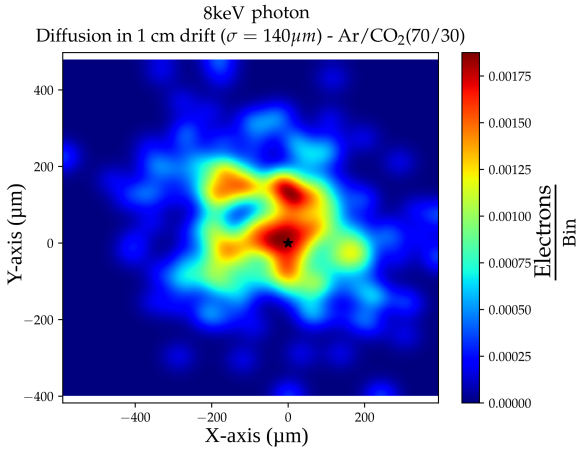


Figure 5.11: Primary electron distribution of the event shown in figure 5.10 at the interface between the drift and induction region. The original interaction point is marked with a star.

$$x = \frac{\sum x_i q_i}{\sum q_i} = \frac{\sum x_i q_i}{Q} \tag{5.2}$$

where q_i is the charge collected at point x_i.

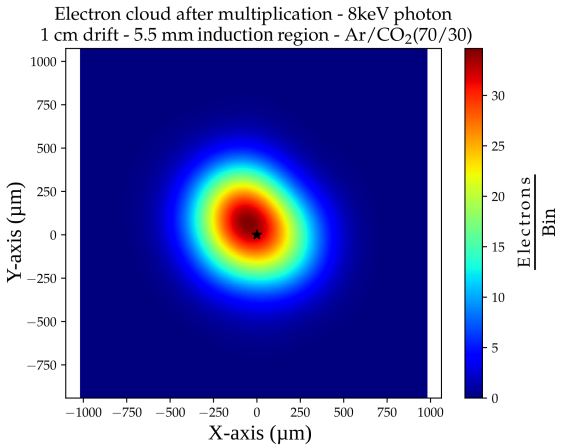


Figure 5.12: Electron distribution at the readout plane after charge multiplication. The interaction point is marked with a star.

To study the position resolution limits for different noble gases mixtures, we calculated the diffusion, multiplication and the center of mass of approximately 40000 different primary tracks in steps of 1 keV between 1 keV and 20 keV. For each energy, a histogram of the reconstructed position was generated and a double Gaussian fit was made. We choose the option to fit a double Gaussian function (both with the same mean) in order to obtain a better chi square to number of degrees of freedom ratio. In fact, it can be considered that there is a convolution of two distributions: the first one (with lower error in the reconstruction) that represents events where both primary and secondary ionization happened close to each other, or in the case of low energy

photons (below the absorption edge of the gas) where only the first photo-electron is present; the second distribution appears as a broader peak with lower intensity, and is related to the increasing error in the reconstruction generated by the atomic deexcitation photon interacting far from the primary interaction point. Figure 5.13 shows the fit for one of the histograms. The position resolution was considered as the FWHM of the Gaussian with larger amplitude. The position resolution limits in pure noble gases was studied previously [63], however with a different approach, considering only the primary electron distribution in space. The effect of the diffusion through the detector and also the charge multiplication was not considered. These effects may play a larger role in gases such as xenon, where the diffusion coefficient is large for lower electric field (normally kept to lower values to maximize the collection efficiency of electrons).

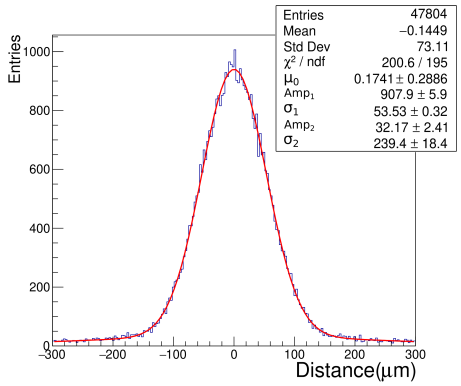


Figure 5.13: Reconstructed position using center of mass algorithm for different photons with 7 keV in Ar/CO_2 mixture.

Figure 5.14 shows the position resolution calculated for argon and xenon mixtures, and we compare with the previous study [63] (in order to validate the simulation but also to check the differences that appear by adding the diffusion effect).

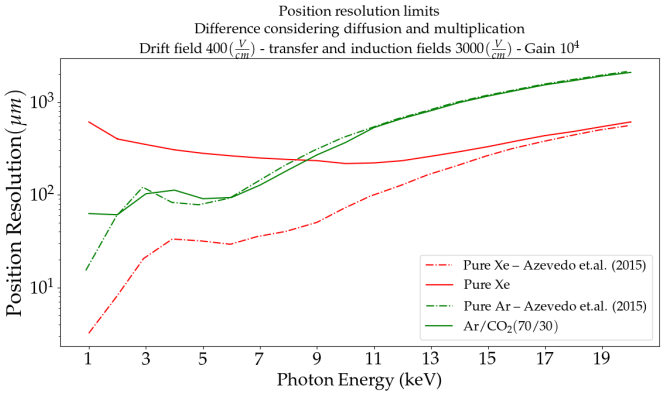


Figure 5.14: Position resolution limits calculated for different gas mixtures. The diffusion plays a larger role for lower energies. The dashed lines data are from [63].

It is possible to see that, in the case of xenon, where the diffusion coefficient is higher for lower electric fields (see figure 5.8), there is a large difference in the position resolution limits for lower energy photons. This behavior is related with the small number of primary electrons and with a higher transverse diffusion in the drift region, generating larger uncertainties. By increasing the photon energy one can see that the error is reduced due to smaller relative statistical fluctuations. The effect of the diffusion is suppressed by the larger number of primary electrons until a certain point. As the photon energy increases, longer tracks are created, depositing energy on a larger region, going in the opposite direction and increasing once again the uncertainties related to the reconstructed position.

In the case of argon, where the diffusion coefficient is smaller, the discrepancy between simulations is small due to the very low transverse diffusion in the Ar/CO_2 mixture. Figure 5.15 shows the resolution limits for different gas mixtures.

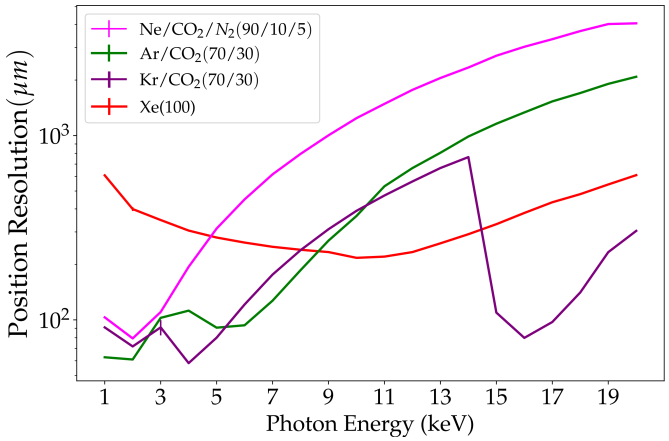


Figure 5.15: Spatial resolution limits calculated using the fast Monte Carlo transport simulation, and considering the electron diffusion effects inside the detector for different noble bases.

The difference between the primary interaction point and the reconstructed position is smaller for lower energy photons and this happens mainly due to the compact primary electron cloud that is created by these photons. In the case of krypton, the resolution is better for photons above 14 keV due to the absorption edge. At these energies, the kinetic energy of the photo-electron is small, leading to a photo-electron that stops in a very small range. The subsequent fluorescent electron either escapes the detector or contributes to the noise in the final image.

This spatial resolution simulation does not take into account two aspects in the reconstruction algorithm. The first one is the presence of electronic noise: it is known that this will affect the events where the total amount of charge generated is small (low energies). The second one is the readout geometry that is used. To understand how the readout electrodes will affect the charge collection and reconstruction of an event, an additional set of simulations were conducted and are presented in the next section.

5.5 Simulation of the readout system and reconstruction algorithms

For a bench top and portable detector the strip-like readout has a major advantage in terms of resolution per number of electronic channels, when compared with pixelated readouts. However, they have limitations when an excessive number of events comes within the same acquisition time window. If one or more interactions happen in the same set of strips but at different positions, part of the information is lost and artifacts may appear in the image.

The readout consists of two stacked planes of parallel conductive strips, rotated by 90°, with respect to each other as illustrated in figure 5.16. The charge is collected independently for each strip and the signal is processed by a standard chain of charge sensitive preamplifiers, shapers, discriminators and an analog-to-digital converter. The interaction point is reconstructed by a center of mass algorithm.

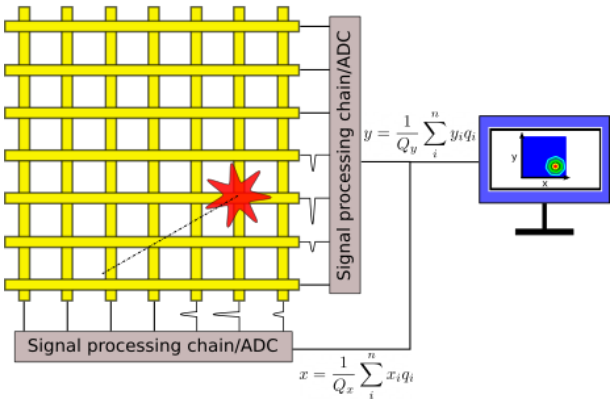


Figure 5.16: Example of a 2D strip readout system.

With strips crossing each other it is possible to create virtual pixels that have the size related with the readout pitch. This is an advantage when compared to a pixelated readout with pads since a smaller number of electronic channels will be needed to cover the same area. Since we are reading a continuous distribution of charge with a discrete system, we add a position dependent systematic error. To estimate the errors and to minimize the artifacts that may appear in our image we have conducted several simulations that take into account the parameters shown in figure 5.17, such as the electron cloud diffusion (σ), the readout pitch and the strip width. In this toy model simulation we have included a response function for the readout, modeling the charge collection by the electrode plane, that is, all the charge that hits a strip is collected and electrons that hits the readout plane between two adjacent strips are lost (see figure 5.18). Several additional features such as noise and the application of a zero suppression threshold, i.e. removing from the center of mass calculation the strips where the charge does not reach a minimum threshold value can be applied.

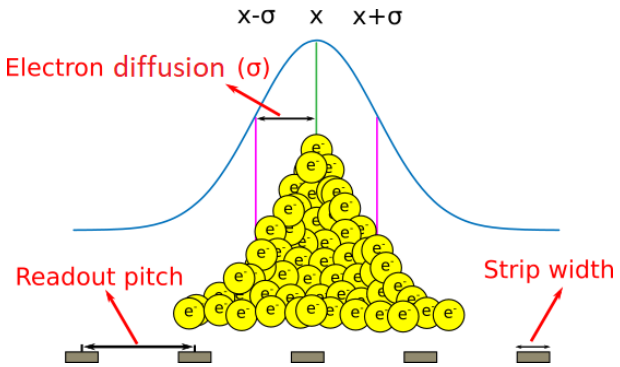


Figure 5.17: Simulation parameters that can be changed in order to study the precision of a segmented readout system.

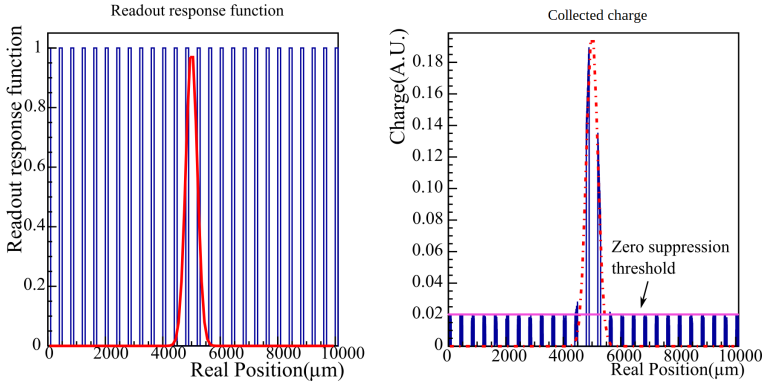


Figure 5.18: Left: Readout response function. In red it is possible to see the projection where an electron cloud hits the readout. Right: Collected charge in an event with the noise contribution being taken into account. The pink line indicates the zero suppression threshold.

By using the center of mass algorithm we can reconstruct the interaction position, using parameters that are similar to the ones used in our laboratory (strip width = 100 µm and pitch = 400 µm). Since we know exactly where the center of the simulated electron cloud is, we are able to calculate the deviation between the real and the reconstructed position, which can be defined as:

$$\epsilon_x = x_r - x_c \tag{5.3}$$

where x_r is the real position and x_c is the reconstructed position.

We may also define an error for 2D images, which will be:

$$\epsilon_r = \sqrt{(x_r - x_c)^2 + (y_r - y_c)^2} \tag{5.4}$$

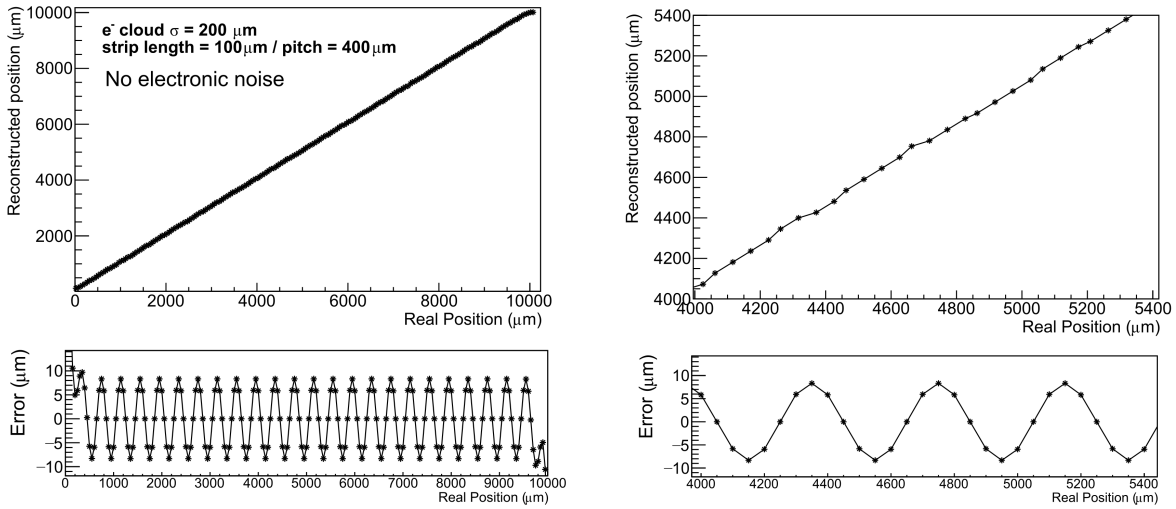


Figure 5.19: Left: One-dimensional reconstructed position of the interaction point as a function of the real position. Right: Zoom in on the left image.

By scanning the readout plane along one direction with this Gaussian function representing an electron cloud, we can calculate the deviation between the point where the electron distribution is centered and the reconstructed position. In figure 5.19 we show a plot of the one-dimensional reconstructed position as a function of the real interaction point for $\sigma = 200\,\mu\text{m}$. Taking a closer look at the residuals, we can see that it has a clear periodicity that induces a specific artifact into the reconstructed images: the mesh artifact.

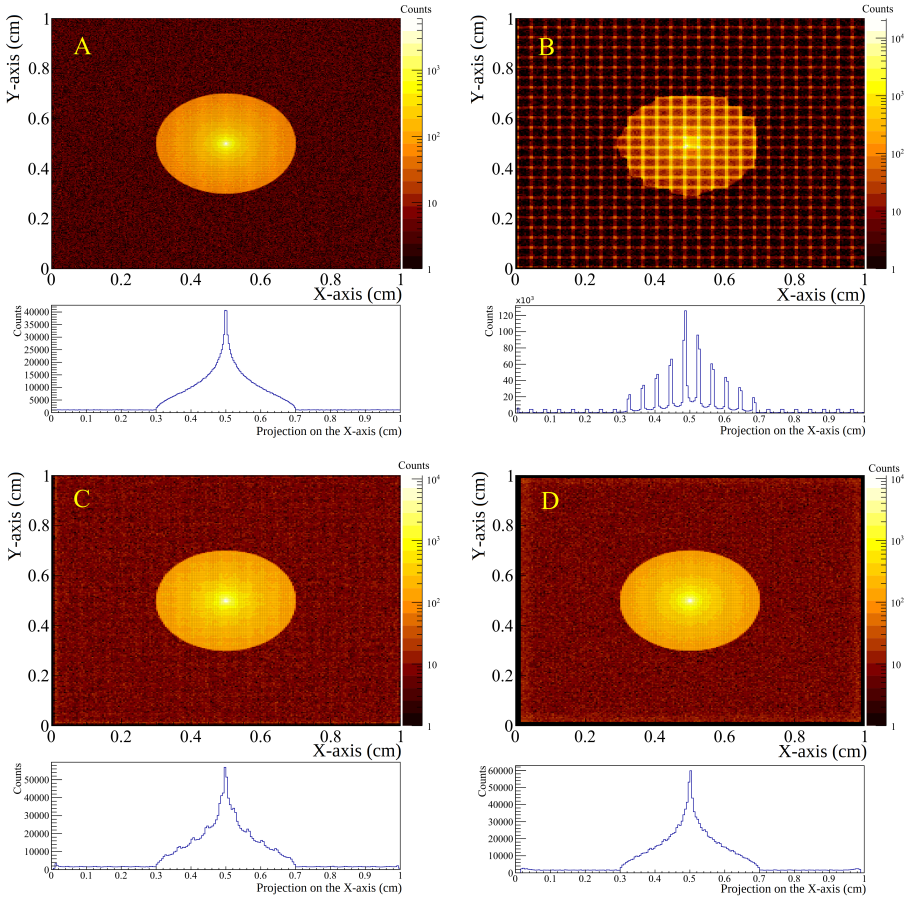


Figure 5.20: A: Ideal image. B, C and D are the reconstructed images with the electron cloud $\sigma =$ equal to 100 µm, 200 µm and 300 µm respectively. One can see that by increasing the dispersion of the electron cloud and consequently the strip multiplicity the artifacts are mitigated.

We can use the same readout response function, now for 2 dimensions, to simulate the imaging of an object. Figure 5.20 shows the detector response to an object that could be thought as a round hole drilled into an opaque mask. It is possible to see a set of reconstructions of the same round object but with different dispersion parameters. Image 5.20-A shows the distribution of the real position of the interaction points in the detector. The readout strip mesh artifact can be clearly seen in figure 5.20-B. In this case the high luminosity circle is completely affected. Figure 5.20-C shows a result that is similar to the one obtained in the laboratory, where the image reconstruction is not perfect but the main aspects of the sample are present and its identification is not compromised, nevertheless we can see the readout pattern shadow and a modulation in the profile. Figure 5.20-D shows that for large widths of the charge clouds, the readout pattern is not a problem, due to the large multiplicity of strips. Therefore, it is important to notice that using threshold levels that are excessively high may worsen the image reconstruction, causing low strip multiplicity resulting in an increased systematic error and the presence of artifacts.

As presented in chapter 4, one method that is widely used to characterize image detectors is

the modulation transfer function (MTF). In this method the contrast of the image is measured for different spatial frequencies and by looking at its values it is possible to define the system resolution. If the readout pattern creates a modulation in the whole image, the result of the test of characterization is affected leading to an incorrect determination for the position resolution. Since this error is intrinsic to the measurement and can only be reduced but not completely eliminated, one thing that can be done is a post processing analysis called flat field correction.

5.5.1 Flat-field correction algorithm for strip readouts

The flat field correction is an algorithm used to improve the quality of digital images by leveling the sensibility of pixels. This method is used to calibrate many different imaging systems such as telescope lenses, CCD devices [65] and microscopes [66]. In our experimental setup we do not have pixel structures, however, the intersection of strips will create a pixel like structure, with size related to the strip pitch. For simplicity, in this section we are going to refer to these structures as pixels.

The method consists of illuminating the detector evenly, generating a flat field image. Later, after making an image of the desired sample, we divide it by the flat field image, balancing the brighter and darker pixels. In the general formula, the counts in each pixel are the sum of background noise with a convolution of the light intensity distribution with the pixel sensitivity [66]. Since in our detector we have a variation in brightness that follows the readout pitch, we can use a slightly different algorithm that takes into account not individual pixels but the complete projection along a direction. The use of the profiles, instead of the 2D distributions for the flat field corrections, takes advantage of improving the correction due to the better statistical quality of the 1D profiles.

To obtain the correction parameter ($C(i,j)$) for a pixel with bin coordinates i and j, first we need to create two 1-D projection histograms of the flat field image, P_x and P_y. Then, we need to get the number of entries in each bin of these histograms($N_x(i)$ and $N_y(j)$) and the average number of entries over all bins from the projection histograms($\bar{N}_x$ and $\bar{N}_y$). The parameter then can be obtained using the following equation:

$$C(i,j) = \frac{N_x(i)}{\bar{N}_x}\frac{N_y(j)}{\bar{N}_y}$$

$$\bar{N}_x = \frac{\sum_{i=0}^{A} N_x(i)}{A}, \bar{N}_y = \frac{\sum_{j=0}^{B} N_y(j)}{B}$$

where A and B are the number of bins for the projection histograms P_x and P_y respectively. Afterwards, a new image can be generated where the entries in each pixel will be:

$$N'(i,j) = \frac{N(i,j)}{C(i,j)}$$

where $N(i, j)$ is the original number of entries for the pixel with coordinates i and j.

A simulation was made in order to show this principle. Using the same readout simulation from the previous section, we have generated the flat field image (left image of fig. 5.21). We have also simulated a sample with our model, a round object which will appear with higher intensity. It is possible to see that after applying the algorithm, the readout pattern is barely visible. One thing that must be clarified is that the coordinates of the interaction (as shown before in image 5.19) are still shifted due to the reconstruction method using a strip readout plane and they were not corrected by this method. So, the flat field correction affects only the intensity of each bin of the 2-D histogram and does not correct the coordinates of the event.

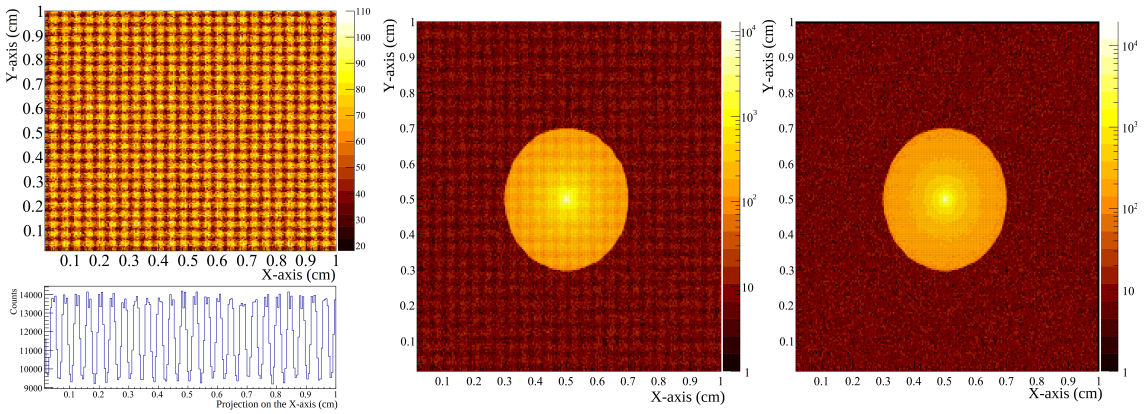


Figure 5.21: Left: Flat field image. Middle: Image before correction. Right: Image after applying the correction algorithm: the readout pattern is barely visible.

We can apply the same algorithm to data obtained with the detector and this will be discussed further in chapter 8. An alternative to strip readout is the use of optical readouts using CCD cameras to mitigate artifacts, to reduce the acquisition time and distortions [67]. These readouts are able to collect the scintillation photons generated in the avalanche when using the proper gas mixture, normally a composition containing CF_4 [68] or gases scintillating in the proper wavelength.

5.6 Copper contamination of the energy spectra.

One of the challenges of using GEMs for X-ray fluorescence imaging is the contamination of the energy spectra, generated by the fluorescence X-rays from the copper surfaces that are present in all the detector's electrodes. Part of the radiation that does not interact in the drift region may hit the copper surface of a GEM foil or the readout, generating fluorescence X-rays. This radiation may reach the active area of the detector and be recorded as an event. The copper has a K fluorescence emission line at 8.05 keV [59], which is close to the efficiency peak of our system, as was shown in figure 5.1. As we have calculated previously, the energy resolution

limit for our detector is in the order of 15% (FWHM) in this energy range and the presence of this peak can jeopardize the identification of elements.

To estimate the contribution of the copper contamination generated and detected, we have studied and complemented a model that is widely used in XRF spectroscopy [69, 70]. The idea is to sum the contributions of all the copper electrodes inside the detector.

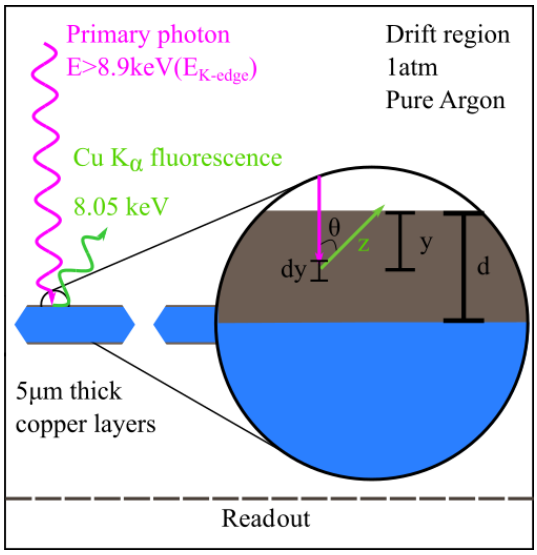


Figure 5.22: How the copper contamination takes place inside the detector, in this specific case, by the top layer of the GEM foil.

Figure 5.22 illustrates the process of the copper contamination of the energy spectrum. The emission of a fluorescence X-ray from a copper layer is a function of the intensity of the original X-rays that reach a certain depth y in the copper surface, multiplied by the fluorescence yield and the probability of interaction with a K-electron, multiplied by the intensity of characteristic copper X-rays transmitted through the same depth of copper into the drift region of the detector. The normalized intensity dI_k of the spectral line K_α of copper, emitted from an infinitesimal thin copper layer dy, can then be expressed as follows:

$$dI_k(\nu_i, \nu_f) = \frac{dI(\nu_i, \nu_f)}{I_0} \propto \frac{d\Omega}{4\pi}\omega_k \frac{1}{\lambda_k(\nu_i)} \exp\left(-\frac{y}{\lambda_{Cu}(\nu_i)}\right) \exp\left(-\frac{z}{\lambda_{Cu}(\nu_f)}\right) dy \qquad (5.5)$$

The first exponential term gives the intensity of the beam (with energy ν_i) that reaches the infinitesimal layer of copper(dy) after traveling a copper length of y. The second exponential is the attenuation of the fluorescence photons (with energy ν_f) that are generated inside this same infinitesimal layer and that pass through a total length z inside the copper (z depends on the angle which the fluorescence X-ray is emitted). The term $\frac{1}{\lambda_k(\nu_i)}$ is related to the differential probability of photon fluorescence emission and takes into account only interactions which generated K-shell vacancies. At a first approximation, for energy above the K-edge, the great majority of the X-ray interactions are with the K-electrons of copper [71], therefore, $\frac{1}{\lambda_k(\nu_i)} \approx$

$\frac{1}{\lambda_{Cu}(\nu_i)}$. The fraction $\frac{d\Omega}{4\pi}$ will give the solid angle of the fluorescence emission and ω_k is the fluorescence yield, that is, the probability of the K-shell vacancy being filled through radiative processes. The value used was 0.433, obtained though the fit in [72].

To obtain the probability of a contamination photon being detected ($d\bar{I}_k$), two extra terms should be included in equation 5.5. The first ($\gamma(\nu_i)$) is related to the beam attenuation until interaction with the copper cladding (that is, the air column between the source and the detector and the window and drift region transmission) and is energy dependent. The second is the probability of detection of the fluorescence photon by the drift region, which is given by Lambert-Beer's law in the form of the copper X-rays that are not transmitted by the absorption region. Taking into account the angle emission, one can write $z = \frac{y}{\cos(\theta)}$ (also applying it to the path inside the drift region), we obtain the following:

$$d\bar{I}_k(\nu_i,\nu_f) = \frac{d\Omega\gamma(\nu_i)\omega_k}{4\pi\lambda_{Cu}(\nu_i)} \exp\left[-\left(\frac{y}{\lambda_{Cu}(\nu_i)} + \frac{y}{\lambda_{Cu}(\nu_f)\cos(\theta)}\right)\right]\left(1-\exp\left[\frac{-D}{\lambda_{Ar}(\nu_f)\cos(\theta)}\right]\right)dy \quad (5.6)$$

where D is the drift region thickness, $\lambda_{Ar}(\nu_f)$ is the argon attenuation length. The total intensity calculated only for the first copper layer of the first GEM is given by:

$$\begin{aligned}\bar{I}_k(\nu_i,\nu_f) = \frac{\gamma(\nu_i)\omega_k}{4\pi\lambda_{Cu}(\nu_i)} \int_0^{2\pi} d\phi \int_0^{\frac{\pi}{2}} d\theta \sin(\theta) \int_0^{d} dy \exp\left[-\left(\frac{1}{\lambda_{Cu}(\nu_i)} + \frac{1}{\lambda_{Cu}(\nu_f)\cos(\theta)}\right)y\right] \\ \left(1-\exp\left[\frac{-D}{\lambda_{Ar}(\nu_f)\cos(\theta)}\right]\right)\end{aligned} \quad (5.7)$$

Integrating over the copper thickness d and in the ϕ angle:

$$\begin{aligned}\bar{I}_k(\nu_i,\nu_f) = \frac{\gamma(\nu_i)\omega_k}{2\lambda_{Cu}(\nu_i)} \int_0^{\frac{\pi}{2}} d\theta \sin(\theta) \frac{1}{\frac{1}{\lambda_{Cu}(\nu_i)} + \frac{1}{\lambda_{Cu}(\nu_f)}\cos(\theta)} \\ \left(1-\exp\left[-\left(\frac{1}{\lambda_{Cu}(\nu_i)} + \frac{1}{\lambda_{Cu}(\nu_f)\cos(\theta)}\right)d\right]\right)\left(1-\exp\left[\frac{-D}{\lambda_{Ar}(\nu_f)\cos(\theta)}\right]\right)\end{aligned} \quad (5.8)$$

or

$$\bar{I}_k(\nu_i,\nu_f) = \frac{\gamma(\nu_i)\omega_k}{2} \int_0^{\frac{\pi}{2}} d\theta \sin(\theta) \frac{a}{a+b\cos(\theta)} \left(1-\exp\left[-\left(a+\frac{b}{\cos(\theta)}\right)d\right]\right)\left(1-\exp\left[\left(\frac{-Dc}{\cos(\theta)}\right)\right]\right) \quad (5.9)$$

where a, b and c are $\frac{1}{\lambda_{Cu}(\nu_i)}$, $\frac{1}{\lambda_{Cu}(\nu_f)}$ and $\frac{1}{\lambda_{Ar}(\nu_f)}$ respectively.

This integral can be solved numerically by making some assumptions to simplify the problem. The first one is that the X-ray source is considered to be very far from the detector window, this way all the photons enter the drift region perpendicular to the detector plane.

The XY plane is considered to be infinite in both directions. The GEM foil holes and the space between the readout strips were neglected. Future corrections can be applied to compensate for imprecision caused by these approximations. To calculate the contribution of the other copper electrodes, more attenuation terms related with the incident and the contamination fluorescence photons were added.

Figure 5.23 shows the contamination contribution for 3 different layers inside a triple-GEM detector, the first and second copper electrodes from the stack and the readout plane. The contributions, shown as a function of the fluorescence emission angle, were calculated using equation 5.6 by applying the additional terms in the case of a triple stack.

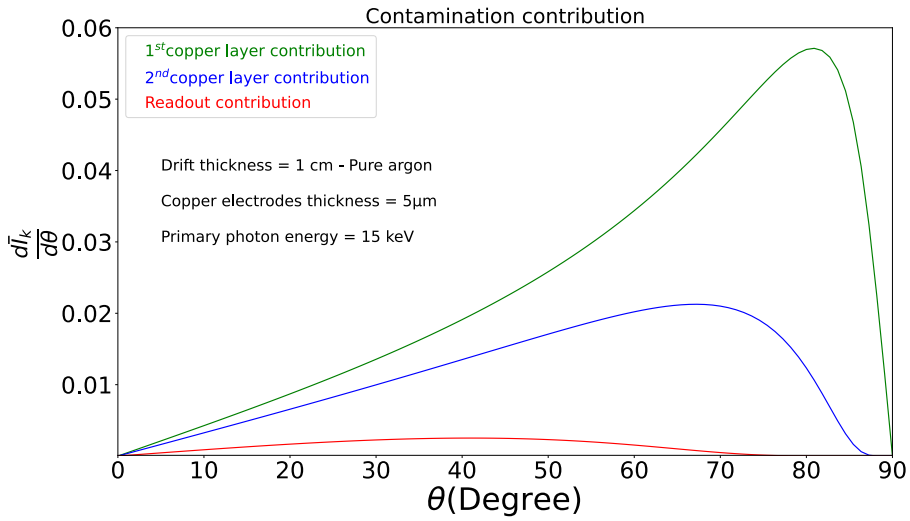


Figure 5.23: Contamination inside a triple-GEM detector.

It is clear that the contribution to contamination from layers which are deeper inside the detector are smaller. By integrating and summing these curves, the total contribution of contamination for a specific detector setup is obtained. Figure 5.24 shows the total contamination for two different systems. The graph on the left shows a triple-GEM detector that has a drift region with 1 cm, while the one on the right has a drift with 3 cm. Both detectors have a copper readout and its contribution was included. Each one of the copper electrodes is 5 µm thick. The value for γ (beam attenuation until hitting the copper) in the first layer calculation was kept equal to the transmission probability in the drift region and for the subsequent layers the terms related to the transmission in other components were added. The fluorescence photons are also attenuated by the same materials after they are generated. The transfer and induction zones were 1.5 mm and 1 mm respectively.

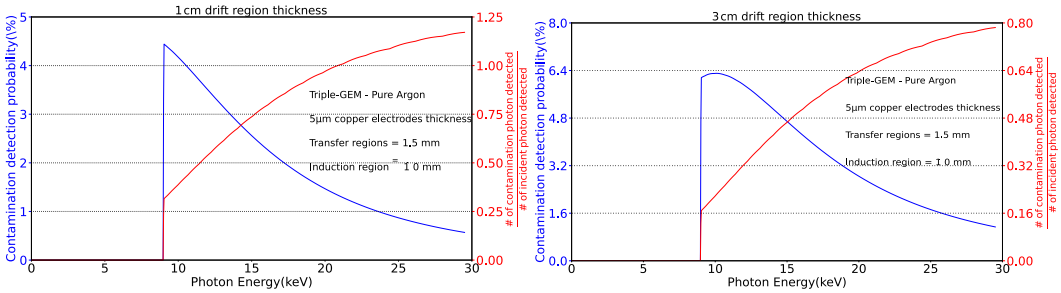


Figure 5.24: Contamination detection probability (blue) and contamination fraction (red) for 1 cm and 3 cm drift thickness.

One can see that the probability to detect a contamination photon (blue curve) has its maximum just above the K-shell absorption edge and then it drops. This happens mainly due to the increase of the attenuation length for higher energy primary photons, while the attenuation length for the copper photons remains constant. In red it is possible to see the number of contamination photons detected that were generated divided by the number of incident photons with energy ν_i. The detector with a thicker drift region has a higher probability of contamination from copper X-rays, but also has a higher efficiency for X-rays above the copper k-edge, resulting in a smaller relative contamination.

One can see that the ratio between contamination photons and incident photons detected can achieve values above 1 for high energies meaning that, above some energies, the amount of contamination in the energy spectrum will be larger than the incident X-rays. The pollution of the energy spectrum can decrease the position resolution of the detector because photons from the copper fluorescence inside the detector create a flat background in the images, decreasing the contrast over the whole active area. Furthermore, they generate extra energy peaks at 8.05 keV and 5 keV(copper escape peak).

Other groups are working in ways to suppress the contamination from the copper cladding. One of the approaches is to remove most of the copper conductive layer and to use only the chromium layer that is used to improve the adhesion between the kapton and the copper layer to bias the GEM foil [73]. Despite the clear contamination suppression reported [74], the process in which these GEM foils are produced is not clear and the chromium may also produce a contamination, with lower intensity, in the region of interest, at 5.41 keV [59].

Another alternative is to use a different cladding for the GEM foils, replacing the copper by other metal, with a smaller atomic number. Aluminum is one of the candidates, with X-ray fluorescence at 1.48 keV which will not hinder the energy spectrum in the region we are interested in [75]. Figure 5.25 shows the total contribution of contamination detected for a aluminum-clad triple-GEM detector operating with a copper readout.

One can see that the probability to detect a contamination photon is small in the system using aluminum GEMs even when the readout and also the ratio between contamination and

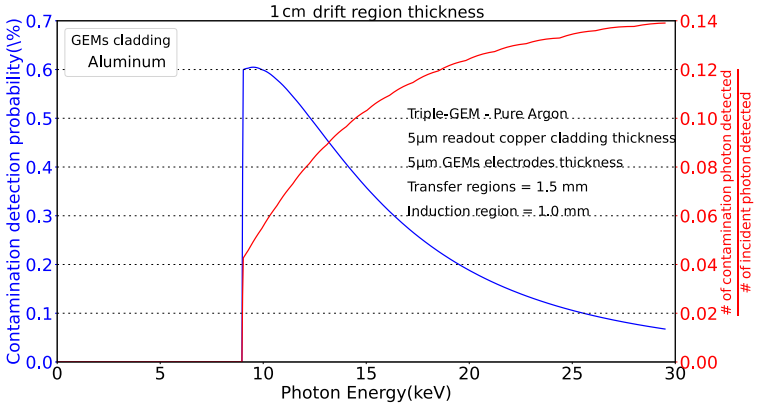


Figure 5.25: Copper fluorescence contamination probability for a triple-GEM detector using aluminum cladding and copper readout.

incident photons is lower in this system. In reality, the etching of aluminum foils may be more difficult and this electrode may show oxidation problems in a shorter time than the copper one. Heavier elements such as silver can also be an alternative. However, the price and the difficulty of deposition may make the manufacture of this type of GEM foil impractical.

Chapter 6

Ion back-flow simulations

As defined in chapter 4, ion back-flow (IBF)describes the migration of ions back to the absorption region, deformation of the electric field that can impair the performance of the detector. Especially in the case of TPCs, the ion back-flow may decrease the spatial resolution and, consequently, the energy resolution. In this chapter we present the results obtained from simulations of the IBF.

6.1 Using a mesh to reduce the IBF

Different groups are prototyping mesh structures to reduce the IBF [76,77]. The mesh being operated under some certain conditions, changes the electric field configuration and consequently the flow of charges. The chosen potential values can be tuned to optimize the passage of electrons and ions. This is a different approach from the gating grid scheme used in the original readout (MWPC based) of ALICE TPC [40], blocking the passage of charge during a certain amount of time, resulting in larger dead time for the detector.

Our group performed some experimental work based on this principle (see [78] for some experimental results). The detector is operated using a mesh between two different GEM structures as figure 6.1 shows. By applying a correct potential to the mesh, it is possible to divide the transfer region into two new regions that work as an extraction region for the first GEM and a drift region for the second GEM. The pitch of the holes of these GEMs was chosen according to the collection and extraction efficiency curves calculated previously [16]. The first GEM of the stack is a standard pitch (GEM-S, 140 µm pitch), which has a collection efficiency for electrons close to 1 in the drift electric field region that we are interest in, while suppressing the flow of ions back to the detector's drift region. The second GEM of the stack is a small pitch (GEM-SP, 90 µm pitch) and was chosen to maximize the collection efficiency of electrons that cross the second transfer zone.

The detector was divided into the different stages of the amplification and transfer processes, as shown in figure 6.1 (right). This is possible because the electric field lines are parallel a few hundred of micrometers away from the electrodes.

The calculation of the IBF is done by determining both the anode and cathode currents. The anode current can be written directly as:

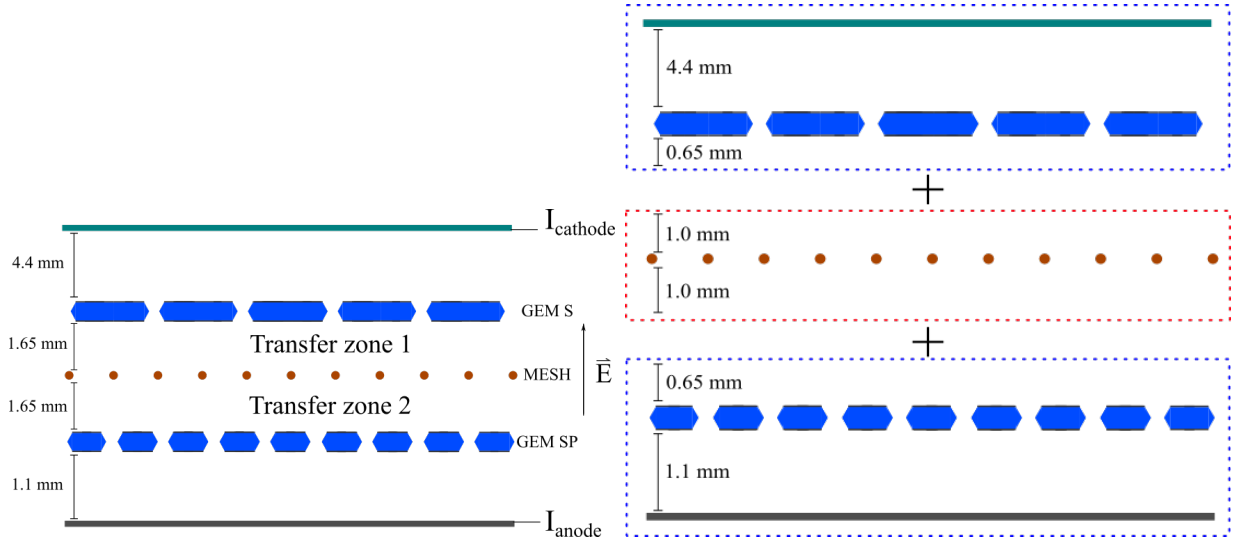


Figure 6.1: Left: Double GEM detector using a mesh to split the transfer zone in two. Right: Scheme of the simulated detector: 3 different unitary cells were made in order to generate a complete output.

$$I_{\text{ano}} = N_{\text{p}} G^{s}_{\text{eff}} T^{-}_{\text{m}} G^{sp}_{\text{eff}}$$

where N_{p} is the primary number of electrons, T^{-}_{m} is the mesh transparency for electrons and G^{s}_{eff} and G^{sp}_{eff} are the effective gain for the GEM-S and GEM-SP foils respectively. Knowing that $G_{\text{eff}} = C^{-} G \chi^{-}$, where G is the absolute gain, we can rewrite the anode current as:

$$I_{\text{ano}} = N_{\text{p}} C^{-}_{\text{s}} G_{\text{s}} \chi^{-}_{\text{s}} T^{-}_{\text{m}} C^{-}_{\text{sp}} G_{\text{sp}} \chi^{-}_{\text{sp}} \tag{6.1}$$

The cathode current will be the sum of 3 different contributions, the primary positive charge ($N^{+}_{0} = N_{\text{p}}$), the ions that come from the first GEM foil (N^{+}_{1}) and the ions that come from the second GEM foil (N^{+}_{2}). The ion contribution from the first GEM can be written as:

$$N^{+}_{1} = N_{\text{p}} C^{-}_{\text{s}} G_{\text{s}} \chi^{+}_{\text{s}}$$

The ion contribution that comes through the mesh, generated at the second GEM(N^{+}_{2}):

$$N^{+}_{2} = N^{+}_{\text{sp}} T^{+}_{\text{s}} T^{+}_{\text{m}} \tag{6.2}$$

where T^{+}_{m} is the mesh transparency to ions and T^{+}_{s} is the standard GEM transparency to ions. Looking at figure 6.2 we can see that the final position of ions depends on the region where they were first created inside the hole, related to the drift of ions following the electric field lines. Since the ion mobility is small, they have enough time to be deflected to the center of the hole and completely follow the electric field lines. In this way, the ion transparency is close

to one for low transfer fields however it starts to drop when the field becomes higher (fig. 6.3). It is not suitable to use the relation $T_s^+ = \chi_s^+ C_s^+$ because when we calculated these quantities using the results from simulating avalanches, they are calculated taking into account that the multiplication happens spread over several points of the hole and not only the central region.

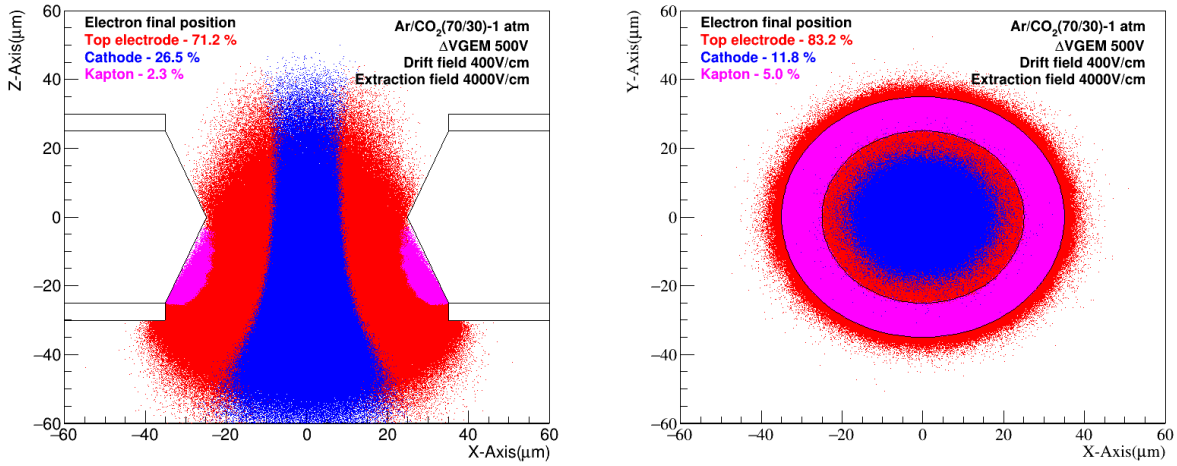


Figure 6.2: Initial position of ions generated in an avalanche. The colors represent the final position of these ions after their drift.

Almost all the ions which are generated or pass through the middle of the hole end their trajectory on the cathode as we may see in figure 6.2. This happens also for the ions that are created in the GEM-SP and drift towards the transfer region. The number of ions that come from the mesh are related with the number of ions generated in the second GEM:

$$N_{sp}^+ = N_s^- T_m^- C_{sp}^- G_{sp} \chi_{sp}^+ \tag{6.3}$$

where N_s^- is the amount of electrons that reach the mesh, coming from the GEM-S. They can be calculated using:

$$N_s^- = N_p C_s^- G_s \chi_s^- \tag{6.4}$$

where T^- is the mesh transparency to electrons. Replacing values from equations 6.4 and 6.3 in equation 6.2, one can obtain:

$$N_2^+ = N_p C_s^- G_s \chi_s^- T_m^- C_{sp}^- G_{sp} \chi_{sp}^+ T_s^+ T_m^+ \tag{6.5}$$

Summing the 3 contributions to the cathode charge, we get:

$$I_{cat} = N_0^+ + N_1^+ + N_2^+ = N_p + N_p C_s^- G_s \chi_s^+ + N_p C_s^- G_s \chi_s^- T_m^- C_{sp}^- G_{sp} \chi_{sp}^+ T_s^+ T_m^+ \tag{6.6}$$

Using the ion back-flow definition:

$$\mathrm{IBF} = \frac{I_{\mathrm{cat}}}{I_{\mathrm{ano}}} = \frac{N_{\mathrm{p}} + N_{\mathrm{p}} C_{\mathrm{s}}^{-} G_{\mathrm{s}} \chi_{\mathrm{s}}^{+} + N_{\mathrm{p}} C_{\mathrm{s}}^{-} G_{\mathrm{s}} \chi_{\mathrm{s}}^{-} T_{\mathrm{m}}^{-} C_{\mathrm{sp}}^{-} G_{\mathrm{sp}} \chi_{\mathrm{sp}}^{+} T_{\mathrm{s}}^{+} T_{\mathrm{m}}^{+}}{N_{\mathrm{p}} G_{\mathrm{s}} C_{\mathrm{s}}^{-} \chi_{\mathrm{s}}^{-} G_{\mathrm{sp}} C_{\mathrm{sp}}^{-} \chi_{\mathrm{sp}}^{-} T_{\mathrm{m}}^{-}}$$

rearranging the expression:

$$\mathrm{IBF} = \frac{1 + C_{\mathrm{s}}^{-} G_{\mathrm{s}} \chi_{\mathrm{s}}^{+} + C_{\mathrm{s}}^{-} G_{\mathrm{s}} \chi_{\mathrm{s}}^{-} T_{\mathrm{m}}^{-} C_{\mathrm{sp}}^{-} G_{\mathrm{sp}} \chi_{\mathrm{sp}}^{+} T_{\mathrm{s}}^{+} T_{\mathrm{m}}^{+}}{G_{\mathrm{s}} C_{\mathrm{s}}^{-} \chi_{\mathrm{s}}^{-} G_{\mathrm{sp}} C_{\mathrm{sp}}^{-} \chi_{\mathrm{sp}}^{-} T_{\mathrm{m}}^{-}} \tag{6.7}$$

Figure 6.3 shows the electron extraction efficiency of the GEM-S foil and electron transparency of the mesh as a function of the induction field (transfer zone 1). Since the drift field was kept constant for different induction fields, the quantities that are somehow a function of the drift field, such as the collection efficiency for electrons and extraction efficiencies for ions are also constant. This will help us to confirm the independence of the electric field above and below the GEM foil. As it was said before, the ion transparency is close to one, although it starts to change for larger induction field values due to charge losses to the bottom electrode. The uncertainties smaller than the markers.

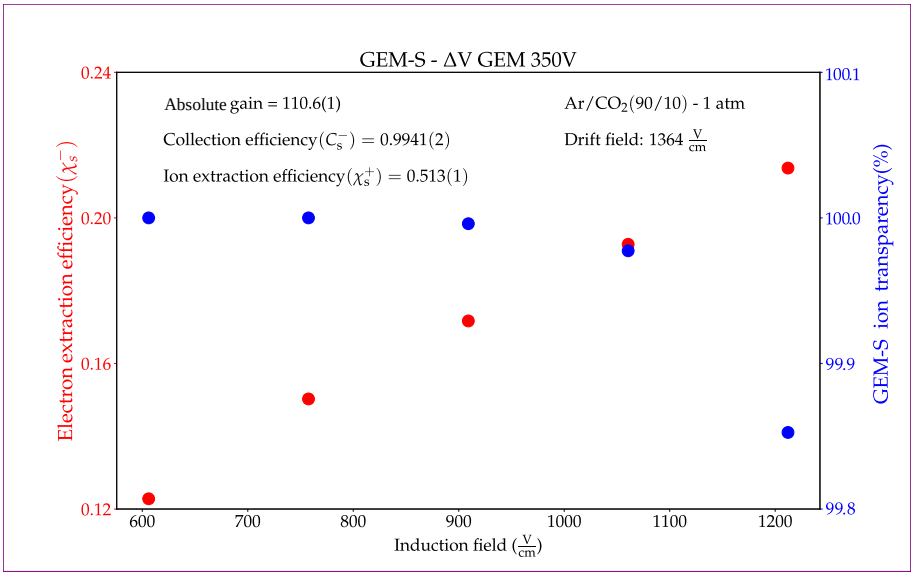


Figure 6.3: Electron extraction efficiency and ion transparency as a function of the induction field.

The mesh transparency for electrons and ions can be seen in figure 6.4 for different fields 1 and 2. It is possible to see that the two behave in the opposite ways related to the field, that is, a high transparency to electrons is linked with a low transparency for ions. For higher electric field in the transfer zone 1 and lower electric field in the transfer zone 2, we are achieving a lower transparency for electrons while we get a higher transparency for ions, already indicating that the mesh is working in the opposite way that was first proposed, that is, increasing the IBF.

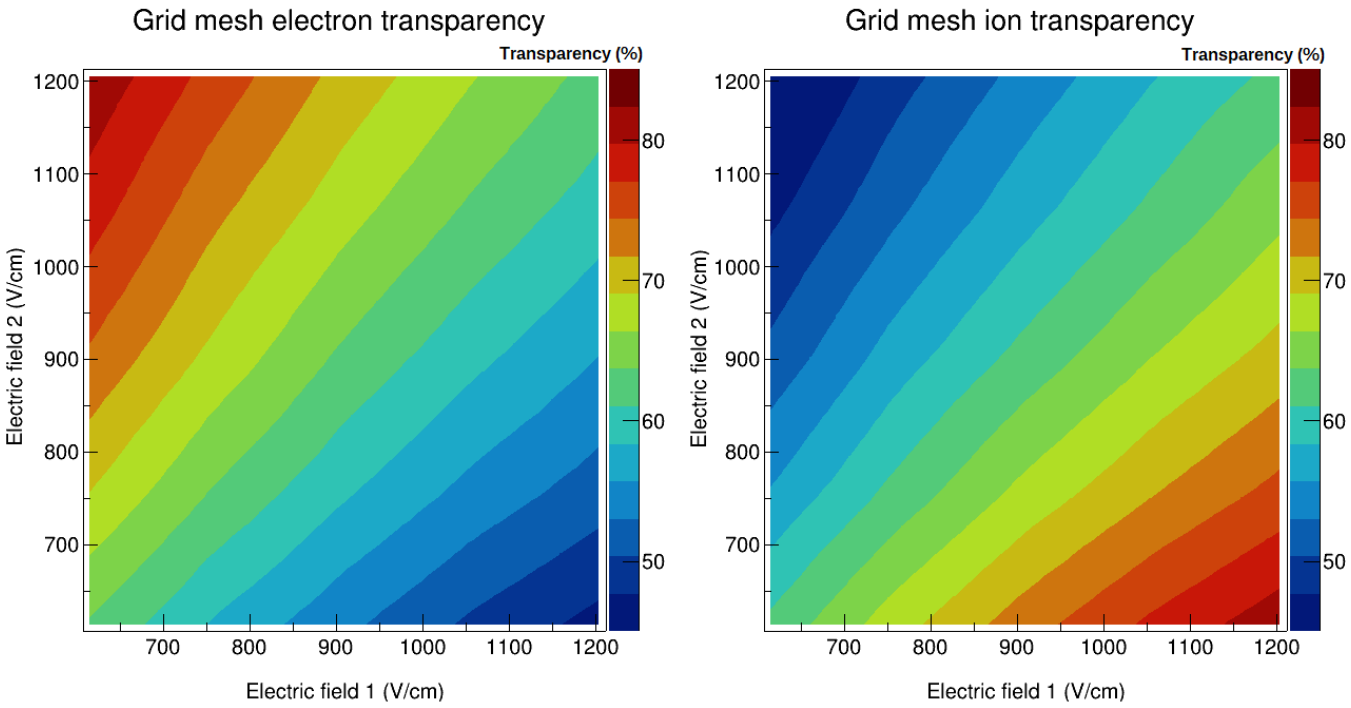


Figure 6.4: Mesh transparency for electrons(left) and ions (right).

The extraction efficiency for ions was calculated for the GEM-SP and can be seen in figure 6.5.

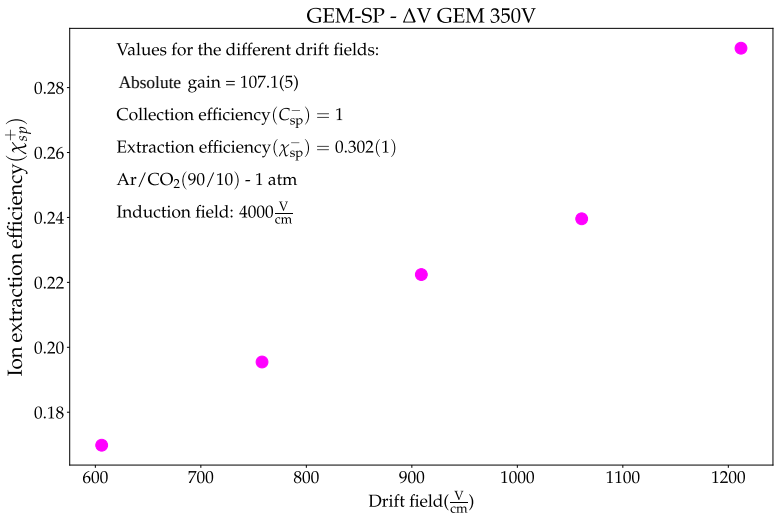


Figure 6.5: Ion extraction efficiency as a function of the drift field.

With all these results it is possible to use equation 6.7 and obtain the value for IBF as a function of transfer fields 1 and 2. Figure 6.6 shows the values obtained.

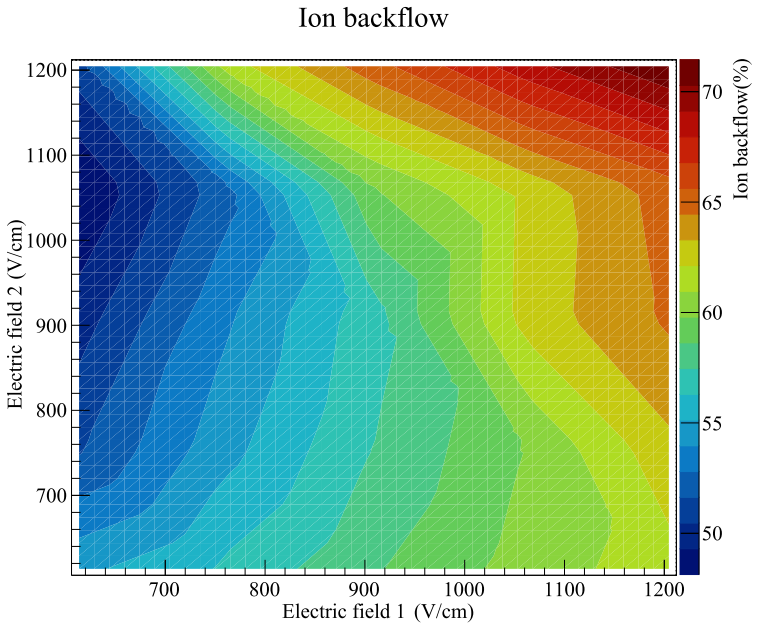


Figure 6.6: Ion back-flow calculated using equation 6.7.

By splitting the transfer region in two, it was possible to maximize the efficiencies on both parts, however for the optimal values for the efficiencies (electric field 1 high and electric field 2 low), the mesh starts to block the flow of electrons while allowing the passage of ions, increasing the ion back-flow.

Chapter 7

Experimental setup

7.1 The detector

The fluorescence imaging system that was built consists of a triple-GEM detector with the layout shown in figure 7.1. The detector operates at atmospheric pressure and the electric fields in the different regions were set to optimize collection and extraction efficiencies.

The detector is mounted on a FR4 PCB board that is also the support for the readout strips and HV connectors. The detector frame, readout plane and GEM foils were all designed and manufactured at CERN. The detector entrance window is a 50 µm thick kapton foil. The frame is sealed with low vapor pressure viton O-rings and the only openings are the inlets and outlets gas tube in which a flow of 6 L/h passes through 4 mm tubes. Digital mass flow controllers from Bronkhorst Hi-Tec [79] are used to control the gas flow and mixture composition (argon and carbon dioxide). Figure 7.2 shows in detail the setup.

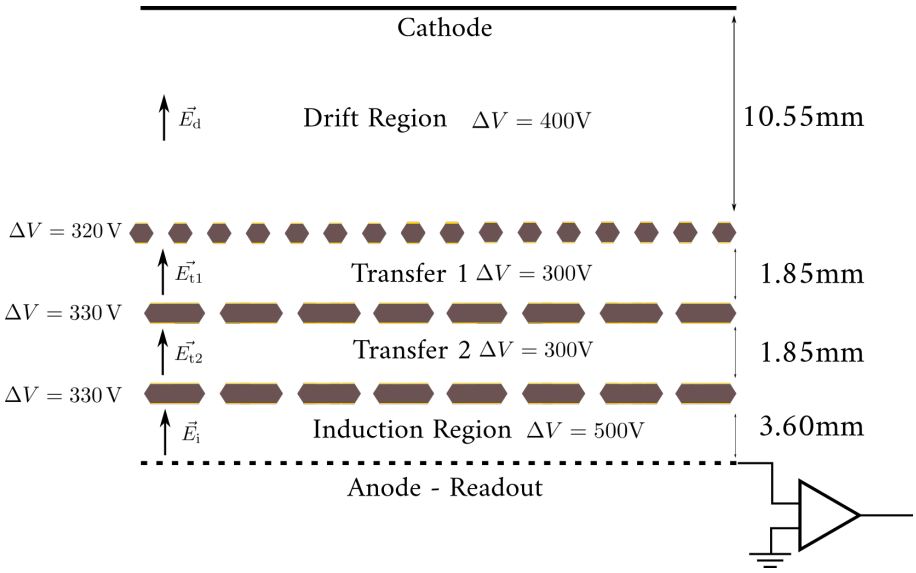


Figure 7.1: Scheme of the detector setup mounted in our laboratory and approximate values of operation for Ar/CO_2 mixtures.

The bias of the GEM foils is done by seven independent high-voltage channels, using standard safety high voltage (SHV) connectors. In the future the idea is to remove most of the SHV connectors after the tuning of the detectors, making the bias distribution using only one HV

channel and to define values for each field by using a voltage divider. This will transform the detector in a more compact structure that can be carried to other sites. As a power supply we are using VME modules from CAEN [80] to distribute the voltage, controlling the system by a Raspberry Pi [81]. The HV control software was developed by HEPIC@IFUSP, providing live information, and safety features (such as ramp-up and ramp-down voltages and a limiting current) to protect the electronics against electrical discharges inside the detector. The coupling between the power supply and the top electrode of the last GEM includes a low pass filter that successfully suppresses frequencies above 60 Hz.

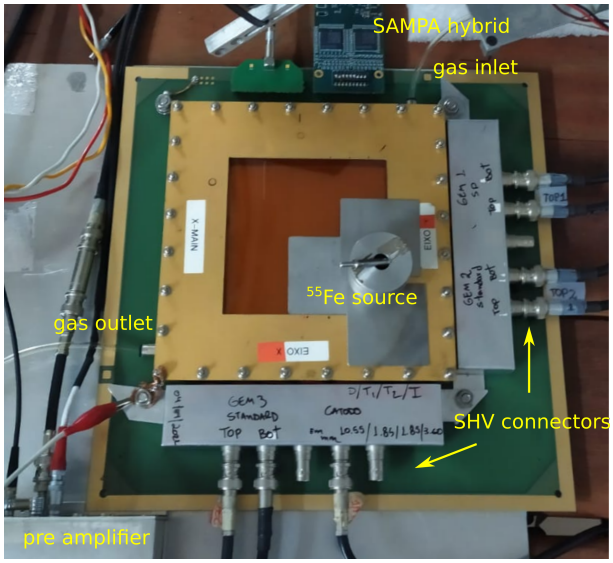


Figure 7.2: Triple-GEM detector mounted for a X-ray transmission acquisition using an ^{55}Fe source.

7.2 The geometry for XRF imaging

X-rays from fluorescence are emitted isotropically, therefore, to make an image, a parallel collimator optics or a pin-hole must be used. The first one works coupled to the detector window, mapping each point of the sample directly on the top of the detector as shown in figure 7.3. The pinhole setup uses the same physical principle of Leonardo Da Vinci's *camera obscura*, where it is possible to project an inverted image of an object in a plane by using a small hole. The advantage of using the parallel collimator optics is the higher flux of photons that are able to reach the detector when compared to the pinhole geometry [82]. The disadvantage of using such a method is that in every image, the shadow of the collimator plate creates an additional artifact that can degrade image resolution and interpretation.

The image made using a pinhole camera is inverted and by varying the distances of the sample and detector to the pinhole, the magnification can be adjusted. In this work we want to test the capability of our imaging system, therefore the distances between the pinhole and sample were set equal (10 cm) and consequently the magnification is equal to one. We can use

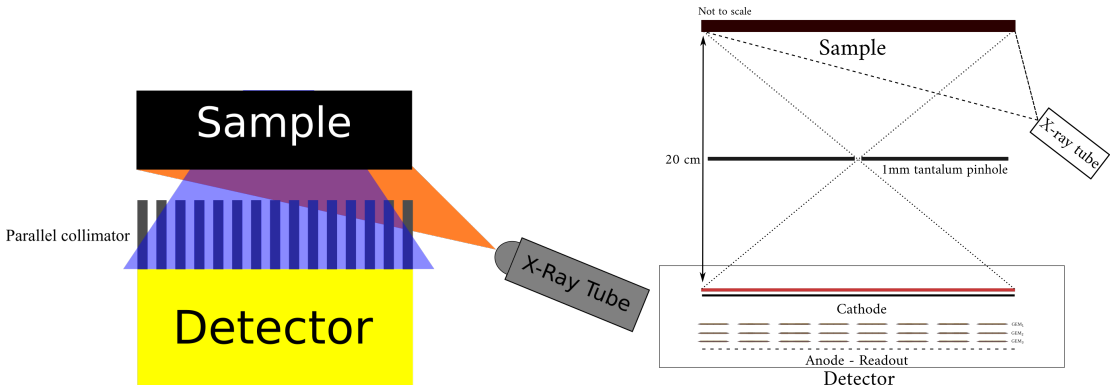


Figure 7.3: Different experimental setups to obtain fluorescence images. Left: Parallel collimator. Right: Pinhole geometry

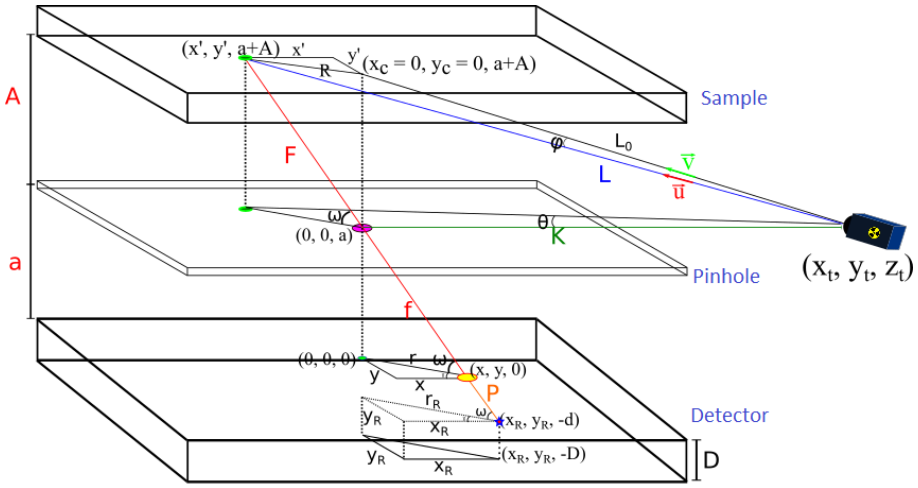


Figure 7.4: Geometric aspects of the detector that can influence the final spectrum.

two different pinholes, both with diameter and thickness of 1 mm: one in stainless steel and one in tantalum.

7.2.1 Geometric response

Since we are using a source that does not irradiate the samples uniformly and the path that is traveled by light changes for different points of the detector, the spectrum intensity in each region will be different and interfere with quantitative analyses. Figure 7.4 helps understanding how the geometry of the imaging setup and the incidence angle of the fluorescence X-rays can influence the event rate measurement across the area of the detector and also affect the final energy spectrum. The origin of the coordinate system is set at the middle of the detector's window, which defines a plane crossed by the before being absorbed. The pinhole is placed at distance a from the window and the sample is in a plane parallel to the detector, at distance A from the pinhole.

The intensity measured by the detector (I_R) at a distance R from its geometric center is given

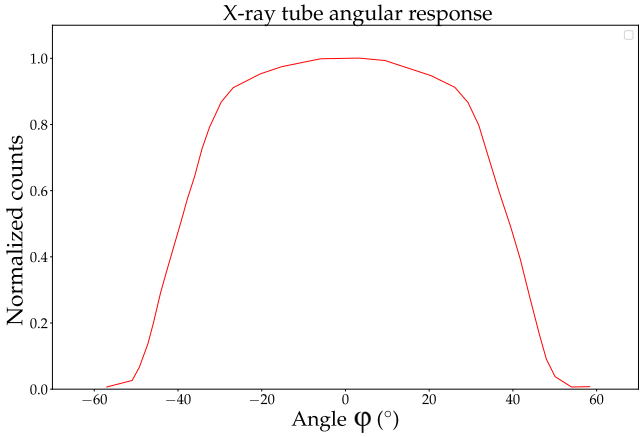


Figure 7.5: Intensity of the radiation emission produced by the X-ray tube as a function of the exiting angle φ. Data adapted from [28]

by a convolution of several factors such as the tube radiation emission ($E_{\mathrm{T}}(\varphi)$), the transmission probability of a photon in air (P_{air}), the transmission through the detector window (P_{win}) and the interaction probability in the gas ($1 - P_{\mathrm{gas}}$), as equation 7.1 shows.

$$I_{\mathrm{R}} = E_{\mathrm{T}}(\varphi)P_{\mathrm{air}}(\lambda)P_{\mathrm{air}}(\lambda')P_{\mathrm{win}}(\lambda')(1 - P_{\mathrm{gas}}(\lambda')) \tag{7.1}$$

The radiation intensity emitted by the X-ray tube is a function of the exiting angle from the tube φ (see figure 7.5). The photon λ is the one emitted by the tube and will travel a distance L. The photon λ' is a fluorescence photon emitted by the sample, traveling a path $F + f$ before it reaches the detector's window. The interaction probability can be calculated using equation 2.1, applying the attenuation coefficients obtained from reference [58].

The path L, traveled by photon λ, can be obtained using the tube's coordinates (x_t, y_t, z_t) and the interaction point on the sample $(x', y', A + a)$. To calculate the emission angle, we also need the coordinate where the tube is aiming at $(x_c, y_c, A + a)$, that is, the point in the sample where $\varphi = 0$. To get the intensity of X-rays arriving at $(x', y', A + a)$, we need to calculate the angle φ whereby, the following equation holds:

$$\cos\varphi = \frac{\langle \vec{u}, \vec{v} \rangle}{|\vec{u}| \cdot |\vec{v}|},$$

and consequently

$$\varphi = \arccos\left(\frac{(x' - x_t)(x_c - x_t) + (y' - y_t)(y_c - y_t) + ((A + a) - z_t)^2}{\sqrt{(x' - x_t)^2 + (y' - y_t)^2 + ((A + a) - z_t)^2}\sqrt{(x_c - x_t)^2 + (y_c - y_t)^2 + (A + a) - z_t)^2}}\right).$$

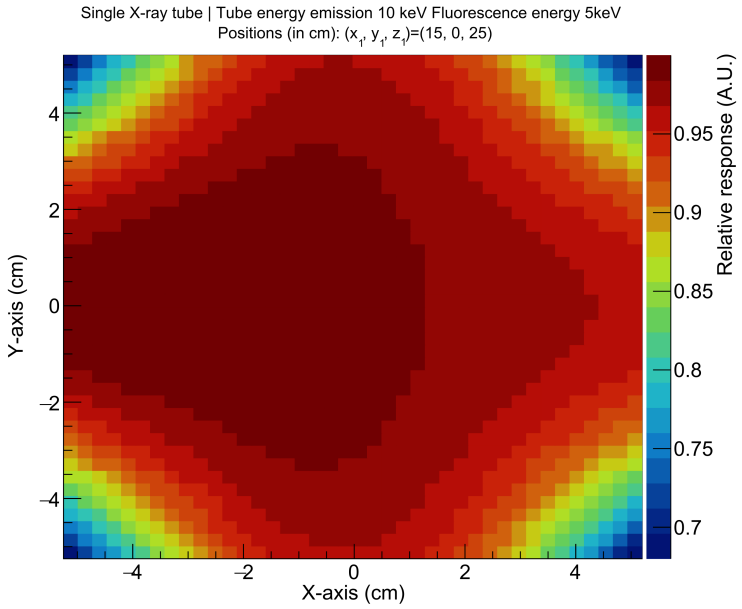


Figure 7.6: Normalized intensity measured by the detector for a 5 keV fluorescence photon. Sample irradiated with one X-ray tube placed on the coordinates (x_t=15 cm, y_t=0, z_t=25 cm).

To calculate the path $F + f$, traveled by the photon λ', we need to know where it entered the detector. We may then use the following relations:

$$r = \sqrt{x^2 + y^2}, \qquad f = \sqrt{r^2 + a^2}, \qquad F = \frac{Af}{a}.$$

After entering the detector, the photon is converted into electrons at some point between 0 and D. In our example we are assuming the coordinate $(x_r, y_r, -d)$, and the electron cloud will hit the readout system at the point $(x_r, y_r, -D)$. These coordinates can be obtained using:

$$x = \frac{a}{(a+d)} x_r, \qquad y = \frac{a}{(a+d)} y_r.$$

The position of the sample is uniquely defined and given by:

$$x' = -x\frac{F}{f}, \qquad y' = -y\frac{F}{f}.$$

Since the photon can interact at any height inside the gaseous volume, the probability needs to be integrated over the thickness d.

Figure 7.6 shows the normalized response of the detector as a function of geometric aspects, using equation 7.4 and the derivations discussed. In this example the X-ray tube was placed at coordinates (15, 0, 25) cm, the distances A=a=20 cm and the detector drift region set to 1 cm. The tube was aiming at the center of the sample. The simulated tube emitted a mono energetic 10 keV radiation beam. The fluorescence was also considered monochromatic, emitting 5 keV

photons. It is possible to see a large difference in the relative intensity measured by the detector due to geometric aspects. This will lead to discrepancies in the intensity of the energy spectrum if one measures the same uniform sample using different areas of the detector. One alternative to mitigate this situation is to use two X-ray sources to irradiate a sample.

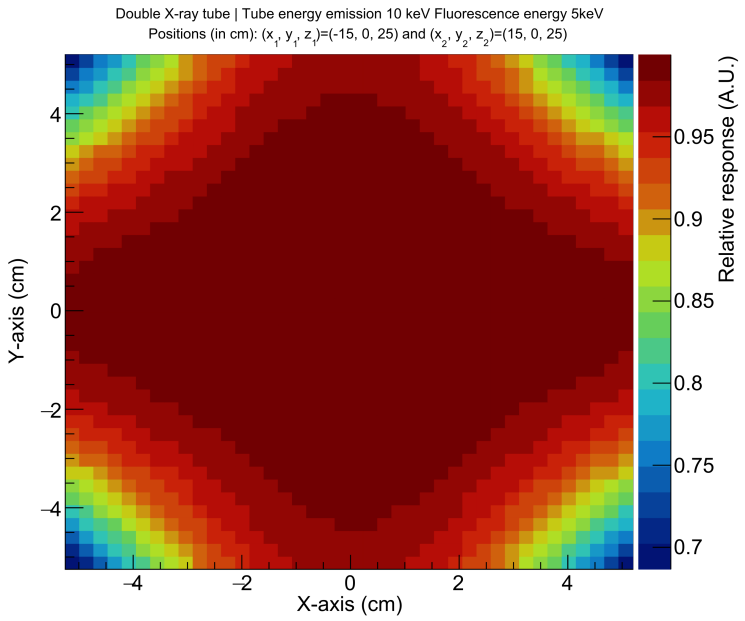


Figure 7.7: Normalized intensity measured by the detector for a 5 keV fluorescence photon. Sample irradiated with two X-ray tubes one placed at (15, 0, 15) cm and the other at (-15, 0, 15) cm.

Figure 7.7 shows an improved uniformity of the irradiation when two X-ray tubes are used, one at coordinates (15,0,15) cm and the other at (-15,0,15) cm. The relative intensity deviation was reduced and the illumination in the central area of the sample, and consequently in the detector, is more uniform. Eventually, post-processing data analysis could also be done to correct the intensity of the energy spectrum for a specific region of the detector.

To validate the simulation results with experimental data, when the first detector was mounted, a flat titanium plate (K_α fluorescence at 4.51 keV) was irradiated using a 1 mm diameter stainless steel pinhole and the data was collected with a triple-GEM detector. The results were compared with the values obtained by the simulation. For this experiment the X-ray tube was placed at coordinates (0, 7.5, 21) cm. The triple-GEM used for this experiment had a drift region thickness of 0.80 cm and details are described in [17]. Figure 7.8 shows the simulated curve, for the same X-ray tube position, on the left and we can see the events obtained using the triple-GEM based detector on the right.

The simulation partly describes the measured profile, however with clear discrepancies. The first one is the uncertainties in the measurements of the X-ray tube position in the laboratory. Since we do not have a fixed setup or an optical bench that allow to properly align the setup, this could cause few differences on the profile obtained. Also, here we calculated a single emission

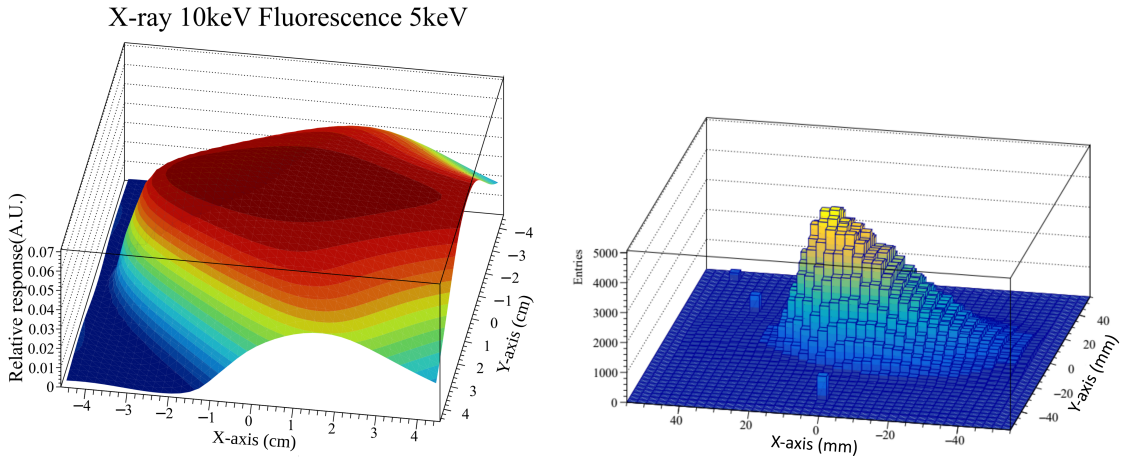


Figure 7.8: Left: Simulation of the image/geometric response produced by a plate with the emission of 5 keV after irradiation with a simulated X-ray source. Right: Experimental result for a Ti plate with similar arrangement.

line of 10 keV which is certainly not equal to the X-ray tube emission spectrum (Mini-X with Ag target). To obtain a more detailed and reliable simulation there is the need to take into account the emission curve of the X-ray tube and also the elements present in the sample needs to be identified to obtain both information about the energy of fluorescence and also the fluorescence yield. The self absorption of the material can also be considered.

7.3 The scalable readout system

Developed at CERN, the SRS or Scalable Readout System [19] is a powerful electronics framework created as a common back-end electronics to support different types of detectors and their front end electronics. One of the most used setups for gaseous detectors applications at the Gaseous Detector Development laboratory at CERN and by members of the RD51 collaboration is to use the APV25, a CMOS (Complementary Metal Oxide Semiconductor) created to be used at the CMS tracker [83], as a multi-channel readout chip. Using 4 APV25 hybrids, it is possible to cover all the 512 electronic channels of a standard gaseous detector readout, allowing to read each anode strip independently.

As 'scalable' in the name SRS suggests, it can be used for table top experiments dealing with a few electronic channels but also in systems with tens of thousands of them. In the case of XRF fluorescence imaging, the advantage to read each anode strip independently is the improvement of spatial resolution when compared to resistive charge division [16]. The APV25 can record the full waveform of the signal, or operate in zero suppression mode, transmitting only data above a threshold. Using this feature it is possible to acquire data at rates above 1 kHz. To acquire data at higher counting rates (up to few MHz) different chips such as the

VMM [84] and the SAMPA chip [85] must be used.

7.4 The SAMPA chip

The SAMPA chip [18, 85] is an ASIC (Application Specific Integrated Circuit) developed at the Integrated Systems Laboratory (LSI) of the USP Polytechnic School (POLI) to serve the TPC and the Muon Chambers (MCH) of the ALICE experiment, operating at CERN. It was designed and fabricated in 130 nm TSMC technology. Each chip has 32 channels and they are equipped with a Charge Sensitive Amplifier (CSA), followed by shapers and a 10-bit Analog-to-Digital Converter (ADC) with sampling frequency of 10 MSps and the capability to run at up to 20 MSps depending on the configuration. A simplified block diagram of SAMPA can be seen in figure 7.9.

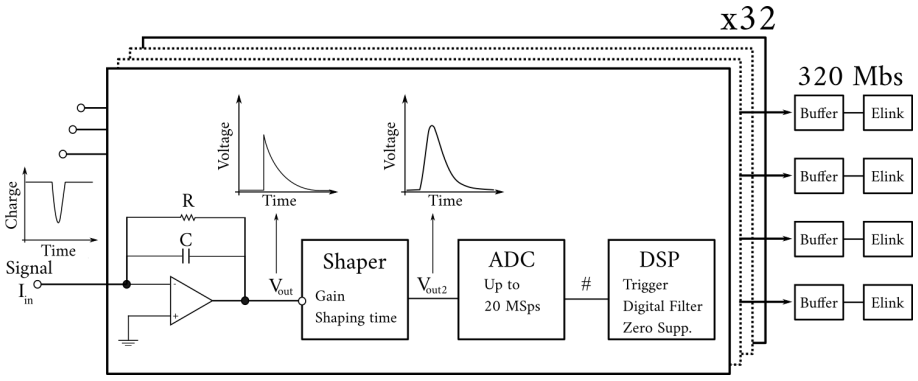


Figure 7.9: Block diagram of SAMPA showing its main processing blocks.

The SAMPA front-end is composed of a negative and positive CSA, a Pole-Zero cancellation circuit and a sequence of filters. The charge signal is converted to a voltage pulse and transmitted to a shaper. Different shaping times and gains are available depending on the version of SAMPA, table 7.1 shows in detail the configuration possibilities of SAMPA, designed for two different applications, the ALICE's TPC and the MCH.

7.4.1 The SAMPA hybrid

To operate a detector with hundreds of electronic channels, several SAMPA chips need to be mounted in a specific board (which is connected to the detector). One of the functions of this board is to provide the necessary power for the operation of the chips (20 mW/channel). A hybrid board, which fulfills these requirements, was designed by engineers at POLI. An image of the fabricated prototype can be seen in figure 7.10. Each strip or pad of the detector is connected through a specific connector to one of the SAMPA's channels. Since the standard readout produced by the RD51 collaboration uses the 140 pin Hirose connectors, the hybrid

	TPC-v4	**MCH-v4**	**TPC-v5**
Polarity	Negative	Positive	Negative
Sensor capacitance	12-25 pF	40-80 pF	12-25 pF
Gain/sensivity	20/30 mV/fC	4mV/fC	20/30 mV/fC
Equivalent Noise Charge	< 580 e$^-$ (18.5 pF)	< 950 e$^-$ (40 pF) < 1600 e$^-$ (80 pF)	< 580 e$^-$ (18.5 pF)
Shaping time	160 ns	300 ns	160/300 ns
Baseline return	< 500 ns	< 550 ns	< 500 ns
Sampling rate	10 (20) MS/s	10 MS/s	20 MS/s

Table 7.1: SAMPA'S configuration.

board was built using 4 SAMPA chips and it can read up to 128 electronic channels at once operating at 300 MHz main clock. A single DisplayPort cable is used to connect the hybrid to the adapter card, connected to the Front-End Card (FEC) of the SRS. The hybrid has external switches to change between gain configurations, shaping time, sampling rate and polarities. The physical dimensions of the hybrid are compatible with the standard readout plane developed by the RD51 collaboration.

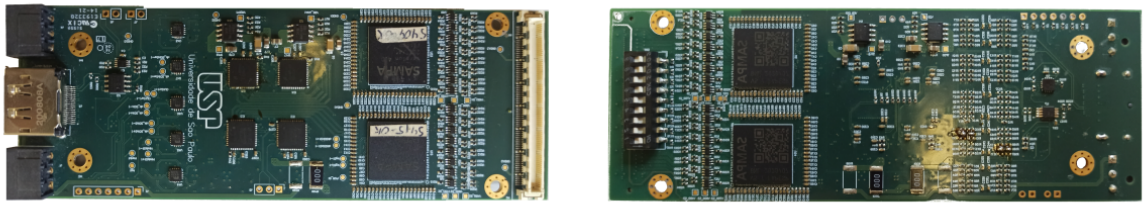


Figure 7.10: Photograph of both sides of the 4-SAMPA hybrid board.

7.4.2 The SampaSRS software

A software package was developed to control and operate the SAMPA-SRS data acquisition. The different steps of the framework were written in C++, using TCPDUMP and LIBPCAP libraries for network traffic capture. CERN's ROOT libraries [86] were also implemented for data storage. The reconstruction analysis steps are the following:

- **sampa_control:** request/reply protocol communication between the computer and the SAMPAs to configure the acquisition (start/stop, internal/external trigger, waveform length, latency, zero suppression threshold);
- **sampa_acquisition/sampa_gui:** a tool that captures the packages from the network. A graphic user interface processes and decodes small amounts of data to create few his-

tograms for monitoring and online data quality control (energy spectrum, channel of the strip with the maximum energy value and its waveform);

- **sampa_decoder:** transforms the raw data produced by SAMPA and coded by the FPGA host in the SRS FEC board to be transmitted via UDP protocol to the computer and converts it into root tree files. The event built contains information of time, channel and the complete waveform produced after a trigger;
- **create_pedestal:** processes and produces a pedestal file containing information of the baseline levels and noise for each channel. Can be used for offline zero suppression or as input for the online zero suppression of SAMPA (work in progress);
- **clustering:** using a pedestal file, builds the clusters using an algorithm that is explained in detail ahead. The new file contains information regarding the position of the center of mass of the cluster, energy and size (number of strips).

Details regarding the acquisition, such as the total number of events, trigger rate, percentage of valid events (SAMPA's validation bits and package integrity), network usage, writing to disk speed and load are also shown in real time. Figure 7.11 shows the *sampa_gui*'s monitoring window.

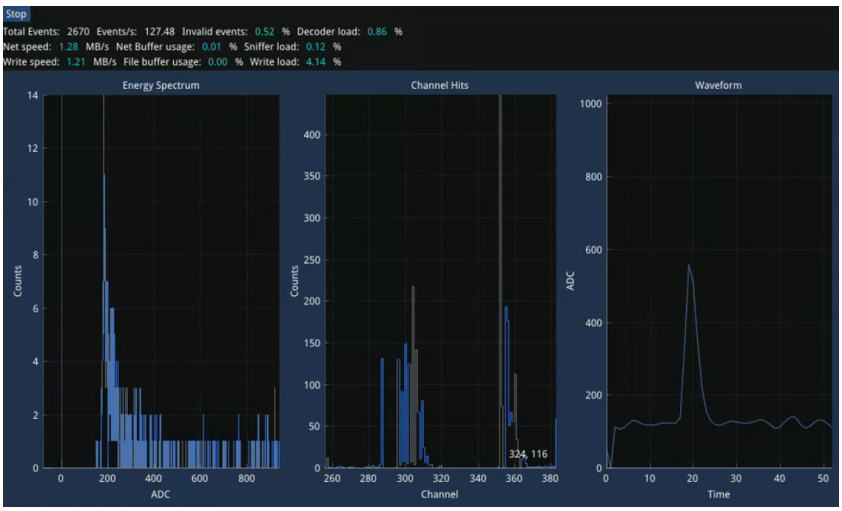


Figure 7.11: SampaGUI window (from left to right): Energy spectrum, channel of the strip with the maximum energy value and waveform of the channel with maximum energy

Figure 7.12 shows a normal pedestal. It is still possible to see several malfunctioning channels that were discarded in post processing. The first prototype had communication issues that were related with the connections between the SAMPA adapter board and the SRS FEC, causing data reception to be impaired. Figure 7.13 gives an example of how these issues are reflected in the data. It is possible to see several channels that show zero noise because they were locked to a constant ADC value, making it impossible to use them.

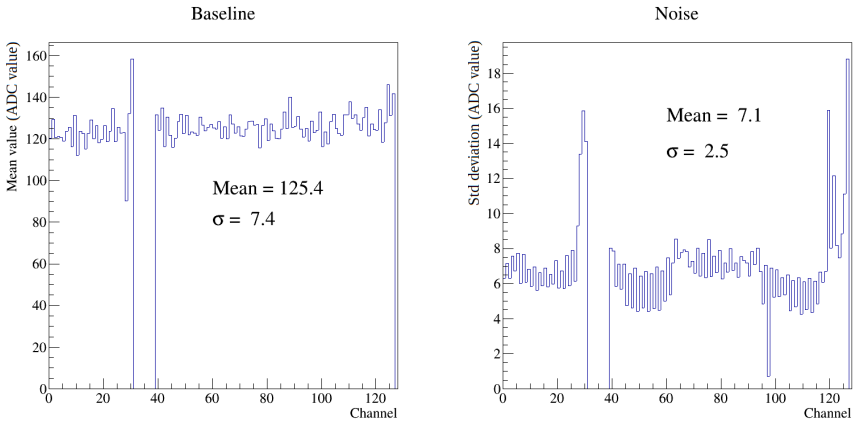


Figure 7.12: Good SAMPA pedestal sample. The missing channels are malfunctioning and are not sending data. These plots allow their immediate identification, as well as the noisiest channels.

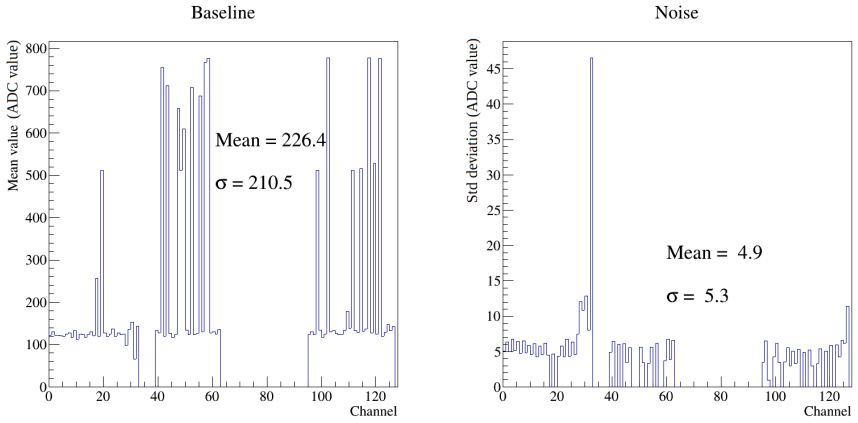


Figure 7.13: Bad SAMPA pedestal sample. Many channels are missing or lacking reliable information (constant ADC reading - leading to a false zero noise value) due to communication failure between the boards.

Calculating the noise for each strip (standard deviation of the baseline) using a large number of samples (10^4 words) it is possible to see a clear split of the data and two different expected values for noise. Looking in detail it is noticeable that the channels with even number have a different noise mean when compared to channels with odd number, and this is due to the difference in the length of the strip that goes to the connector, changing the capacitive coupling.

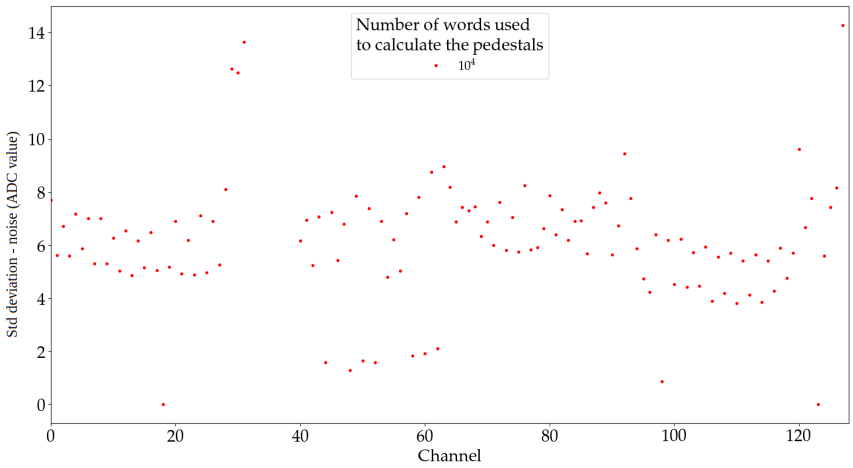


Figure 7.14: Noise calculated for each channel using 10^4 samples. It is possible to see an alternation in the noise values depending on the position in the connector where the channels are located.

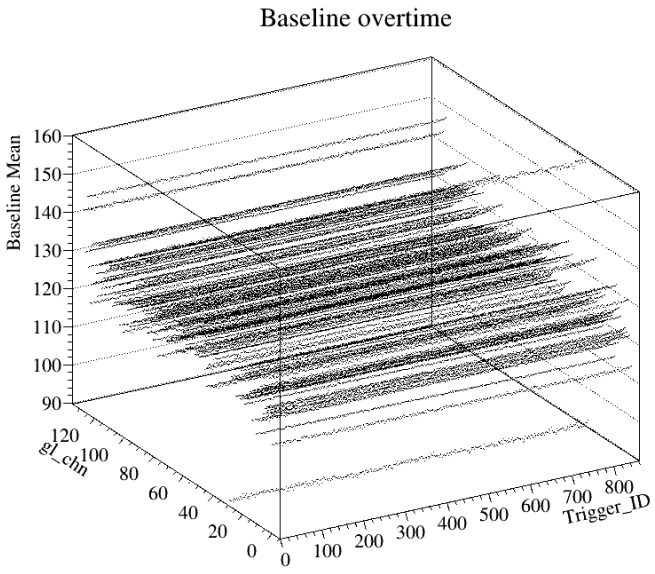


Figure 7.15: Baseline mean for each channel through time.

To evaluate the common-mode signal (CM), that is, a group behavior related with ground level shifting which can impair the reconstruction of events, especially for ADC reading close to the threshold, we evaluate the baseline mean for each SAMPA channel throughout time. Each point in figure 7.15 represents the baseline mean calculated using 1000 ADC samples for each channel. This test was made using the FEC's internal trigger. The trigger was set to 33 Hz and approximately 850 events were acquired (representing almost 26 seconds). By looking at this measurement it is not clear that the system is suffering from event-by-event pedestal fluctuation. A more detailed analysis, shown in fig. 7.16, was done taking into consideration a

smaller time scale to check if a slight change in some parameter of operation such as the high voltage applied to the GEM foils could change the behavior of the system. The common-mode signal can be estimated by looking at the average shift of the channels from the baseline at each time bin. The common-mode signal is defined as:

$$C(t) = \frac{\sum_{i=0}^{N} B_i(t) - \overline{B_i}}{N} \tag{7.2}$$

where $B_i(t)$ is the ADC reading of channel i at the time t, $\overline{B_i}$ is the baseline value and N is the number of channels.

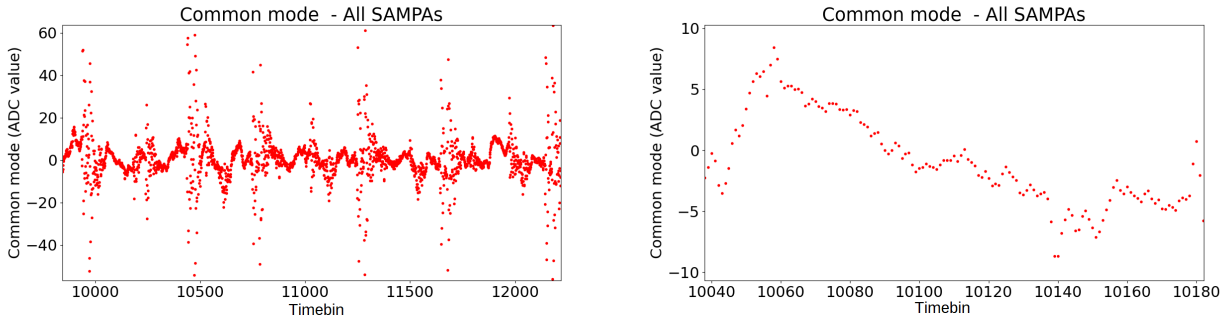


Figure 7.16: Common-mode signal calculated for each time bin during a pedestal run.

It is expected that the average across strips is zero if no common-mode signal is present. However, it is clear that group behavior can be observed in the SAMPA channels, for example in figure 7.16 at the time bin close to 10500. This means that all channels have a simultaneous baseline shifting of almost 60 ADC counts. As mentioned before, several factors may contribute to that, such as a high voltage power supply jitter, a grounding problem or even small sparks in the detector. An offline common-mode correction can be made using the information from all the channels. The common-mode signal can be calculated for each time bin (using the ADC value from all channels) and subtracted from the signal of each channel. With that, a new noise level can be calculated and therefore a new threshold for the events.

Figure 7.17 shows the noise before and after removing the CM shift in each time bin for the pedestal calculation. A reduction of half of the original value was achieved and this can improve the performance of the detector. To apply such correction in data containing signals is not as trivial as it is done for the pedestal run, requiring an additional scan through the data, first to determine which channels contain a signal and to remove those from the CM calculation. After that, the CM is calculated for each time bin and each channel without a signal applying the correction to all channels.

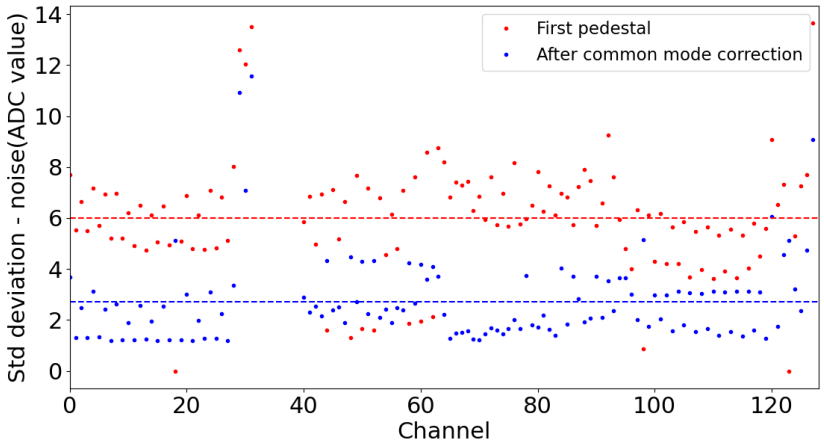


Figure 7.17: Noise calculated for each strip before and after using the common-mode correction. The dashed lines represent the mean of each distribution.

7.4.3 Clustering algorithm for event reconstruction

When an ionization happens inside the active volume of the detector the charge is deposited over several readout strips. Also, depending on the gas mixture used and energy of the primary photon, more than one cluster can be generated in the same event, for instance, when the argon fluorescence photon interacts far from the primary interaction point. A clustering algorithm uses the baselines and noise values to search for clusters of signals within an event and use this information to apply the center of mass algorithm. The clustering algorithm starts to compose a cluster when a strip with a signal above the threshold (T_1) is found. The neighboring strips with signals above the threshold are added to that cluster until two consecutive strips are found below the threshold level. When this happens, the cluster is closed, the total energy is summed and the center of mass is applied to calculate the reconstructed position. Figure 7.18 exemplifies some of the situations that can happen during the creation of clusters. In real data each strip has its own threshold depending on its noise and baseline.

The clustering algorithm developed for this work only takes into consideration one dimension to reconstruct the clusters. In a 2D readout the same clustering is applied independently to the two directions, and followed by a cluster-matching algorithm. After applying the clustering process to the data produced by the SampaSRS software, a ROOT tree is filled with information of the cluster multiplicity, the location of each cluster in space, the total energy and the strip multiplicity in each cluster.

7.4.4 Data production and zero suppression

The SAMPA chip can be operated with a user defined sampling rate of up to 20 MS/s. Due to one of the clocks of the front-end card of the SRS, this rate was limited to a value of

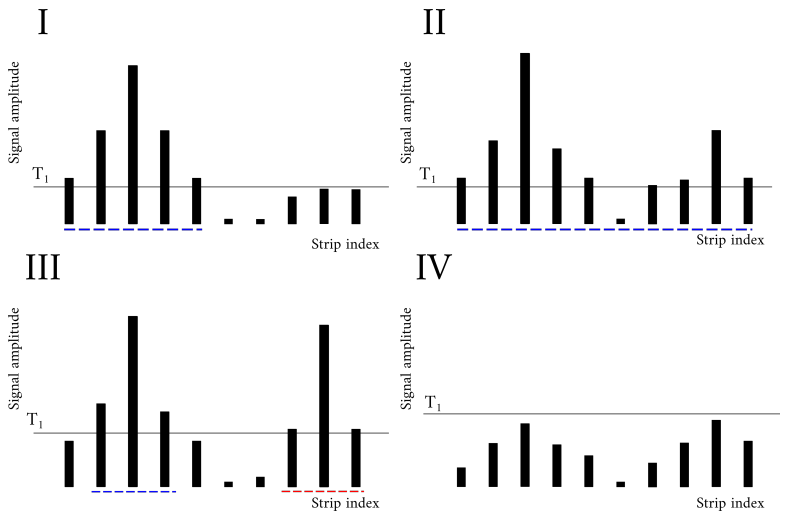


Figure 7.18: Different examples of the result of the clustering algorithm. The valid clusters are marked with the blue and red dashed line in the x-axis. I) Valid cluster on the left. II) Valid single cluster. III) Two clusters (above T_1). IV) No valid cluster reconstructed.

18.5 MS/s. If we calculate the amount of data that can be produced we reach a value of 5920 Mbit/s or 0.75 GB/s (18.5 MS/s x 32 channels x 10 bit). To transmit this data each SAMPA is equipped with 11 e-links of 320 Mbit/s, however, for the SRS integration only four are being used. Although all this data can be produced by only one SAMPA chip, there is a limitation to the data that can be transmitted by the FEC to the acquisition computer and the maximum value that can be reached is 1 Gbit/s. The data transmitted can be limited by selecting a specific number of samples that each channel will send after a trigger. To emulate the data produced by the detector, different trigger rates were injected in the system. Figure 7.19 shows the measured data traffic produced by one single SAMPA hybrid as a function of the detector trigger frequency and the number of ADC sampling per channel per trigger.

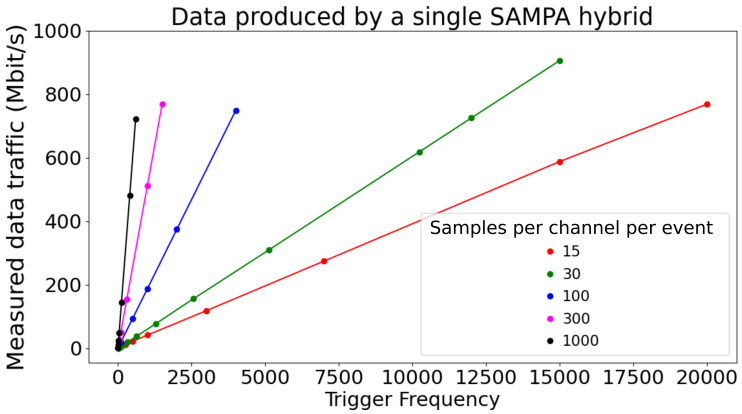


Figure 7.19: Data transmitted by the SRS FEC according to the trigger rate in the detector (only one hybrid - 4 SAMPAs - is being used) and limit line.

Looking at the red curve (15 samples per trigger per channel) it was possible to achieve

value above 20 kHz without using the whole bandwidth of the network. This calculation was made with no zero suppression, that is, channels that do not have a signal are still going to send their ADC readings.

One thing that can be done to improve even further the event rate that can be read by SAMPA is to use the online zero suppression. A well defined charge pulse was injected in one of the channels and a threshold value was defined. Only readings that are above this threshold were recorded. Figure 7.20 shows an example of this feature for one specific channel of SAMPA.

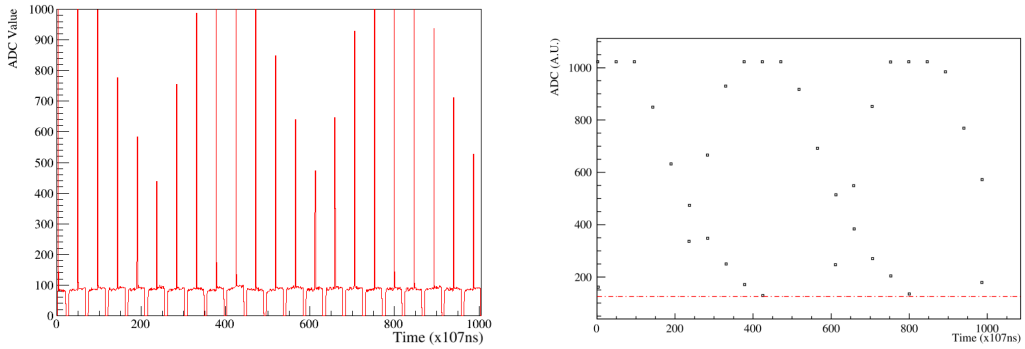


Figure 7.20: Comparison between what is sent before and after turning the zero suppression feature. Left: Pulse injecting at a rate of 200 kHz – Period T = 5 µs. Right: Same pulse in zero suppression mode (threshold set to 125 ADC units).

A typical pulse produced by the SAMPA chip has a duration of a few hundreds of nanoseconds. Estimating that after the photon absorption the charge is deposited across a few strips it is possible to estimate the maximum counting rate that can be achieved with this system in zero suppression mode. Disregarding spurious noise that eventually can go above the threshold, if the charge is deposited in only 5 channels, with a peak duration of 10 ADC samples per channel, a 1 Hz rate of events would produce 50 words/s, therefore, the maximum value of the bandwidth, which is 1000 Mbit/s will be reached at an event rate as high as 2 MHz.

Chapter 8

Experimental results

8.1 Detector characterization

Different ways to test the performance of an imaging system were explained in chapter 4. All these methods were tested in a previous work [16] and the results obtained were equivalent. Therefore, to evaluate the resolving power of the systems mounted during this work we choose the MTF method. To evaluate the resolving power we worked in transmission mode and we calculated the position resolution using the specific lead pattern shown in fig. 8.1 (standard test type 38 - 100 µm thick Pb).

8.1.1 The SRS with APV25

Measurements with the ASIC APV25 installed in the SRS were done using a 2D readout strip detector. This could provide an interesting comparison with the measurements made using the SAMPA chip. The first measurements with APV25 were made by placing the X-ray tube (Amptek mini-X with Ag target) around 25 cm above the detector's window. With this setup we were able to achieve a counting rate of about 1.2 kHz in transmission mode, limited only by the APV25 capability to process data. The X-ray tube current was set to 5 µA and the acceleration potential to 10 kV. To reduce the intensity of photons, a 250 µm thick aluminum filter was added to the tube's exit window, filtering lower energies and reducing the counting rate to the desired value. Figure 8.1 shows the resolution pattern picture and the reconstructed image.

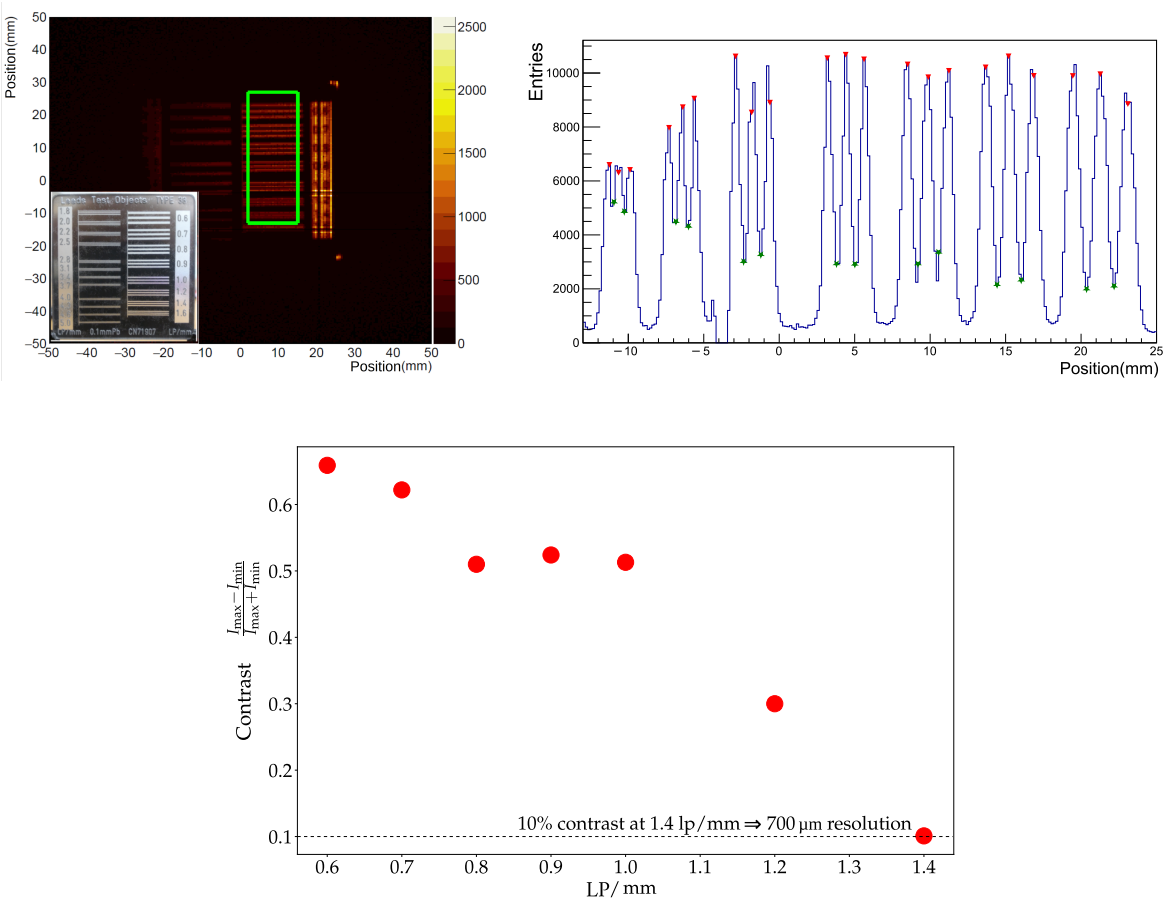


Figure 8.1: Top: Lead mask and X-ray transmission image using the SRS with APV25 and profile of the data selected from the inside of the green rectangle. Bottom: Contrast calculated for each line pair set.

To obtain the position resolution of the imaging system, the Modulation Transfer Function (MTF) was used. As it was explained, this method measures the contrast response of the system to different spatial frequencies [52]. The contrast was obtained using the Michelson definition [51], as seen in equation 4.15. The absolute value of contrast decreases for higher spatial frequencies (smaller objects) and the final resolving power of the detector is assumed to be the MTF at 10 % of contrast [50]. The contrast was calculated from the image profile and is shown in figure 8.1. Assuming that the position resolution is equivalent to the inverse of the spatial frequency at 10 %, these preliminary measurements provided a value of resolution power of less than 700 µm.

To create fluorescence images a different setup is needed as illustrated in figure 7.3 and shown in the photograph of fig. 8.2. To generate images using a pinhole geometry, first one needs to change the position of the X-ray tube and to add a lead shielding above the detector window to prevent the passage of X-rays that do not come from the pinhole. The sample was placed 10 cm away from the pinhole and the detector was kept at this same distance to keep the magnification equal to 1. In our setup the average counting rate obtained for this experiment

(using a 1 mm tantalum pinhole and the mini-X X-ray tube [28] at 20 keV and 150 µA) was approximately 350 Hz, limited only by geometric constraints and the output current of the X-ray tube. The screw-on brass cover was kept at the X-ray tube output and no collimator was attached to it. One of the first fluorescence images to test the system's capability is from a titanium plate with several rectangular pieces of copper glued on it. Figure 8.2 shows the picture of the plate and the reconstructed image using the SRS. The color scale in the image was developed in previous works [17] and shows different energies as different colors and the intensity in each pixel as a different level of white, like in a false color X-ray image.

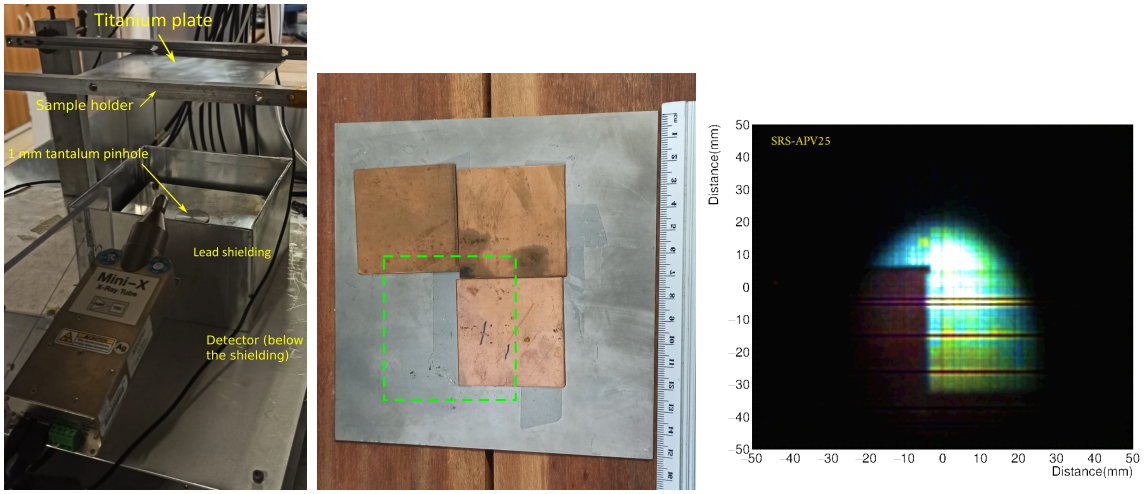


Figure 8.2: Left: Pinhole geometry setup mounted for X-ray fluorescence imaging measurements. Middle: Photography of the titanium and copper plates used to perform the fluorescence image described in the text. The green dashed line shows the region irradiated. Right: Image reconstructed using the SRS system and APV25.

As shown in chapter 5, our detector has its maximum efficiency for energies close to 8 keV, which is approximately the same energy as the copper K_α fluorescence. When we choose to look at a specific region of the image, we can reconstruct the energy spectrum for that part and use it to identify the presence of different elements. Figure 8.3 shows the energy spectrum for two different regions. At first, we can clearly notice in the image that the fluorescence intensity is different for the two different materials.

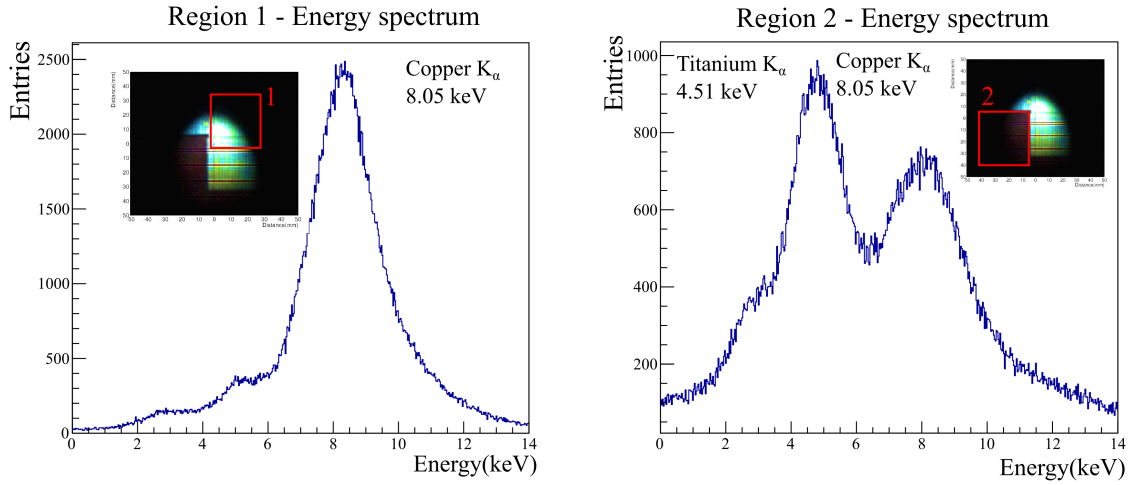


Figure 8.3: Energy spectra from different parts of the titanium and copper plate. Left: Energy spectrum for region 1, where there is only the presence of copper. Right: Energy spectrum for region 2. We can see the presence of two 2 different elements.

A detector with a large area will have different gain over its active area. This gain variation is linked with several factors such as non-uniform spacing between the GEM foils, the cathode and the anode. Also, one of the foils may be slightly bent, changing the electric field configuration and consequently the collection and extraction efficiencies of the detector. So before analyzing the energy spectrum and to calculate the resolution of the detector, a gain equalization should be made. By mapping the gain distribution across all the active region of the detector it is possible to create a correction factor and to obtain a uniform gain across the complete area of our system. The measurement was made placing an ^{55}Fe source 10 cm above the detector and fully irradiating the detector window for several hours. The corrections to the relative amplitude of the peak in different regions were then applied. For this, the detector was divided in 32 sectors for each dimension, obtaining a total of 1024 regions, and for each one of them, the peak position of the K_α fluorescence of ^{55}Fe was measured. Figure 8.4 shows the relative peak position divided by the mean position across the whole detector window. Figure 8.4 shows the gain variation and differences in the energy spectrum measured before and after applying the correction to our detector. In this setup these differences are not very significant, however, it was observed in other detectors [17] that these corrections are a requirement to achieve a fair energy resolution. It is possible to see that the distribution after gain normalization becomes thinner and higher in the peak region and the valley between the main peak and the escape peak becomes deeper, indicating a better resolving capability. Since it was not observed a change in the gain map over the time of this work, we assume that the mapping is something intrinsic to the system, related with the displacement and spacing between GEM foils, and so, we can use this same map to correct data runs that we have taken in different moments.

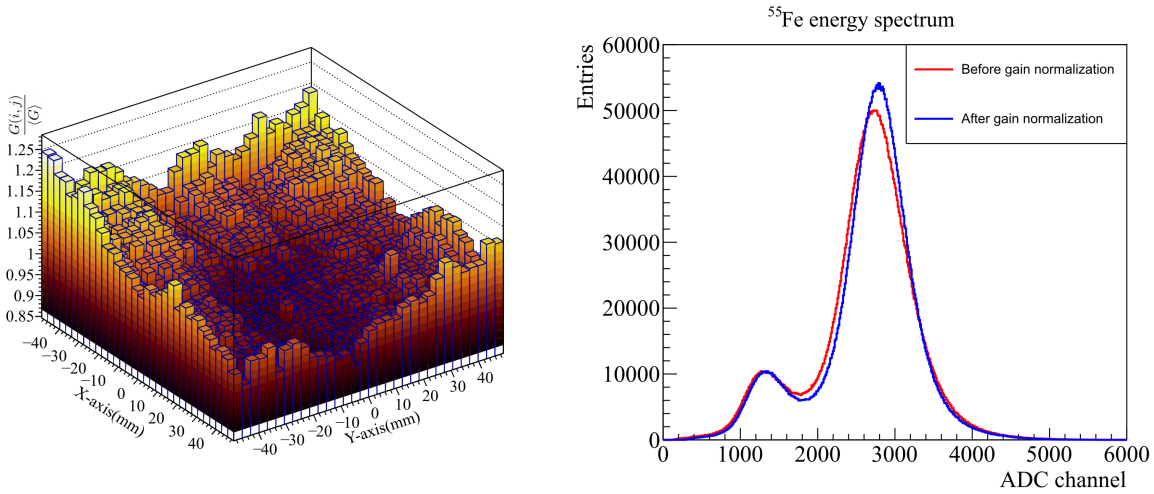


Figure 8.4: Left: Gain mapping of the detector. Variations of approximately ±20% can be observed, however, they can be corrected using a offline post processing analysis, improving the energy resolution in the full area of the detector. Right: ^{55}Fe energy spectrum before and after applying the gain correction along the active area.

A mechanism to reduce light intensity variations and enhance imaging quality when working with a strip readout is the flat field correction, presented first in chapter 5. Figure 8.5 shows the result of applying such correction to the data obtained using the APV25-SRS. The detector was irradiated using an ^{55}Fe source, placed 10 cm above the window. In this specific case, we have applied the intensity correction factor to the flat field image itself.

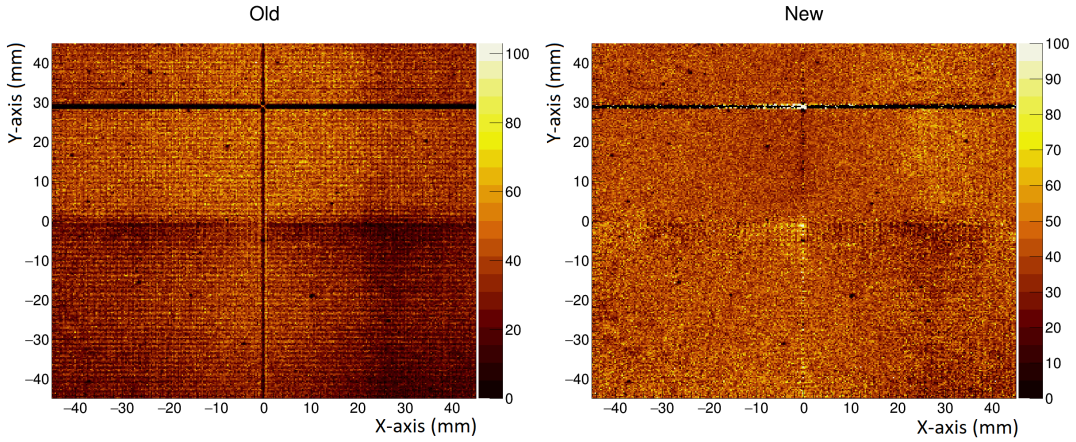


Figure 8.5: Flat field correction method applied to measurements using the APV25. Left: Reconstructed image. The dark lines at $x = y = 0$ mm are the junction between chips and at y≈ 30 mm is a dead channel. Right: Image of the same data set after applying the algorithm.

Since each quarter of the detector is read by a different APV25 hybrid that can have slight difference in their performance, larger counting differences specially between quadrants are expected, challenging the algorithm's performance in these regions. Figure 8.6 shows the projections along the X and Y axis of figure 8.5. It is possible to see that after the correction

the readout pattern is almost completely removed from the image.

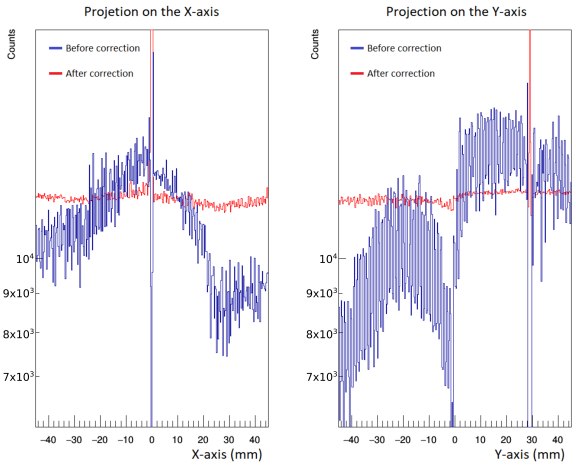


Figure 8.6: Profile of the image 8.5. The blue lines represent the total counts integrated over one axis before the correction. The red line shows the total integrated counts after applying the correction.

8.1.2 The SRS and the SAMPA chip

The SAMPA and the SRS integration has been successfully made and details regarding the acquisition software were already described in chapter 7. The system however is at an early stage when compared to the version that can be operated with the APV25. With the SAMPA, only a single hybrid board containing 4 chips, corresponding to 128 electronic channels (32 channels per chip) can be read at a time. For this reason, we have developed a one dimension (1D) strip readout that can be used for X-ray imaging transmission imaging and fluorescence. It consists of 256 strips (200 µm wide with a pitch of 400 µm), distributed uniformly across the 10 × 10 cm^2 sensitive area of the GEM stack. With one hybrid we are capable of reading half of the active region. Figure 8.7 shows on the left side the readout board developed at HEPIC@IFUSP, with two 140 pin Hirose-HRS connectors and, on the right side, the detector with the triple-GEM stack described in figure 7.1.

To characterize the detector in terms of both position and energy resolution the same measurements that were conducted with the APV25 were made with the SAMPA. Using the lead mask on top of the detector window, the contrast of a set of slits were measured with the 1D readout and the SAMPA-SRS acquisition system. Since all the charge collected along the Y-axis is integrated on the same strip at the X-axis, the pattern was protected with extra lead shielding to avoid the convolution of strips with different spatial frequency. Figure 8.8 shows the measurement of the contrast for two different runs. The peaks close to missing strips or spurious signals were not considered to this calculation and they are generated by the electrons

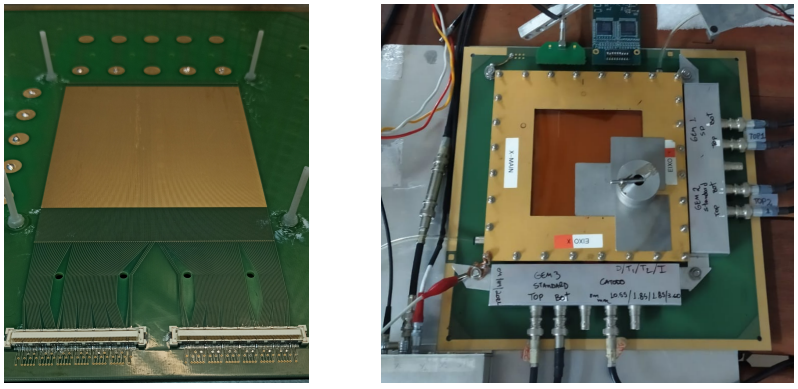


Figure 8.7: Left: the 1D readout used to test the SAMPA acquisition. This readout was designed to accommodate two SAMPA hybrids (256 strips). Right: The experimental setup with an ^{55}Fe radioactive source used to produce signals in the detector. One SAMPA hybrid is visible connected to the detector at the top center of the photography.

being pulled towards the closest working channel. The values I_{max} and I_{min} used to calculate the contrast are the mean over all available peaks for that specific spatial frequency.

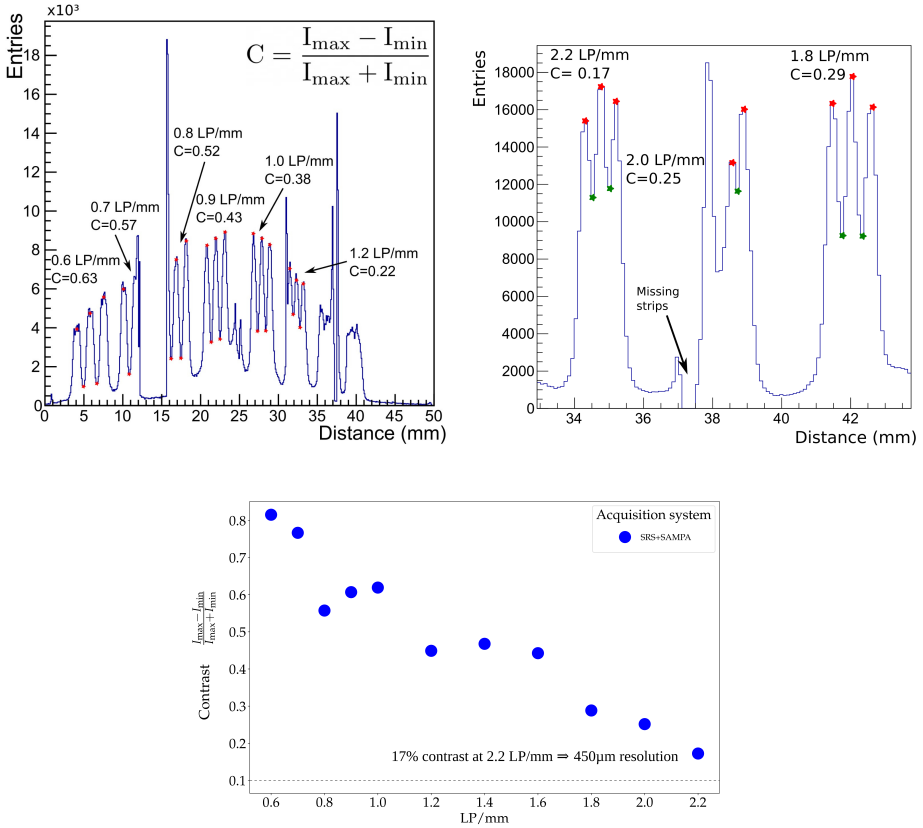


Figure 8.8: Top: Profile of the resolution pattern slits made using the SRS with SAMPA. The red and green dots represent the peaks and valleys that were used to calculate the contrast. Bottom: Contrast result using the SRS with the SAMPA chip.

The bottom part of figure 8.8 shows the contrast results calculated for the SAMPA chip.

The SAMPA chip is showing position resolution (better than 450 µm, 17% of contrast at 2.2 LP/mm). The acquisition with the SAMPA chip has the advantage of being much faster when compared to the APV25. The counting rate measured was above 6 kHz with room to be increased, while the maximum acquisition rate with the APV working with zero suppression was 1.2 kHz.

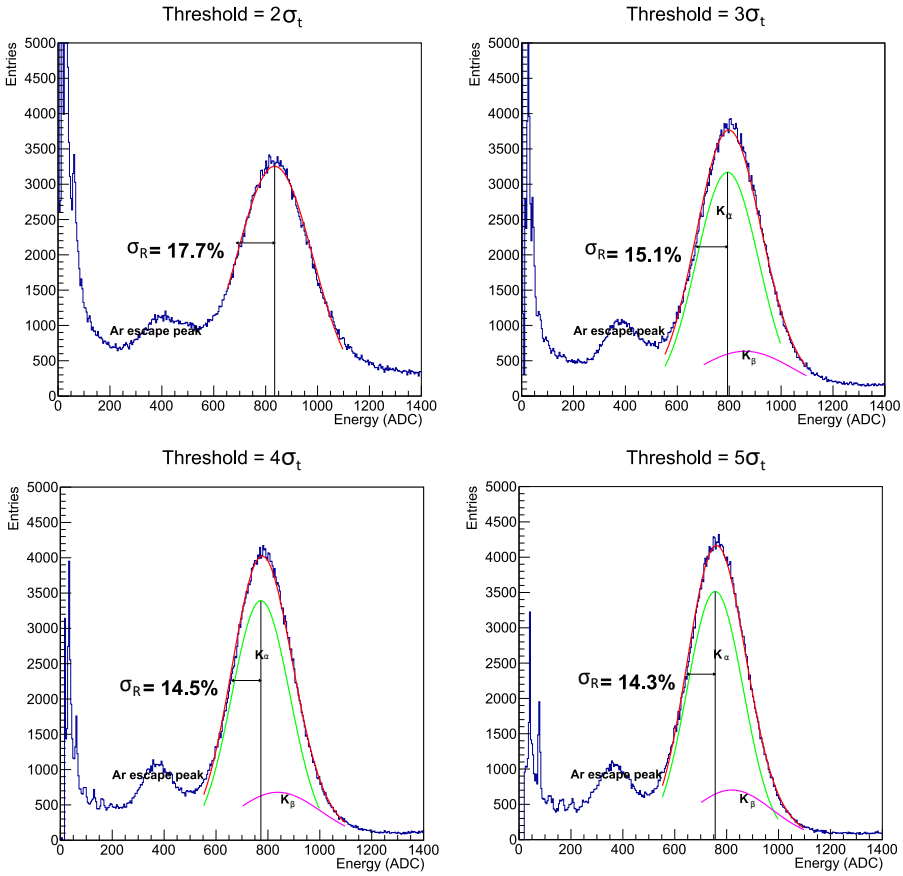


Figure 8.9: Different noise level acceptance in the clustering algorithm to reconstruct the energy spectrum of an ^{55}Fe source. A double Gaussian fit was made, showing different energy resolution for the K_α emission line. For $\sigma_t = 2$, the double Gaussian fit did not converge, so a single Gaussian distribution was fitted.

Figure 8.9 shows the energy spectrum reconstructed for different thresholds (σ_t). Since the detector has sensibility in only one dimension, a lead shielding with a 0.5 cm diameter hole was placed on the top of the window to reduce the spread of radiation across the active area of the detector that can spoil the final energy resolution due to gain non-uniformity. The difference in the spectra is mainly the amount of noise that is integrated into the event. This can be noticed by looking at the peak below channel 200 and the continuum of counts above channel 1200. The main peak distribution becomes thinner and the main and escape peak is also better distinguishable by increasing the threshold, indicating an improvement of the energy resolution (σ_R in these images). The best value achieved was 14.3%. Although it was shown in chapter 7

that the common-mode correction can be used to reduce the noise, it was not yet implemented in the processing chain.

The detector itself can achieve a much better energy resolution than it was observed using the APV25 and SAMPA chips. Figure 8.10 shows the energy spectrum for the ^{55}Fe X-ray source reconstructed using the signal from the bottom of the last GEM, passing by a pre-amplifier, a shaping amplifier and multichannel analyzer (Amptek's MCA8000D). Different factors make the resolution achieved in this case much better. The first one is the amount of charge which is deposited in this electrode. Looking at the values of extraction efficiencies for the standard geometry calculated in a previous work [16], one can see that the amount of charge that stays on the bottom of the last GEM is of the same order of magnitude of the one that goes to the readout plane. The charge deposited at the readout however, is divided in many strips while the one collected from the bottom goes to the same CSA. Also, the bottom electrode is decoupled from the readout electronics which can have additional noise. This image shows that an energy resolution close to the limit simulated in chapter 5 can be achieved, however, when using both the SRS and the MCA (decouple in terms of synchronized data acquisition) for position and energy calculation respectively, the information regarding the place where the interaction with such energy happened inside the detector is lost unless it is recorded by an ADC with a common block and trigger with the SAMPA, or with one SAMPA channel is modified to read specifically the bottom electrode.

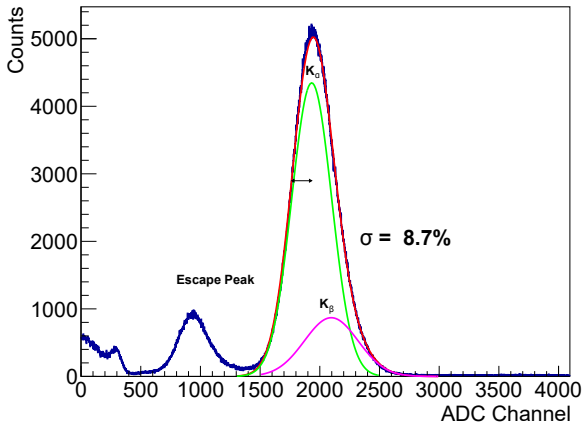


Figure 8.10: ^{55}Fe energy spectrum reconstructed using the signal from the bottom of the last GEM of the stack.

Image 8.11 shows the same titanium and copper plate from fig. 8.2 irradiated and using the SAMPA chip to reconstruct the fluorescence spectrum. The fluorescence emission lines are marked with black lines. Two separated Gaussian distributions were fitted to the data and the parameters can be seen at the top right corner.

It was observed that the SRS with SAMPA is already operating smoothly with a fair spatial

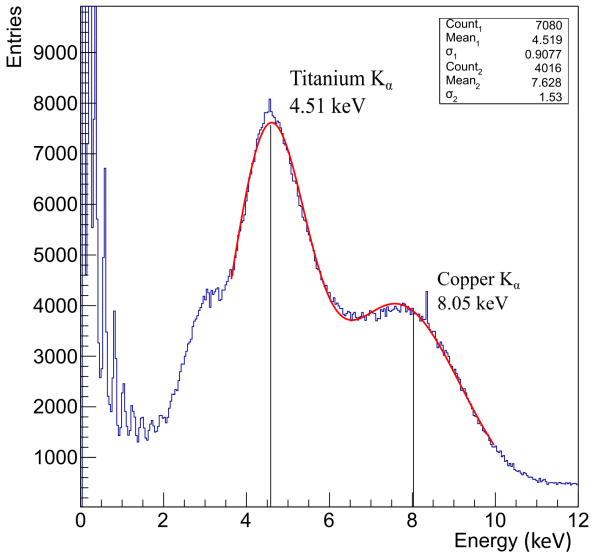


Figure 8.11: Energy spectrum obtained from the irradiation of a titanium and copper plate.

and energy resolution, 450 µm and $\sigma_R = 14.2\%$ for 5.9 keV respectively. The system is capable of working at higher or equivalent counting rates when compared to the other ASICs that are already being operated with the SRS such as the APV25 or the VMM. The SAMPA chip was designed to be implemented in the TPC of the ALICE experiment and for that the chip was optimized to handle a large event rate and also to store and transmit data during a long period of time (or even in a continuous mode), a requirement to be integrated on a TPC.

8.2 Application of the SAMPA in a TPC

The test of the SAMPA chip in X-ray detection has been done with promising results. However, we also wanted to test the full capability of the device by applying it to an experiment with the SRS in TPC mode, the type of experiment SAMPA was first designed for. To do so we are in a collaboration with the Van de Graaff group at the Institute of Experimental and Applied Physics of the Czech Technical University in Prague. Their main objective is to build a spectrometer to measure anomalies in the angular correlation of electrons and positrons that are produced in excited states of ^{8}Be and ^{4}He, which can be related with the signature of a hypothetical new boson [87, 88].

The experiment is based on building several detectors around a ^{7}Li target that is bombard with protons with the resonant energies of 441 keV or 1.03 MeV to produce ^{8}Be in an excited state. The closest detector to the target has to be made with a light and thin material, with high granularity (position resolution) and has to be operated in vacuum. Therefore, the Timepix3 [89] was the choice for this task. With these detectors around the target it will be

possible to reconstruct with a very good precision the point where the decay first happened. Passing this first detector there is a need to have an equipment with a light material that is going to slowly stop the particles, with a good energy resolution, that can cover a large solid angle and is capable of identifying charged particles passing through a magnetic field. The gaseous detectors and TPC are the ones that are going to fit in this task. Figure 8.12 shows a schematic of the experiment and pictures of the TPC field cages and the readout planes separately.

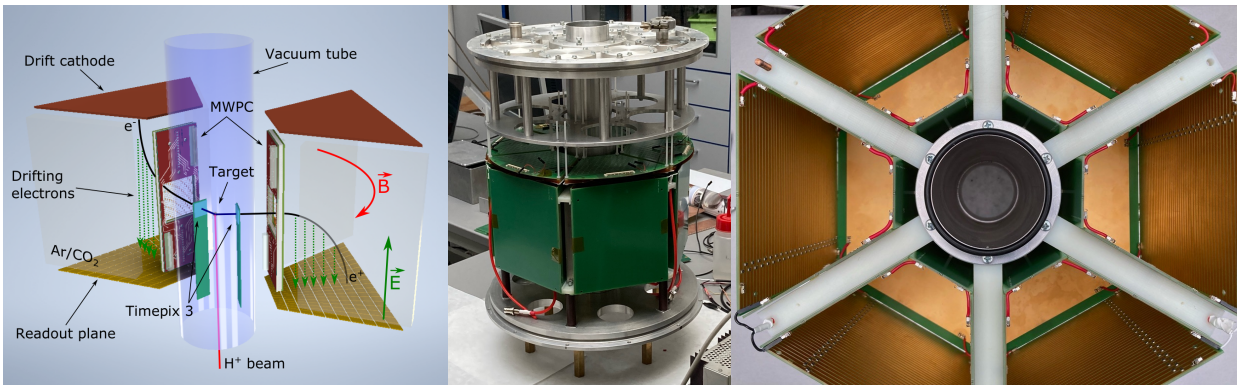


Figure 8.12: Spectrometer for the measurement of angular correlation between positrons and electrons [90]. Figures are courtesy of Hugo. N. da Luz - UTEF 2023.

The MWPCs presented inside the detector are going to be used as the trigger for the TPC. It is possible to see that the detector is composed of 6 separated segments, each of them equipped with a Timepix3, a MWPC, and a TPC with a GEM stack and a readout. Each segment of the TPC is between two 0.3 T permanent magnets that create a toroidal magnetic field. Particles passing through this field undergo a Lorentz force that bends their trajectory towards or away from the readout plane, depending on their charge.

To test the SAMPA-SRS integration a TPC prototype was built. The detector chamber was 3D printed using a PLA filament and a PCB based field cage was attached to the sides of the PLA vessel. The 80 mm high drift region was filled with a Ar/CO_2 (70/30) mixture in open and continuous flow of 15 l/h (at atmospheric pressure). The high flux was necessary to compensate for the strong out-gassing and leaks of the 3D printed vessel. In the meantime, the issues related to the leaks through the pores of the 3D printed material were solved by spraying its surface with an acrylic filler. The readout electrode of the TPC is composed of 120 pads (10×12 matrix), covering an active area of 10×10 cm^2 as shown in figure 8.13.

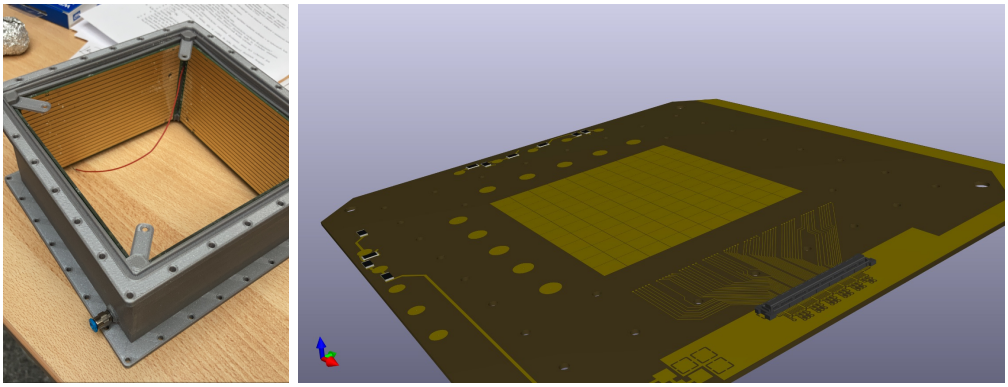


Figure 8.13: Left: Field cage used for electric field uniformity. Right: 3D model of the pad readout used for the tests with the TPC.

Figure 8.14 shows the full schematics of the detector on scale and also a picture of the setup during its operation. The detector was tilted by 30 degrees to provide longer, diagonal tracks (hitting a larger amount of pads). Two photo-multiplier tubes (PMTs) were used to create a coincidence trigger with the detector, one was placed above the detector and the other below it. The counting rate of cosmic rays, with the setup mounted like that, was approximately 1 Hz.

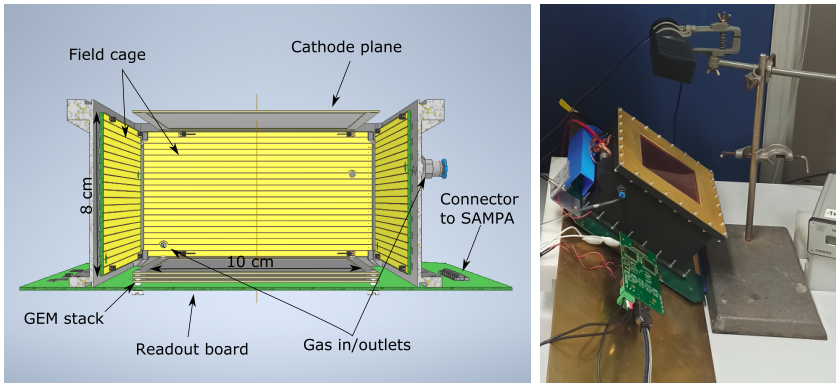


Figure 8.14: Left: Schematic of the prototype. Right: Telescope setup for cosmic ray measurements using two PMTs for trigger (the second one is at the bottom of the detector). The TPC is tilted to provide longer tracks.

Figure 8.15 shows the waveform for different SAMPA channels after the passage of a cosmic ray inside the detector. One can see in this picture the difference in time of arrival of the charge for each one of the pads.

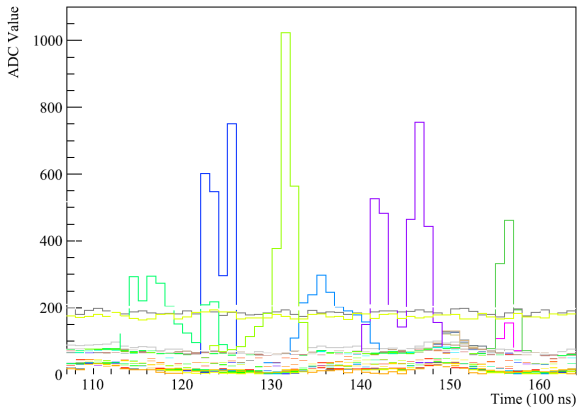


Figure 8.15: Signal produced in each pad (represented by the different colors) after the passage of a cosmic ray inside the detector. It is possible to see that the charge is deposited only in a few pads.

The clustering algorithms for TPCs are more complex than for X-rays due to the additional coordinate. For each coincidence trigger between the PMTs, a frame of samples with duration of typically 20 µs for all the channels was recorded. These raw signals were zero suppressed offline by removing the parts of pulses which were below a threshold of 5σ plus the baseline. To calculate the noise and baseline the first 80 samples of the frame were used, minimizing errors due to baseline shift since the acquisition can take a long time. To reconstruct the time coordinate a drift velocity of 1 cm/µs [91] was assumed.

The following images show examples of events that were detected and corrected through improvements implemented to the algorithm. Figure 8.16 shows the actual track, polluted by small amplitude noise signals that can still appear, since they can occasionally cross the threshold. The clustering algorithm removes these low amplitude events by applying a neighboring logic for adjacent pads and also in time, leaving only the track.

Figure 8.17 shows a spurious signal affecting almost all the channels at the same time. The origin of such an artifact can be a ground fluctuation or a baseline shift. This was removed by applying a higher threshold cut in the case of more than a specified number of channels with a signal in the same time bin. These small amplitude events were removed by this method, however, part of the track can also be lost.

In figure 8.18 we can see what happens to a track when the amount of charge generated by the passage of a muon is high enough to saturate the Charge Sensitive Amplifier (CSA) of SAMPA. If the algorithm detects that a channel is saturated (the maximum value of 1024 is read in sequence during a few time bins), the threshold is increased. In this case the zero suppression cut was changed to $20\sigma_t$ (σ_t being the standard deviation of the pedestal) as it can bee seen in figure 8.19. This method removes the tail in the Z-axis (charge tail in time), recovering the track with minor uncertainties.

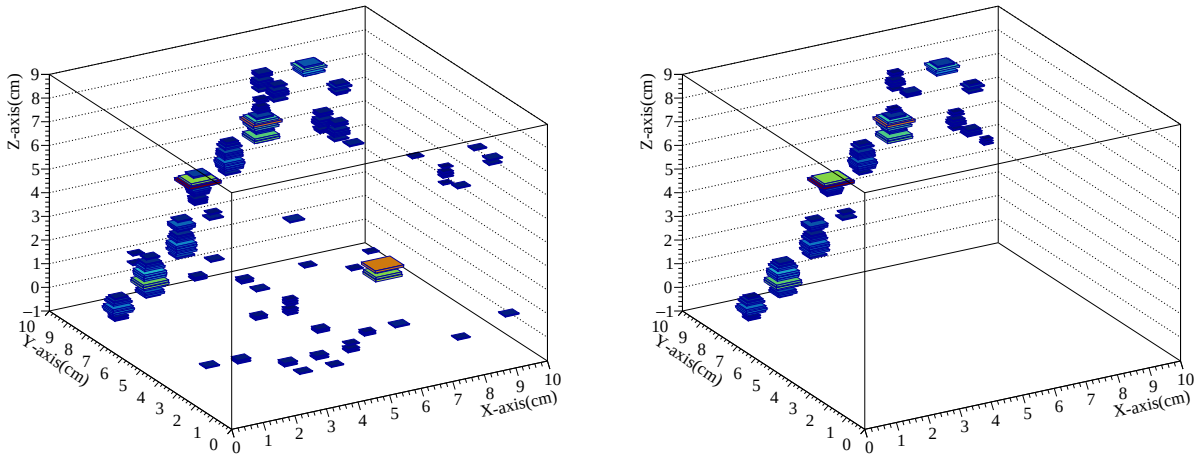


Figure 8.16: Left: Track and several small signals generated by noises. Right: Spaced signals are removed using the neighboring logic algorithm.

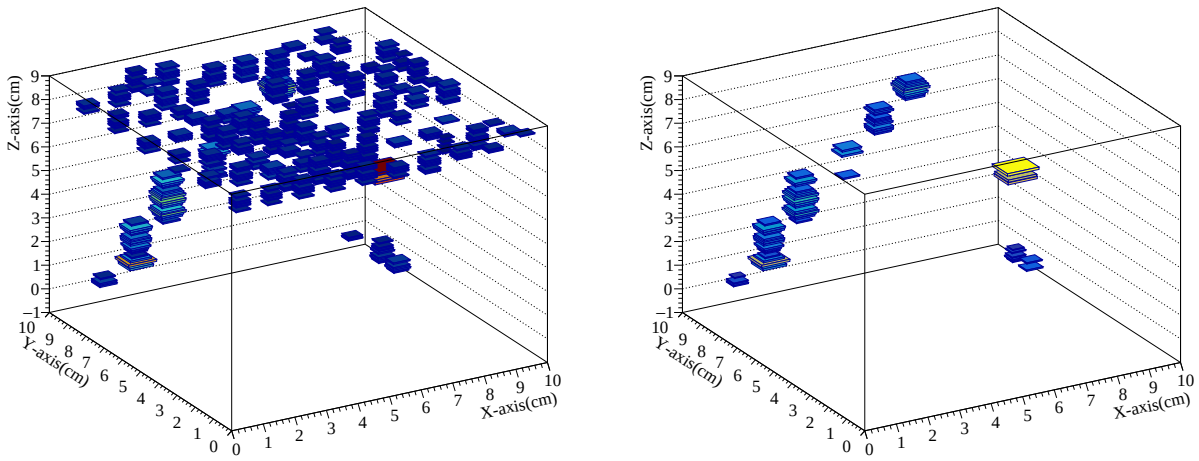


Figure 8.17: Left: Event reconstructed with a polluted time bin. Right: Clean track.

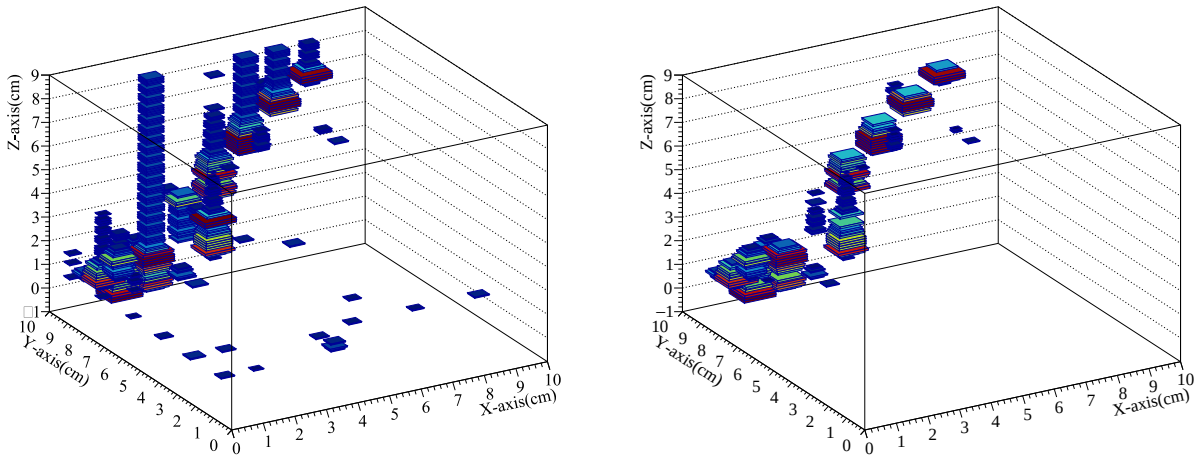


Figure 8.18: Left: Saturated pulses with a tail-like structure generating an elongated signal over the Z-axis (time coordinate). Right: The structure is removed by applying a different threshold when a saturated signal is found.

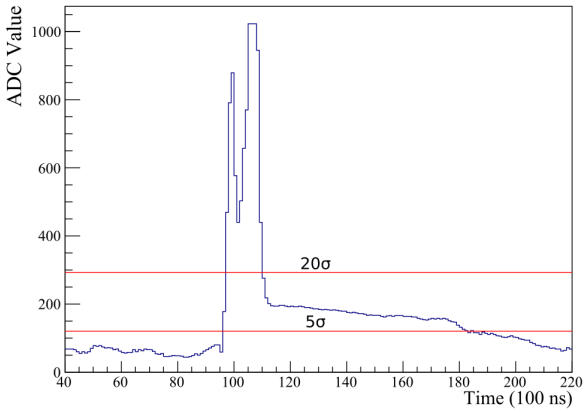


Figure 8.19: Two signals integrated by the SAMPA CSA in sequence. One can see that after the second pulse, which saturates the amplifier, the signal takes longer to return to the baseline.

The SAMPA chip has been tested in two different detectors and completely integrated in the CERN/RD51 Scalable Readout System. Both tests show promising results regarding high counting rate position and energy sensitive X-ray detection and also particle tracking. A complete software for control, acquisition and data process was developed, along with simple algorithms for event reconstruction and particle tracking with small effort. Although SAMPA shows its full capacity in TPC applications, it may also work very well in the near future for 2D X-ray imaging.

Chapter 9

Discussion and conclusions

The proposed goal of creating a large area sensitive detector for X-ray that can be used for X-ray fluorescence was achieved. We were capable of operating the detector with a rate of events that was never achieved before in our laboratory in this type of measurement. Despite the communication issues related with the adapter board and the FEC of the SRS, we have a thin-gap detector for X-ray fluorescence sensitive to energy and position that can be easily operated at counting rates above 20 kHz even without zero suppression of data. When the zero suppression is fully implemented, even higher rates will be achieved. The detector operated with the Scalable Readout System and the SAMPA chip reached a spatial resolution better than 450 µm when irradiated with a X-ray tube with maximum accelerating potential of 10 keV. The energy resolution obtained by the data reconstructed channel by channel with SAMPA was 14.2 % (σ, for 5.9 keV), or 838 eV. With this resolution, obtained by measuring the energy directly from the SAMPA chip's data, the distinction between elements which are 3 atomic numbers of distance will be possible (looking at the K_α fluorescence emission). However, using the signal from the bottom of the last GEM it is possible to achieve a much better energy resolution for the system, 8.7 % (σ, for 5.9 keV), or 513 eV, making it possible to resolve elements which are two atomic numbers of distance in some cases.

Several studies were conducted to better understand how the detector should be constructed and how to optimize it for the detection of X-ray fluorescence in the energy range of 1 keV to 30 keV. The simulations regarding detection efficiency and escape peak suppression have shown us that a thicker drift region can help to reduce the acquisition time by increasing the efficiency of the detector and at the same time will reduce the background (escape) peaks generated due to the gas fluorescence. This point, however, requires a compromise because a thicker drift region could lead to spark problems due to the larger voltages required to operate the detector and also electric fields non-uniformity. In the future one could try to use krypton as part of the gaseous mixtures to reduce even more any pollution in the energy spectrum if this proves to be a limiting factor of the detector.

A model to help us understand the undesired fluorescence inside the detector and to think in ways to reduce it was created. The most effective way to reduce such contamination is to remove the copper cladding of the GEM foils and use other metals such as chromium or aluminum. A more direct alternative to reduce the contamination peak relative intensity is

to increase the drift length of the detector, however secondary problems may appear such as field non-uniformity. The geometric response simulation of the detector may also provide data for a correction for the peak intensity and should be taken into account if one wants to measure sample composition. These measurements have not been conducted yet but we intend to continue this in the near future.

The studies showing the artifacts presented in images reconstructed using a segmented strip readout, have helped us to understand what can be changed to suppress them. This intrinsic issue can be suppressed but not completely eliminated, therefore the flat field correction method is an important tool to remove artifacts from images reconstructed by the system and may help to reduce mistakes when one is characterizing an object.

Regarding the ion backflow, placing a mesh between two of the GEM foils to create two separate regions of electric field that could favor the electron extraction in one of the GEMs while increasing the collection on the next one resulted in a field configuration that would actually decrease the transparency of the mesh to electrons. This ended in a final increase of the ion backflow.

Bibliography

[1] W. C. Röntgen, "Über eine neue art von strahlen," *In Aus den Sitzungsberichten der Würzburger Physik.-medic. Gesellschaft Würzburg - pages 137–147, 1895. Tradução para o Português: A. C. P. Carvalho, "Sobre uma nova espécie de raios", Rev. Imagem, 27(4):287-293*, 2005.

[2] T. Arai, N. Langhoff, A. Simionovici, V. Arkadiev, W. Knüpfer, T. Cechak, J. Leonhardt, J. Chavanne, A. Erko, A. Bjeoumikhov, A. Alexander, B. Beckhoff, I. Grigorieva, B. Kanngießer, B. Vidal, F. Scholze, A. Longoni, C. Fiorini, L. Strüder, and W. Malzer, *Handbook of Practical X-Ray Fluorescence Analysis*. Springer, 05 2006.

[3] D. Isabelle, "The PIXE analytical technique: Principle and applications," *Radiation Physics and Chemistry*, vol. 44, no. 1, pp. 25–30, 1994.

[4] W. R. Leo, *Techniques for nuclear and particle physics experiments: a how-to approach; 2nd ed.* Berlin: Springer, 1994.

[5] G. Charpak, R. Bouclier, T. Bressani, J. Favier, and Č. Zupančič, "The use of multiwire proportional counters to select and localize charged particles," *Nuclear Instruments and Methods*, vol. 62, no. 3, pp. 262 – 268, 1968.

[6] D. R. Nygren, "The Time Projection Chamber: A New 4 π Detector for Charged Particles," *eConf*, vol. C740805, p. 58, 1974.

[7] A. Oed, "Position-sensitive detector with microstrip anode for electron multiplication with gases," *Nucl. Instr. Meth. A*, vol. 263, no. 2, pp. 351 – 359, 1988.

[8] F. Sauli, "GEM: A new concept for electron amplification in gas detectors," *Nucl. Instr. Meth. A, vol. 386, p. 531-534*, 1997.

[9] Y. Giomataris, P. Rebourgeard, J. Robert, and G. Charpak, "MICROMEGAS: a high-granularity position-sensitive gaseous detector for high particle-flux environments," *Nucl. Instr. Meth. A*, vol. 376, no. 1, pp. 29 – 35, 1996.

[10] R. Chechik, A. Breskin, C. Shalem, and D. Mörmann, "Thick GEM-like hole multipliers: properties and possible applications," *Nucl. Instr. Meth. A*, 2004.

[11] J. F. C. A. Veloso, J. M. F. Santos, and C. A. N. Conde, "A proposed new microstructure for gas radiation detectors: The microhole and strip plate," *Rev. of Sci Inst. vol 71, no 6, p. 2371-2376*, 2000.

[12] F. D. Amaro, C. Santos, J. F. C. A. Veloso, A. Breskin, R. Chechik, and J. Santos, "The thick-COBRA: a new gaseous electron multiplier for radiation detectors," *Journal of Instrumentation, vol. 5, Out*, 2010.

[13] R. Bellazzini, M. Bozzo, A. Brez, G. Gariano, L. Latronico, N. Lumb, A. Papanestis, G. Spandre, M. Massai, R. Raffo, and M. Spezziga, "The WELL detector," *Nuclear Instruments and Methods in Physics Research Section A: Accelerators, Spectrometers, Detectors and Associated Equipment*, vol. 423, no. 1, pp. 125–134, 1999.

[14] G. F. Knoll, *Radiation detection and measurement; 4th ed.* New York, NY: Wiley, 2010.

[15] J. Alme et al., "The ALICE TPC, a large 3-dimensional tracking device with fast readout for ultra-high multiplicity events," *Nuclear Instruments and Methods in Physics Research Section A: Accelerators, Spectrometers, Detectors and Associated Equipment*, vol. 622, no. 1, pp. 316–367, 2010.

[16] G. G. A. de Souza, "X-Ray fluorescence imaging system based on Thick-GEM detectors," Master's thesis, University of São Paulo - Institute of Physics, Brazil, 2019.

[17] G. G. de Souza and H. N. da Luz, "XRF element localization with a triple GEM detector using resistive charge division," *Nuclear Instruments and Methods in Physics Research Section A: Accelerators, Spectrometers, Detectors and Associated Equipment*, vol. 937, pp. 141–147, 2019.

[18] J. Adolfsson, A. A. Pabon, M. Bregant, C. Britton, G. Brulin, D. Carvalho, V. Chambert, D. Chinellato, B. Espagnon, H. H. Herrera, T. Ljubicic, S. Mahmood, U. Mjörnmark, D. Moraes, M. Munhoz, G. Noël, A. Oskarsson, L. Osterman, A. Pilyar, K. Read, A. Ruette, P. Russo, B. Sanches, L. Severo, D. Silvermyr, C. Suire, G. Tambave, K. Tun-Lanoë, W. van Noije, A. Velure, S. Vereschagin, E. Wanlin, T. Weber, and S. Zaporozhets, "SAMPA chip: the new 32 channels ASIC for the ALICE TPC and MCH upgrades," *Journal of Instrumentation*, vol. 12, pp. C04008–C04008, apr 2017.

[19] S. Martoiu, H. Muller, A. Tarazona, and J. Toledo, "Development of the scalable readout system for micro-pattern gas detectors and other applications," *Journal of Instrumentation*, vol. 8, p. C03015, mar 2013.

[20] H. Schindler, "Garfield++ simulation of tracking detectors — user guide." `https://garfieldpp.web.cern.ch/garfieldpp/`, 2017.2. Access in: 14-09-2018.

[21] RD51 collaboration, "Development of micro-pattern gas detectors technologies." `https://rd51-public.web.cern.ch/`, 2021. Access in: 28-06-2021.

[22] M. J. Berger, J. H. Hubbell, S. M. Seltzer, J. Chang, J. S. Coursey, R. Sukumar, D. S. Zucker, and K. Olsen, "XCOM: Photon Cross Sections Database," *NIST Standard Reference Database 8 (XGAM)*, 2010. Access in: 13-10-2018.

[23] R. Evans, *The Atomic Nucleus*. McGraw Hill Book Company, Inc., New York, 1955.

[24] R. M. Eisberg and R. Resnick, *Quantum physics of atoms, molecules, solids, nuclei and particles; 2nd ed.* New York, NY: Wiley, 1985.

[25] K. S. Krane, *Introductory nuclear physics*. New York, NY: Wiley, 1988.

[26] L. Pozzo, "Positron Emission Tomography PET / SPECT Systems Study Viability Quantification," Master's thesis, University of São Paulo - Institute of Physics, Brazil, 2005.

[27] H. Bethe, "Zur theorie des durchgangs schneller korpuskularstrahlen durch materie," *Annalen der Physik*, vol. 397, no. 3, pp. 325–400, 1930.

[28] Amptek®, "Mini-X2 X-Ray Tube System for XRF." `https://www.amptek.com/products/mini-x2-x-ray-tube`, 2023. Access in: 20-04-2023.

[29] A. Cho, "Helium-3 shortage could put freeze on low-temperature research," *Science (New York, N.Y.)*, vol. 326, pp. 778–9, 11 2009.

[30] U.S. Departament of Energy - Office of Science, "Neutron and X-ray Detectors," *Report of the Basic Energy Sciences Workshop on Neutron and X-ray Detectors*, 2012.

[31] L. S. Filho, R. F. dos Santos, G. de Souza, M. Paulino, F. Souza, M. Moralles, H. da Luz, M. Bregant, M. Munhoz, C.-C. Lai, C. Höglund, P.-O. Svensson, L. Robinson, and R. Hall-Wilton, "Double-GEM based thermal neutron detector prototype," *Journal of Instrumentation*, vol. 17, p. P09018, sep 2022.

[32] ASTROLab du parc national du Mont-Mégantic, "Photographic plates." `https://astro-canada.ca/les_plaques_photographiques-photographic_plates-eng`, 2020. Access in: 05-06-2020.

[33] "The ALICE TPC, a large 3-dimensional tracking device with fast readout for ultra-high multiplicity events," *Nucl. Instr. Meth. A*, vol. 622, no. 1, pp. 316 – 367, 2010.

[34] D. Primor, *Local tracking in the ATLAS muon spectrometer*. PhD thesis, Tel Aviv U., 2007.

[35] F. Sauli and A. Sharma, "Micropattern gaseous detectors," *Annual Review of Nuclear and Particle Science*, vol. 49, no. 1, pp. 341–388, 1999.

[36] F. Sauli, *Gaseous Radiation Detectors: Fundamentals and Applications*. Cambridge Monographs on Particle Physics, Nuclear Physics and Cosmology, Cambridge University Press, 2014.

[37] Dimitrios, Sampsonidis, "Study of the performance of micromegas detectors in magnetic field," *EPJ Web Conf.*, vol. 174, p. 05003, 2018.

[38] I. Manthos, I. Maniatis, I. Maznas, M. Tsopoulou, P. Paschalias, T. Koutsosimos, S. Kompogiannis, C. Petridou, S. E. Tzamarias, K. Kordas, C. Lampoudis, I. Tsiafis, and D. Sampsonidis, "The micromegas project for the ATLAS new small wheel," *AIP Conference Proceedings*, vol. 2075, no. 1, p. 080010, 2019.

[39] F. Sauli, "The gas electron multiplier (GEM): Operating principles and applications," *Nucl. Instr. Meth. A*, vol. 805, pp. 2 – 24, 2016. Special Issue in memory of Glenn F. Knoll.

[40] "Upgrade of the ALICE Time Projection Chamber," Tech. Rep. CERN-LHCC-2013-020. ALICE-TDR-016, Oct 2013.

[41] A. Colaleo, A. Safonov, A. Sharma, and M. Tytgat, "CMS Technical Design Report for the Muon Endcap GEM Upgrade," Tech. Rep. CERN-LHCC-2015-012. CMS-TDR-013, Jun 2015.

[42] A. Cardini, G. Bencivenni, and P. De Simone, "The operational experience of the triple-GEM detectors of the LHCb muon system: Summary of 2 years of data taking," *IEEE NSS/MIC Proceedings, 759*, 2012.

[43] C. Altunbas, M. Capéans, K. Dehmelt, J. Ehlers, J. Friedrich, I. Konorov, A. Gandi, S. Kappler, B. Ketzer, R. D. Oliveira, S. Paul, A. Placci, L. Ropelewski, F. Sauli, F. Simon, and M. van Stenis, "Construction, test and commissioning of the triple-GEM tracking detector for COMPASS," *Nucl. Instr. Meth. A*, vol. 490, no. 1, pp. 177 – 203, 2002.

[44] D. Pfeiffer, F. Resnati, J. Birch, M. Etxegarai, R. Hall-Wilton, C. Höglund, L. Hultman, I. Llamas-Jansa, E. Oliveri, E. Oksanen, L. Robinson, L. Ropelewski, S. Schmidt, C. Streli, and P. Thuiner, "First measurements with new high-resolution gadolinium-GEM neutron detectors," *Journal of Instrumentation*, vol. 11, pp. P05011–P05011, may 2016.

[45] S. Uno, T. Uchida, M. Sekimoto, T. Murakami, K. Miyama, M. Shoji, E. Nakano, T.Koike, K. Morita, H. Satoh, T.Kamiyama, and Y. Kiyanagi, "Two-dimensional neutron detector with GEM and its applications," *Physics Procedia*, vol. 26, pp. 142 – 152, 2012. Proceedings of the first two meetings of the Union of Compact Accelerator-Driven Neutron Sources.

[46] Natal da Luz, H., Souza, F. A., Moralles, M., Carlin, N., Oliveira, R. A. N., Bregant, M., Suaide, A. A. P., Chubaci, J. F. D., Matsuoka, M., Silva, T. F., Moro, M. V., Rodrigues, C. L., and Munhoz, M. G., "Characterization of multilayer Thick-GEM geometries as 10B converters aiming thermal neutron detection," *EPJ Web Conf.*, vol. 174, p. 01012, 2018.

[47] M. Köhli, M. Klein, F. Allmendinger, A.-K. Perrevoort, T. Schröder, N. Martin, C. J. Schmidt, and U. Schmidt, "CASCADE - a multi-layer boron-10 neutron detection system," *Journal of Physics: Conference Series*, vol. 746, p. 012003, sep 2016.

[48] D. Mörmann, A. Breskin, R. Chechik, and B. Singh, "On the efficient operation of a CsI-coated GEM photon detector," *Nucl. Instr. Meth. A*, vol. 471, no. 3, pp. 333 – 339, 2001.

[49] S. N. Ahmed, "7 - position-sensitive detection and imaging," in *Physics and Engineering of Radiation Detection (Second Edition)* (S. N. Ahmed, ed.), pp. 435–475, Elsevier, second edition ed., 2015.

[50] W. R. Hendee and E. R. Ritenour, *Medical Imaging Physics, 4th ed.* New York, NY: Wiley, 2002.

[51] A. A. Michelson, "Studies in optics," *University of Chicago*, 1927.

[52] U. Neitzel, E. Buhr, G. Hilgers, and P. R. Granfors, "Determination of the modulation transfer function using the edge method: Influence of scattered radiation," *Medical Physics*, vol. 31, no. 12, pp. 3485–3491, 2004.

[53] R. Veenhof, "Garfield — simulation of gaseous detectors." `http://cern.ch/garfield`. Access in: 14-09-2018.

[54] S. F. Biagi, "Magboltz - transport of electrons in gas mixtures." `http://magboltz.web.cern.ch/magboltz/`, 1995. Access in: 21-07-2023.

[55] C. Geuzaine and J.-F. Remacle, "Gmsh: A 3-d finite element mesh generator with built-in pre- and post-processing facilities," *International Journal for Numerical Methods in Engineering*, vol. 79, no. 11, pp. 1309–1331, 2009.

[56] J. Ruokolainen, M. Malinen, P. Raback, T. Zwinger, A. Pursula, and M. Byckling, "Elmer-solver manual." `http://www.nic.funet.fi/index/elmer/doc/ElmerSolverManual.pdf`, 2018. Access in: 21-07-2023.

[57] I. Smirnov, "Modeling of ionization produced by fast charged particles in gases," *Nuclear Instruments and Methods in Physics Research Section A: Accelerators, Spectrometers, Detectors and Associated Equipment*, vol. 554, no. 1, pp. 474 – 493, 2005.

[58] B. Henke, E. Gullikson, and J. Davis, "X-ray interactions: photoabsorption, scattering, transmission, and reflection at E=50-30000 eV, Z=1-92," *Atomic Data and Nuclear Data Tables*, vol. 54, no. 2, pp. 181–342, 1993.

[59] Thompson, A. et al., *X-ray Data Booklet - LBNL/PUB-490 Rev.3.* Berkeley, CA, 94720: Lawrence Berkeley National Laboratory, 2009.

[60] I. Smirnov, "Modeling of ionization produced by fast charged particles in gases," *Nuclear Instruments and Methods in Physics Research Section A: Accelerators, Spectrometers, Detectors and Associated Equipment*, vol. 554, no. 1, pp. 474 – 493, 2005.

[61] M. Ribeirete, A. Policarpo, M. Salete, S. Leite, M. Alves, and E. D. Lima, "Fano factors of krypton-xenon mixtures," *Nuclear Instruments and Methods in Physics Research*, vol. 214, no. 2, pp. 561 – 563, 1983.

[62] M. Kase, T. Akioka, H. Mamyoda, J. Kikuchi, and T. Doke, "Fano factor in pure argon," *Nucl. Instr. Meth. A*, vol. 227, no. 2, pp. 311 – 317, 1984.

[63] C. Azevedo, S. Biagi, R. Veenhof, P. Correia, A. Silva, L. Carramate, and J. Veloso, "Position resolution limits in pure noble gaseous detectors for X-ray energies from 1 to 60 keV," *Physics Letters B*, vol. 741, pp. 272–275, 2015.

[64] P. Virtanen *et al.*, "SciPy 1.0: Fundamental Algorithms for Scientific Computing in Python," *Nature Methods*, vol. 17, pp. 261–272, 2020.

[65] J. Friedrich, U. Leloglu, and E. Tunali, "Radiometric camera calibration of the bilsat small satellite: Preliminary results," 02 2006.

[66] N. Hagen, "Flatfield correction errors due to spectral mismatching," *Optical Engineering*, vol. 53, p. 123107, 12 2014.

[67] F. M. Brunbauer, D. Munoz, D. Pfeiffer, E. Pollacco, E. Oliveri, F. I. G. Fuentes, F. J. I. Gutierrez, G. Norberg, L. Ropelewski, M. Lupberger, M. V. Stenis, P. Thuiner, and H. Muller, "Optical readout of gaseous detectors: new developments and perspectives." VCI2019 - The 15th Vienna Conference on Instrumentation, 2019.

[68] A. Morozov, L. M. S. Margato, M. M. F. R. Fraga, L. Pereira, and F. A. F. Fraga, "Secondary scintillation in CF4: emission spectra and photon yields for MSGC and GEM," *Journal of Instrumentation*, vol. 7, pp. P02008–P02008, feb 2012.

[69] J. Jaklevic, J. Kirby, M. Klein, A. Robertson, G. Brown, and P. Eisenberger, "Fluorescence detection of exafs: Sensitivity enhancement for dilute species and thin films," *Solid State Communications*, vol. 23, no. 9, pp. 679 – 682, 1977.

[70] L. Tröger, D. Arvanitis, K. Baberschke, H. Michaelis, U. Grimm, and E. Zschech, "Full correction of the self-absorption in soft-fluorescence extended x-ray-absorption fine structure," *Phys. Rev. B*, vol. 46, pp. 3283–3289, Aug 1992.

[71] H. Hirayama, "Lecture note on photon interactions and cross sections." KEK, High Energy Accelerator Research Organization, Tsukuba, Ibaraki, Japan, 2000.

[72] A. Kahoul, A. Abassi, B. Deghfel, and M. Nekkab, "K-shell fluorescence yields for elements with 6 $\leq$z$\leq$ 99," *Radiation Physics and Chemistry*, vol. 80, no. 3, pp. 369 – 377, 2011.

[73] B. Mindur, T. Fiutowski, S. Koperny, P. Wiącek, and W. Dąbrowski, "Performance of a GEM detector with copper-less foils," *Journal of Instrumentation*, vol. 12, pp. P09020–P09020, sep 2017.

[74] B. Mindur, T. Fiutowski, S. Koperny, P. Wiącek, and W. Dąbrowski, "Investigation of Copper-Less Gas Electron Multiplier Detectors Responses to Soft X-rays," *Sensors*, vol. 20, p. 2784, 05 2020.

[75] M. Chernyshova, K. Malinowski, T. Czarski, E. Kowalska-Strzęciwilk, P. Linczuk, A. Wojeński, R. D. Krawczyk, and Y. Melikhov, "Advantages of Al based GEM detector aimed at plasma soft-semi hard X-ray radiation imaging," *Fusion Engineering and Design*, vol. 146, pp. 1039 – 1042, 2019. SI:SOFT-30.

[76] K. Liang, Z. Zhang, J. Liu, M. Shao, and Y. Zhou, "TMM: A Triple Micro-Mesh gaseous structure with ultra-low ion backflow for gaseous photon detectors sensitive to visible light." Micro Pattern Gas Detectors 2022, 2022.

[77] A. Glaenzer, S. Aune, T. Benoit, F. Bossù, E. F. Ribas, and M. Vandenbroucke, "Reducing Ion Backflow with a novel MPGD structure using a bulked micro-mesh on a GEM," *Nuclear Instruments and Methods in Physics Research Section A: Accelerators, Spectrometers, Detectors and Associated Equipment*, vol. 1051, p. 168134, 2023.

[78] C. M. C. C. L. Roux and P. H. F. N. da Luz, "Ion backflow studies in micropattern gaseous detectors," *Simpósio Internacional de Iniciação Científica e Tecnológica da USP*, 2019. Acessed: 08/05/2023 - ISSN 2448-072X.

[79] "Bronkhorst®." `https://www.bronkhorst.com/`. Access in: 25-01-2019.

[80] "CAEN - Power Supply Module." `https://www.caen.it/products/v6521/`. Access in: 25-01-2019.

[81] "Raspberry Pi." `https://www.raspberrypi.org/`. Access in: 25-01-2019.

[82] A. L. M. Silva, M. L. Carvalho, K. Janssens, and J. F. C. A. Veloso, "A large area full-field EDXRF imaging system based on a THCOBRA gaseous detector," *J. Anal. At. Spectrom.*, vol. 30, pp. 343–352, 2015.

[83] M. J. French *et al.*, "Design and results from the APV25, a deep sub-micron CMOS front-end chip for the CMS tracker," *Nucl. Instr. Meth. A*, vol. A466, pp. 359–365, 2001.

[84] M. Lupberger, L. Bartels, F. Brunbauer, M. Guth, S. Martoiu, H. Müller, E. Oliveri, D. Pfeiffer, L. Ropelewski, A. Rusu, and P. Thuiner, "Implementation of the VMM ASIC in the scalable readout system," *Nuclear Instruments and Methods in Physics Research Section A: Accelerators, Spectrometers, Detectors and Associated Equipment*, vol. 903, pp. 91 – 98, 2018.

[85] H. Hernández, B. C. de Souza Sanches, D. Carvalho, M. Bregant, A. A. Pabon, R. W. da Silva, R. A. Hernandez, T. O. Weber, A. L. do Couto, A. Campos, H. A. Cubas, T. A. Martins, M. G. Munhoz, and W. Van Noije, "A monolithic 32-channel front end and dsp asic for gaseous detectors," *IEEE Transactions on Instrumentation and Measurement*, vol. 69, no. 6, pp. 2686–2697, 2020.

[86] R. Brun and F. Rademakers, "ROOT - an object oriented data analysis framework," *Proceedings AIHENP'96 Workshop, Lausanne, Sep. 1996, Nucl. Inst. Meth. A 389 81-86*, 1997.

[87] A. J. Krasznahorkay, M. Csatlós, L. Csige, Z. Gácsi, J. Gulyás, M. Hunyadi, I. Kuti, B. M. Nyakó, L. Stuhl, J. Timár, T. G. Tornyi, Z. Vajta, T. J. Ketel, and A. Krasznahorkay, "Observation of anomalous internal pair creation in ^{8}Be: A possible indication of a light, neutral boson," *Phys. Rev. Lett.*, vol. 116, p. 042501, Jan 2016.

[88] D. Alves, D. Barducci, and G. e. a. Cavoto, "Shedding light on X17: community report," *Eur. Phys. J. C*, vol. 83, no. 230, 2023.

[89] T. Poikela *et al.*, "Timepix3: a 65k channel hybrid pixel readout chip with simultaneous toa/tot and sparse readout," *Journal of Instrumentation*, vol. 9, p. C05013, may 2014.

[90] A. Cortez, H. N. da Luz, R. Sýkora, B. Ali, and L. Fajt, "A spectrometer for the measurement of anomalies in the angular correlation of electron and positron internally produced in excited ^{8}Be and ^{4}He," *Nuclear Instruments and Methods in Physics Research Section A: Accelerators, Spectrometers, Detectors and Associated Equipment*, vol. 1047, p. 167858, 2023.

[91] A. Peisert and F. Sauli, *Drift and diffusion of electrons in gases: a compilation (with an introduction to the use of computing programs)*. CERN Yellow Reports: Monographs, Geneva: CERN, 1984.